Aramco Journal of Technology

WINTER 2022

The *Aramco Journal of Technology* is published quarterly by the Saudi Arabian Oil Company, Dhahran, Saudi Arabia, to provide the company's scientific and engineering communities a forum for the exchange of ideas through the presentation of technical information aimed at advancing knowledge in the hydrocarbon industry.

Editor

William E. Bradshaw
william.bradshaw.1@aramco.com.sa
tel: +966-013-876-0498

Production Coordination

Richard E. Doughty
Corporate Publications, Aramco Americas

Design

Graphic Engine Design Studio
Austin, Texas, U.S.A.

The *Aramco Journal of Technology* gratefully acknowledges the assistance, contribution and cooperation of numerous operating organizations throughout the company.

ISSN 1319-2388

Contents

Principles and Advantages of High Power Lasers for Descaling Surface Equipment

Dr. Damian P. San-Roman-Alerigi, Dr. Saad M. Al-Mutairi, Dr. Sameeh I. Batarseh and Dr. Wisam J. Assiri

Abstract /

This work examines the physical principles and effects of high power laser (HPL) descaling of surface equipment. This contactless technique can fully remove sulfide or calcium carbonate ($CaCO_3$) scale without compromising the integrity of the substrate. The method is environmentally friendly, waterless, and energy efficient. It could do away with chemical and mechanical methods for descaling, which have shown low efficiency for treating fully plugged deposits and environmental risks, due to chemical use.

This article describes the process through an analysis of its efficiency and impact on the substrate material, the environment, and the implications to production reliability.

HPL descaling is described by a multiphysics approach that involves thermal and mechanical processes. The laser causes a phase-change on all or some of the constituents of the scale. This interaction results in spallation, dissociation, and high energy sublimation. Laser-matter interaction is precise. It produces a small heat affected zone (HAZ) that decays exponentially away from the illuminated area. Therefore, the effect of the laser on the surrounding material is minimal to none. Ultrasonic, multi-spectral imaging, microscopy, and statistical analysis are used to analyze the effect of the laser on the substrate material. The environmental impact of the HPL process is compared to existing methods; it is calculated via the carbon intensity of each step and supporting equipment involved in the processes, as well as by its impact to material reuse, waste reduction, and recycling.

Scaling can be detrimental to oil and gas production because it may hinder the flow of fluids to and from the well. In surface systems, scale deposits reduce the internal diameter of the equipment, thereby limiting the flow rate capacity and causing a pressure drop across the production network. From a physics perspective, the process is effective because the energy can be delivered with extreme precision on the target. The efficiency of the process depends on the coupling of the HPL with the target and the rate of debris evacuation.

The physics are complex, but can be optimized through machine learning, e.g., reinforcement learning. The results of the comprehensive characterization demonstrate that HPL descaling preserves the integrity of the substrate. HPL descaling could increase the lifetime of surface equipment affected by scale, and therefore contribute to reuse and recycling.

The adverse effects of scaling make prevention and removal crucial to the energy industry. Existing methods of scale removal rely on mechanical or chemical scrubbing, which show varying degrees of success and may deteriorate the substrate. HPL descaling is an environmentally friendly solution for production reliability; it enables complete descaling and the safe reuse or recycling of scaled equipment.

Introduction

A laser emits a coherent, unidirectional, and high energy beam of light that can be controlled and delivered to a target with high precision. These technical features make lasers ideal to drive processes where a localized phase-change is needed, e.g., welding, cutting, or piercing. The use of lasers in industrial processes has shown to improve efficiency, reduce waste, and decrease energy consumption, thereby eliminating or minimizing environmental impacts.

The same laser source can be customized to tackle multiple operations by modifying its temporal or spatial energy distribution. For example, in dentistry, a single laser is used to clean, drill, or cut by changing the optics and beam pattern. Lasers can also be configured to attain extreme precision; for instance, in medicine, laser scalpels are so precise they can cut cancerous cells without harming the healthy tissue. High power lasers (HPLs) and photonics could enable these same features in Upstream operations.

In Upstream operations, lasers already enable various tools, ranging from distributed fiber sensing to quantum computing. Yet, their application realm has been limited to the reach of low power lasers. HPLs are needed

to extend the usability envelop to all areas of the energy upstream cycle. Advances in laser technology and material engineering have progressively increased the output power and beam quality of lasers, maximizing efficiency and reducing the price per kilowatt to single digit figures.

HPL material processing uses a multi-kilowatt light beam to induce a thermal process on the target material, e.g., dissociation, melting, spallation, evaporation, or even sublimation. The energy required for these thermal processes results from the conversion of the absorbed laser radiation. Figure 1 illustrates the different factors affecting the energy coupling between the HPL and the target material[1].

The interaction is governed mainly by electromagnetic (EM) and thermomechanical properties of the target material, including fluid saturates present within its matrix. The former determines how the material scatters and absorbs EM radiation. The latter controls the thermal transport and phase change dynamics, including thermally induced chemical effects and the volume of the heat affected zone (HAZ). The interaction in terms of physics is intricate and fast-paced; yet, in the case of continuous wave and quasi-continuous wave HPLs, the system evolves to steady-state within the first hundred microseconds after illumination starts[2].

The HAZ in all cases is shallow (~10^{-6} m) because the beam is applied on a localized area and its power distribution is configured to decrease exponentially from the center. The penetration depth of the laser beam is in the order of micrometers, and material from the heated area is removed faster than the thermal diffusion or propagation time[3]. Finally, for all HPL applications it is crucial to characterize the properties of any fluid saturate in the target since these modify the overall EM and thermal properties of the material; conversely, the process can also affect their chemical properties.

Over the last two decades, experimental tests have demonstrated that an HPL with the appropriate optical

Fig. 1 *The outline of HPL rock interaction. The dynamics depend on the EM, thermal, and elastic properties of the material. These properties are a function of the local temperature and pressure; together with optical properties also relate to the EM field intensity, polarization, and frequency[1].*

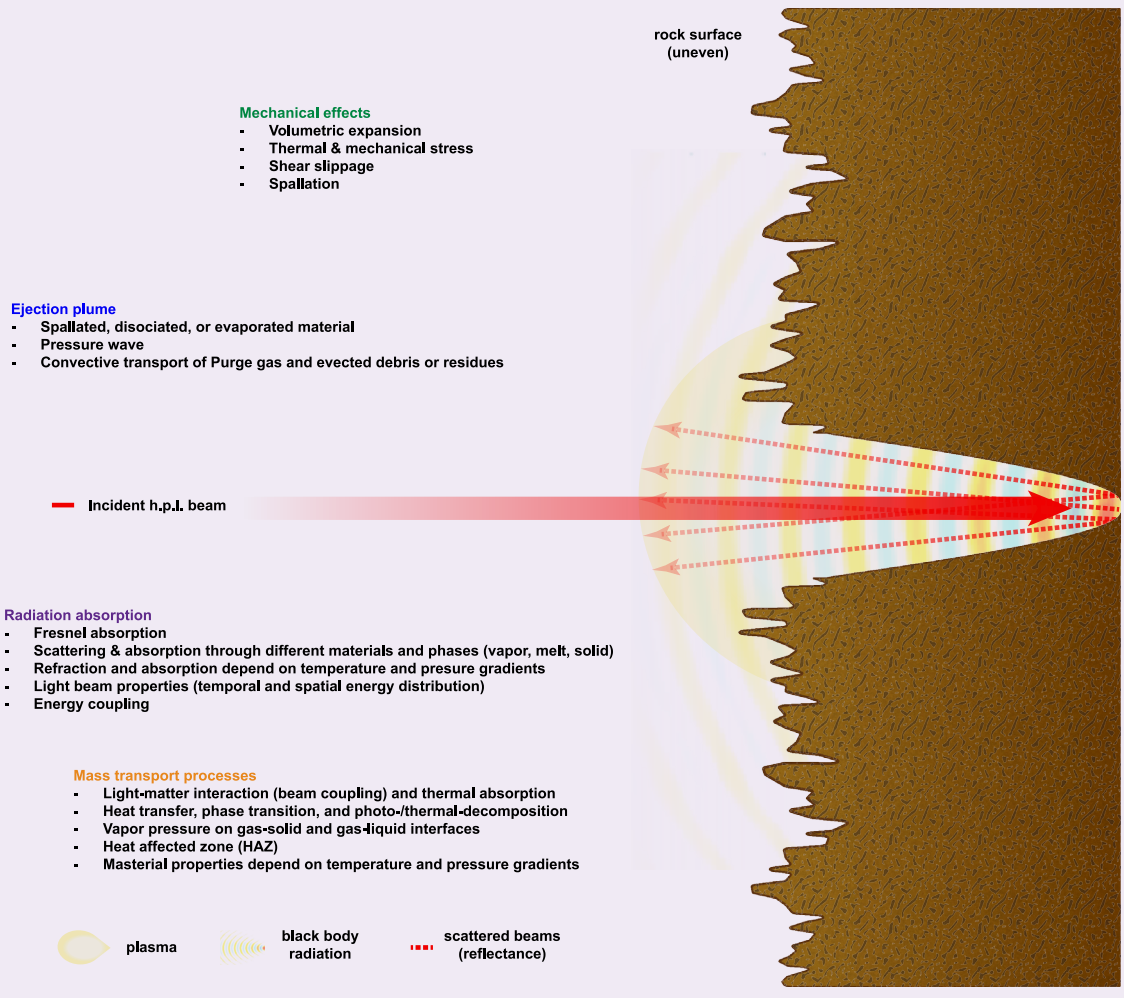

assembly can be used to descale, perforate, fracture, and drill. The research showed that a laser could be precisely controlled and oriented to deliver energy in any direction, regardless of the state of stress in the targeted rocks. This is crucial to production and reservoir management, where the ability to control the perforated tunnel's geometry and orientation could enhance production by eliminating compaction and improving permeability, thereby allowing the flow from pay zones currently bypassed by conventional technologies.

These features make the HPL attractive and a versatile tool to tackle different aspects of productivity enhancement and completion design. In the same manner as with perforations, the HPL beam can be controlled to remove scale deposited on tubings and flow lines without affecting the integrity of the metallic substrate. Therefore, the resulting pipe can be reused while eliminating waste, reducing costs, and saving time.

About Scale

Scale is an amorphous solid that results from the gradual deposition of precipitated minerals, which were previously dissolved in fluids, particularly water. The scale deposits often also include paraffins, asphaltenes, hydrocarbons, rock grains, and debris. The physicochemical interactions that cause scale formation can take at least one of several pathways: (1) Chemical reactions within the fluids or between them and their containers' surface (metal pipe, rock, or other materials); (2) disruptions in pressure or temperature, e.g., flow line elbows; (3) a change in the composition of a solution; or (4) a mixture of any of these processes[4].

Scales can be classified according to their chemical properties and acid solubility as: Sulfate-based (insoluble in acid), carbonate-based (soluble in acid), oxides (varying solubility), and mixtures (varying solubility). Table 1 summarizes the common types of scales and their chemical composition. Calcium carbonate ($CaCO_3$) is ubiquitous in the industry, while sulfate scales are infrequent, but challenging to treat.

Regardless of type, these deposits coat and constrict the internal diameter of flow conduits in the reservoir, wellbore, and surface, e.g., fractures, perforations, flow lines, trunk lines, casing, completions, tanks, and valves. The net effect is a decrease in flow rate capacity, which causes pressure drops across the production network and could even bring production to a halt[5, 6]. For example, in the 1990s at the Miller Field in the North Sea, production fell from 30,000 barrels per day to zero within 24 hours due to scaling plugs[7]. While a similar event has not been documented, it epitomizes the adverse effects of scaling and it highlights the need to develop technologies for scale prevention and fast removal.

Existing methods of scale removal rely on mechanical or acid scrubbing, which, depending on the frequency of use, may deteriorate the substrate and cause leaks[5]. These methods have been applied with varying degrees of success. Chemical pumping tends to be more effective than mechanical cleaning. Yet, the former requires a high volume of treatment chemicals, which present challenges to health and safety, while being unpractical to treat fully plugged deposits[8]. The HPL presents a unique opportunity to resolve these challenges and enable full refurbishments of scaled equipment, in particular flow lines. The journey of taking the first HPL descaling tool from the lab to field is recounted in the companion article[9].

HPL Descaling

The development of optimal removal techniques requires an understanding of the elemental composition and deposition process of scales. In particular, during HPL descaling, the layering and composition of the target can affect the coupling efficiency (laser matter interaction) and the removal dynamics (purging and debris extraction).

The HPL process can be described in terms of an energy balance; i.e.:

$$E_{in} = E_{loss} + E_{EM\ absorbed} + E_{EM\ reflected} \quad (1)$$

where the input energy, E_{in}, includes the contribution of the HPL beam (thermal energy) and purging fluids (thermal and mechanical energy). The right-side of Eqn. 1 encompasses the portion of EM energy reflected and absorbed by the material, as well as the thermal energy dissipated to the environment. The absorption efficiency is governed by the coupling dynamics between the HPL and the target. This energy in turn drives thermal transport and chemical phenomena that changes the host material, e.g., melting, evaporation, sublimation, dissociation, spallation, photolysis, thermolysis, etc., and facilitates its removal. The last step may require purging, and thereby the hydromechanical input to the energy balance.

Equation 1 provides a first approximation of the

Table 1 *Common types of scales classified by chemical basis[4].*

Classification	Name	Chemical Formula
Carbonates	Calcium carbonate	$CaCO_3$
	Ferrous carbonate	$FeCO_3$
Sulfates	Gypsum	$CaSO_4 \cdot 2H_2O$
	Hemihydrate	$CaSO_4 \cdot H_2O$
	Anhydrite	$CaSO_4$
	Barium sulfate	$BaSO_4$
	Strontium sulfate	$SrSO_4$
	Ferrous sulfide	FeS
Oxides	Ferrous hydroxide	$Fe(OH)_2$
	Ferrous hydroxide	$Fe(OH)_3$

temperature change induced by the laser. Given that the thermal conductivity of rock and scales is low (0.4 to 7 W m^{-1} K^{-1}) and that laser processes tend to impact a volume of the target for short periods of time, typically in seconds, then the bulk of the energy lost is due to blackbody radiation and scattering. Therefore, it is possible to rewrite the energy balance as:

$$E_{EM\,in} = A\epsilon\sigma_B\left(T_{target}^4 - T_{amb}^4\right) + E_{reflected/scatterd}, \quad 2$$

where ϵ is the emissivity, σ_B is the Boltzmann constant, A is the area of the beam, and T the temperature; therefore:

$$T_{target} = \left(\frac{\alpha E_{laser}}{A\epsilon\sigma_B} + T_{amb}^4\right)^{1/4}. \quad 3$$

The term α denotes the EM absorption coefficient of the target. Assuming that with a laser on target for 10 seconds of exposure on a circle with a diameter of 5 cm at 10^3 J s^{-1}, the temperature range expected in carbonate-based materials is between 1,000 °C to 3,500 °C. This temperature range is enough to excite thermolysis or calcination in calcium-based materials via the reaction in Eqn. 4[10].

$$CaCO_3 + Heat \rightarrow CaO + CO_2 \quad 4$$

Purging and removal of the material is crucial because the calcium oxide (CaO) could react spontaneously with water in the environment to create portlandite $Ca(OH)_2$ via the chemical reaction in Eqn. 5, or combined with CO_2 in the environment to generate $CaCO_3$ via carbonation.

$$CaO + H_2O \rightarrow Ca(OH)_2 \quad 5$$

Similar chemical reactions can be described for other carbonate-based and sulfate-based scales. In all cases, the chemical balance evinces that purging and removal of the material is crucial to avoid secondary reactions that could limit the efficiency of the process.

Figures 2[11] and 3[11] display the outcome of the first set of tests of HPL descaling in the lab. The white areas on the laser descaled sample in Fig. 2b could be a mixture of CaO and $Ca(OH)_2$.

The lab experiments showed two competing processes aiding scale removal. The first was the above-mentioned calcination. The second was fracturing of the bulk material and separation of small chunks (10^{-2} m) of scale that could be evected mechanically. This latter process is due to the build of thermal stress gradients typical of HPL processes[12], which led to a detachment across the many layers making the bulk of the scale deposits due to the ultrafast nature of the heating dynamics.

The interaction between these processes and the coupling dynamics means the laser removal rate is a function of several variables: laser energy density, scale type, layering, overall thickness, length, environmental constraints, and saturation fluids. The experimental investigation at the lab and the field showed HPL was capable of fully removing the scale; yet, the removal rate spanned from 1×10^{-2} cm s^{-1} up to 0.75 cm s^{-1}.

Fig. 2 *The cross-section of a scaled flow line (a) before, and (b) after the HPL descaling test[11].*

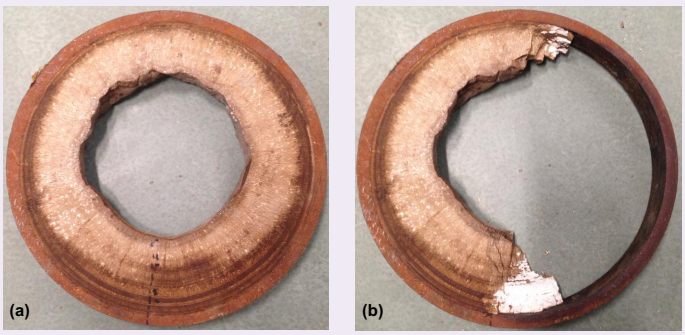

Fig. 3 *The cross-section of a scaled valve (a) before, and (b) after the HPL descaling test[11].*

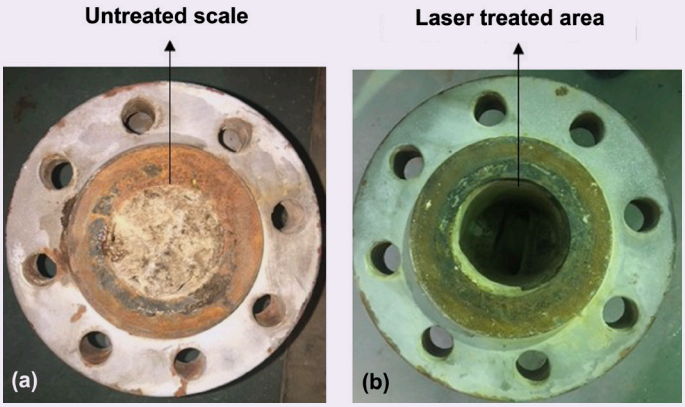

Of significant note, the experiments indicated that higher removal rates occurred in samples with left-over hydrocarbons. A potential explanation is that hydrocarbon fluids may have higher absorption in the near infrared than the scale, which could lead to more pronounced thermal gradients and faster energy transfer to the solid target.

Effect on the Metallic Substrate

The experiments in either the lab or field focused on scale samples deposited on metal pipes. The ideal removal method should be capable of removing the scale without affecting the substrate. This part of the study characterized metal samples before and after HPL descaling through photomicrographs and unconstrained velocity measurements.

Photomicrographs

Photomicrographs provide a visual analysis of the substrate's structure. Figures 4a and 4c shows the corresponding micrographs for the pipe before, and Figs. 4b and 4d shows the corresponding micrographs for the pipe after, at two different resolutions. Qualitatively,

Fig. 4 *Photomicrographs of the transversal section of the steel pipe chosen at a random location. The photos show the structure of the steel at 50 um (top) and 100 um (bottom) resolution before (a and c) and after (b and d) the laser descaling process.*

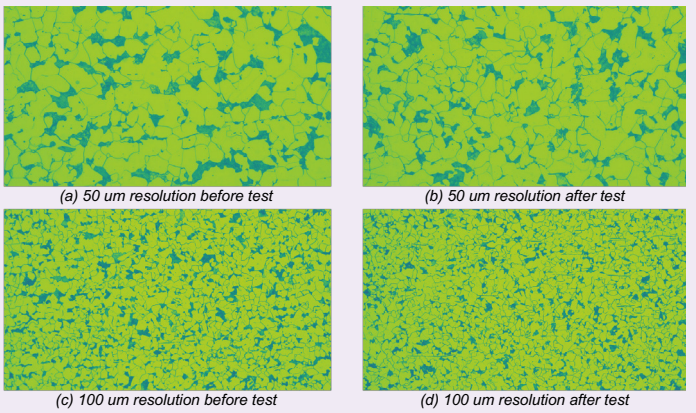

the microstructure before and after seems unaffected by the HPL descaling process.

Figure 5 further adds to this notion by observing that the distribution of luminosity across the samples is similar — had there been major changes, then the micrographs would show areas of damage that would darken the images.

Mechanical Properties

Nondestructive analysis using acoustic testing was used to characterize the uncompressed mechanical properties of the metal. The measurements used a section of the pipe descaled during one of the field trials and was compared to the standard values of carbon steel. The results are summarized in Table 2.

Table 2 *The mechanical properties of a pipe section before and after HPL descaling.*

Property	Standard	After (+/- 5%)
E (GPa)	200	199.3
Poisson ratio	0.3	0.3
P wave (m/s)	5,950 5,800 – 6,100	6,102.3
S wave (m/s)	3,200 3,100 – 3,300	3,093

The results indicate that within the margin of error the mechanical properties of the metal substrate remain unchanged after HPL descaling.

Fig. 5 *A histogram of luminosity with median (Q2) for the 100 um resolution photomicrographs before (bottom) and after (top) HPL descaling.*

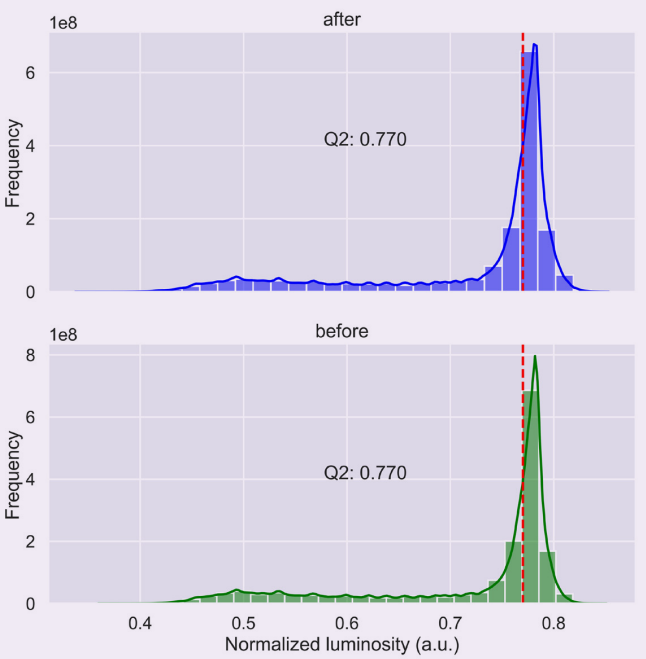

Conclusions

Scaling can be detrimental to oil and gas production because it may hinder the flow of fluids from and to the well. In surface systems, scale deposits reduce the internal diameter of equipment, thereby limiting the flow rate capacity and causing pressure drops across the production network. HPL descaling is a novel method to remediate and refurbish metallic conduits affected by scale. The experimental results in carbonate scale demonstrate that the technology is effective because the energy can be delivered with extreme precision on the target. The efficiency of the process depends on the coupling of the HPL with the target and the rate of debris evacuation.

HPL descaling is described by a multiphysics approach that involves thermal and mechanical processes. The laser causes a phase change on all or some of the constituents of the scale. This interaction results in spallation, dissociation, and high energy sublimation. Laser matter interaction is precise. It produces a small HAZ that decays exponentially away from the illuminated area. Therefore, the effect of the laser on the surrounding material is minimal to none.

Future work will examine the chemical changes in the scale in detail and provide a quantitative view of the effect on the metallic substrate.

HPL descaling is an environmentally friendly solution for production reliability; it enables complete descaling and the safe reuse or recycling of scaled equipment.

Acknowledgments

This article was prepared for presentation at the SPE Annual Technical Conference and Exhibition, Houston, Texas, October 3-5, 2022.

References

1. San-Roman-Alerigi, D.P., Batarseh, S.I., Li, W. and Othman, H.: "Machine Learning and the Analysis of High Power Electromagnetic Interaction with Subsurface Matter," SPE paper 195118, presented at the SPE Middle East Oil and Gas Show and Conference, Manama, Kingdom of Bahrain, March 18-21, 2019.
2. San-Roman-Alerigi, D.P., Batarseh, S.I. and Han, Y.: "Numerical Modeling of Thermal and Mechanical Effects in Laser-Rock Interaction — An Overview," paper presented at the 50th U.S. Rock Mechanics/Geomechanics Symposium, Houston, Texas, June 26-29, 2016.
3. Batarseh, S.I.: "Application of Laser Technology in the Oil and Gas Industry: An Analysis of High Power Laser-Rock Interaction and Its Effect on Altering Rock Properties and Behavior," Ph.D. thesis, Colorado School of Mines, 2001.
4. BinMerdhah, A.B., Yassin, A.A.M. and Muherei, M.A.: "Laboratory and Prediction of Barium Sulfate Scaling at High Barium Formation Water," *Journal of Petroleum Science and Engineering*, Vol. 70, Issues 1-2, January 2010, pp. 79-88.
5. Esbai, R.E. and Palanisamy, G.: "Eliminating Scale Buildup Challenges and Lessons Learnt from the Fadhili Reservoir Awali Field," SPE paper 184204, presented at the SPE Middle East Artificial Lift Conference and Exhibition, Manama, Kingdom of Bahrain, November 30-December 1, 2016.
6. Malik, A., Tiwari, A., Fartiyal, P., Lele, S., et al.: "Holistic Management of Calcium Carbonate Scaling in a Mature Field: A Case Study," SPE paper 188121, presented at the SPE Kingdom of Saudi Arabia Annual Technical Symposium and Exhibition, Dammam, Kingdom of Saudi Arabia, April 24-27, 2017.
7. Crabtree, M., Eslinger, D., Fletcher, P., Miller, M., et al.: "Fighting Scale — Removal and Prevention," *Oilfield Review*, Autumn 1999, pp. 30-45.
8. Hassig, S., Serrano, D., Villacres, C., Flor, D., et al.: "Methodology to Remediate and Evaluate Surface Flow Line Capacity with Coiled Tubing Cleanouts," SPE paper 206215, presented at the SPE Annual Technical Conference and Exhibition, Dubai, UAE, September 21-23, 2021.
9. Batarseh, S.I., Al-Mutairi, S.M., San-Roman-Alerigi, D.P., Assiri, W.J., et al.: "First Industrial Flow Lines Descaling Field Deployment Utilizing High Power Laser Technology," paper prepared for presentation at the SPE Annual Technical Conference and Exhibition, Houston, Texas, October 3-5, 2022.
10. Karunadasa, K.S.P., Manoratne, C.H., Pitawala, H.M.T.G.A. and Rajapakse, R.M.G.: "Thermal Decomposition of Calcium Carbonate (Calcite Polymorph) as Examined by in Situ High Temperature X-ray Powder Diffraction," *Journal of Physics and Chemistry of Solids*, Vol. 134, November 2019, pp. 21-28.
11. Batarseh, S.I., Mutairi, S., San Roman Alerigi, D.P. and Al Harith, A.: "Laser Technology for Downhole Applications; Past, Present and Future," SPE paper 204661, prepared for presentation at the SPE Middle East Oil and Gas Show and Conference, Manama, Kingdom of Bahrain, November 28-December 1, 2021, event canceled.
12. Han, Y., Fang, Y., San-Roman-Alerigi, D.P. and Batarseh, S.I.: "Thermal/Mechanical Interaction in Laser Perforation Process: Numerical Model Buildup and Parametric Study," *SPE Journal*, Vol. 24, Issue 5, October 2019, pp. 2097-2110.

About the Authors

Dr. Damian P. San-Roman-Alerigi

Ph.D. in Electrical Engineering, King Abdullah University of Science and Technology

Dr. Damian P. San-Roman-Alerigi is a Petroleum Scientist working with the Production Technology Team of Saudi Aramco's Exploration and Petroleum Engineering Center – Advanced Research Center (EXPEC ARC). His focus is on developing the next generation of subsurface photonic and electromagnetic tools.

Damian's previous research focused on the interaction of waves with complex media and its application to subsurface technologies. His work encompasses different areas of science and engineering, from oil and gas to applied mathematics. He has published papers in various international journals and conferences around the world.

Damian received his B.S. degree in Physics from the National Autonomous University of Mexico, Mexico City, Mexico. In 2008, he enrolled in King Abdullah University of Science and Technology (KAUST) as a founding class student where he completed his M.S. degree in 2010, and his Ph.D. degree in 2014, both in Electrical Engineering.

Dr. Saad M. Al-Mutairi

Ph.D. in Petroleum Engineering, King Fahd University of Petroleum and Minerals

Dr. Saad M. Al-Mutairi is a Chief Technologist in the Production Technology Division of Saudi Aramco's Exploration and Petroleum Engineering Center – Advanced Research Center (EXPEC ARC). He has more than 20 years of experience in reservoir and production engineering. Saad has also served the company in many technical and leadership positions within upstream organizations, including petroleum engineering and development, Southern Area oil operation and exploration. He was part of the advanced training program exchange with Chevron USA in 2007.

Saad has published more than 30 journal and conference papers and filed six patents. In 2018, he received the Southern Area Oil Operations Vice President Excellence Award. Saad graduated from the company's Technical Development Program in 2014 with a specialty area of CO_2 enhanced oil recovery.

He is a very active Society of Petroleum Engineers (SPE) member, assisting in SPE events and serving in various positions. Saad has also received two regional SPE awards, including Sustainability and Stewardship in the Oil and Gas Industry and Middle East Service in 2022 and 2016, respectively.

Saad is considered the first Saudi to graduate with a Ph.D. degree in the history of the Petroleum Engineering & Geosciences College at King Fahd University of Petroleum and Minerals (KFUPM), Dhahran, Saudi Arabia.

He received his B.S., M.S. and Ph.D. degrees in Petroleum Engineering from KFUPM.

Dr. Sameeh I. Batarseh

Ph.D. in Petroleum Engineering, Colorado School of Mines

Dr. Sameeh I. Batarseh is a Petroleum Engineering Consultant working with the Production Technology Team of Saudi Aramco's Exploration and Petroleum Engineering Center – Advanced Research Center (EXPEC ARC). Currently, he is the Focus Area Champion of the Unconventional Resources leading the High-Power Laser Program. Sameeh's area of interest is to develop an in situ laser application in drilling, perforation and fracturing, among many other applications with a focus on unconventional reservoirs.

He is an active member of the Society of Petroleum Engineers (SPE), serving the society since 1992 while holding different positions, including sitting on the SPE Executive Advisory Committee, ATCE Program Committees (Chairperson), subcommittees (chair and member). Sameeh was also on the board and Vice Chair for the Western Region USA San Joaquin Valley chapter. His service is recognized worldwide as he received the SPE President Section Award of Excellence, Regional Service Award, and is a SPE Distinguished Lecturer, Distinguished Member and Editorial Review Committee Technical Editor. He has organized over 54 SPE technical workshops.

Sameeh has authored or coauthored more than 92 articles with high-impact publications, and has an H-Index of 36. He holds 85 patents (41 granted patents and 44 patents in progress).

Sameeh received his Ph.D. degree in Petroleum Engineering from the Colorado School of Mines, Golden, CO.

Dr. Wisam J. Assiri

Ph.D. in Petroleum Engineering, Colorado School of Mines

Dr. Wisam J. Assiri is a Petroleum Engineer working with Production Technology Team of Saudi Aramco's Exploration and Petroleum Engineering Center – Advanced Research Center (EXPEC ARC). Currently, he is working with the Unconventional Resources Focus Area leading the field deployment of the high-power laser technology.

Wisam was involved in different research projects related to formation damage in the areas of condensate banking and emulsified acids characterization.

In 2006, he received his B.S. degree in Chemical Engineering from King Fahd University of Petroleum and Minerals (KFUPM), Dhahran, Saudi Arabia. In 2012, Wisam received his M.S. degree in Petroleum Engineering from the Colorado School of Mines, Golden, CO. In 2017 he received his Ph.D. degree in Petroleum Engineering, also from the Colorado School of Mines.

Responsive and Controlled Release of Surfactant Encapsulated in Amino-Functionalized Mesoporous Silica Nanoparticles

Hala A. AlSadeg, Ahmed W. Alsmaeil, Mohammed F. Alhassni and Dr. Amr I. Abdel-Fattah

Abstract /

Mesoporous silica nanoparticles (MSNs) have the potential to be carriers for the controlled release of surfactants for enhanced oil recovery (EOR) applications. Herein, MSNs containing a cationic surfactant, CTAB, where the surface functionalized with amino groups and their surfactant release behavior was studied and compared with that of nonfunctionalized MSNs. The responsive release of surfactant molecules from the mesoporous particles was studied under high salinity conditions normally encountered in subsurface environments.

Fourier-Transform infrared spectroscopy (FTIR) analysis was carried out to characterize the functionalized particles spectroscopically. Zeta potential measurements were made to study the alteration in the surface charge of the capsules. Thermalgravimetric analysis (TGA) was conducted to investigate the amount of encapsulated CTAB in the silica capsules. Dynamic light scattering and scanning electron microscopy (SEM) analyses were performed to confirm the morphology and size of these surfactant incorporated particles in saline water containing 56,000 mg/L salts.

FTIR and zeta potential data confirmed the presence of amino groups on the MSN surfaces, and the results from the TGA demonstrated that the CTAB concentration is directly affected by the functionalization and amino groups bound to the MSNs. Dynamic light scattering and SEM analyses showed that the amino-functionalized MSNs are 100 nm in size and maintain their chemical stability when present in high salinity water.

Interfacial tension (IFT) measurements showed that the IFT is reduced when the amino-functionalized MSNs are suspended in high salinity water compared to when suspended in deionized (DI) water. The oil-brine IFT was reduced up to 3×10^{-4} mN/m when the amino-functionalized MSNs were suspended in high salinity water. The functionalized MSNs' higher IFT values when suspended in DI water indicate that the surfactant release only happens in ion rich environments, which is representative of subsurface conditions. The release data indicates that the presence of the amine functional groups in MSNs results in a regulated release mechanism where the functionalized particles in high salinity water released 30% of the CTAB in one day.

The release data indicated that the presence of the amino-functionalized groups in MSNs improved the release properties of the encapsulated CTAB. Therefore, the slow release of surfactant from these amino-functionalized nanocapsules around the wellbore will result in a farther reach and deeper penetration in the reservoir.

Introduction

Enhanced oil recovery (EOR) is an active field of research that strives to maximize the recovery factor of hydrocarbon reservoirs. There are multiple chemical EOR strategies available; one is to increase the volumetric sweep efficiency by reducing the water-oil mobility ratio through injecting polymers, and another is to reduce the residual oil saturation by lowering water-oil interfacial tension (IFT) through the injection of surfactants and nanoparticles. Surfactant injection is considered an effective approach as it reduces the IFT and alters the wettability of rock surfaces[1]. Subsequently, as is the case with many technologies, these are accompanied with several challenges. These challenges include instability at harsh conditions of high temperatures and high salinity reaching up 120 °C and 250,000 ppm. Another major challenge is the adsorption onto rock surfaces where the injected chemicals do not travel deep in the reservoir and are restricted to areas near the wellbore.

One approach to address these challenges is to deliver the surfactant to areas in the reservoir using nanocarriers[2]. The nanocarriers have the potential to deliver surfactant molecules to targeted locations in the reservoir while reducing surfactant adsorption onto the rock. One type of these nanocarriers is the mesoporous silica nanoparticles (MSNs), where the pore size diameter ranges from 2 nm^3 to 50 nm^3. Since their discovery, mesoporous materials have attracted widespread interest in many applications, including drug delivery[4], water

treatment[5], and others[6]. One advantage of this system is that it is possible to functionalize the pores and the surface of the MSNs, which make them suitable to host different molecules and release them in situ in a controlled manner.

Recently, it was demonstrated that mesoporous nanoparticles offer a platform for controlled release of a cationic surfactant, CTAB, encapsulated in the pores of the nanocarrier[7, 8]. In that work, mesoporous silica, MCM-41, was used as the host to deliver the encapsulated cationic surfactant by ion exchange with the ions available in high salinity water.

Here, we go beyond that work to assess MSNs containing a cationic surfactant where a surface functionalized with amino groups in terms of their surfactant release behavior, and compared with that of nonfunctionalized MSNs under high salinity conditions, are normally encountered in subsurface environments.

Methodology

Materials and Synthesis

The brine solutions were prepared with varying amounts of salt, Table 1[9, 10].

The mesoporous silica materials were synthesized utilizing CTAB as described in literature[11, 12]. Tetraethyl orthosilicate was utilized as the silica source. Our procedure for the amino-functionalization of MSNs with primary amines uses (3-Aminopropyl)triethoxysilane (APTES), which is a silane with an amino group, a functionalization commonly used to create systems for different applications.

For this step, the MCM-41 MSNs were re-suspended in a toluene solution and APTES was introduced. The solution was refluxed for 6 hours for amino-functionalization. The resulting particles were washed and dried in a vacuum oven at 100 °C overnight.

Figure 1 shows the MCM-41 amino-functionalization setup.

Characterization

Scanning electron microscopy (SEM) images were obtained to analyze the size and morphology of the resulted particles. Fourier-Transform infrared spectroscopy (FTIR) measurements were performed to assess the functional groups present in the amino-functionalized MSNs. Zeta potential measurements were carried out to determine the surface charge of the particles. Thermalgravimetric analysis (TGA) was conducted under atmospheric conditions and a flow rate of 10 ml/min.

IFT between crude oil and brine is an important variable in water-oil and water-oil-gas displacements. For the IFT measurements we utilized the spinning drop tensiometer by Kruss as it performs really well for low IFT measurements with a high resolution. In our experiments we used 1 mL of heavy phase and 1 uL of light phase. The light phase used was crude oil and

Table 1 *Salt content used in the prepared brine solution.*

Compound	NaCl	$CaCl_2.2H_2O$	$MgCl_2.6H_2O$	Na_2SO_4	$NaHCO_3$
Mass (g L-1)	41.0	2.4	17.6	6.3	0.2

Fig. 1 *The MCM-41 amino-functionalization experimental setup.*

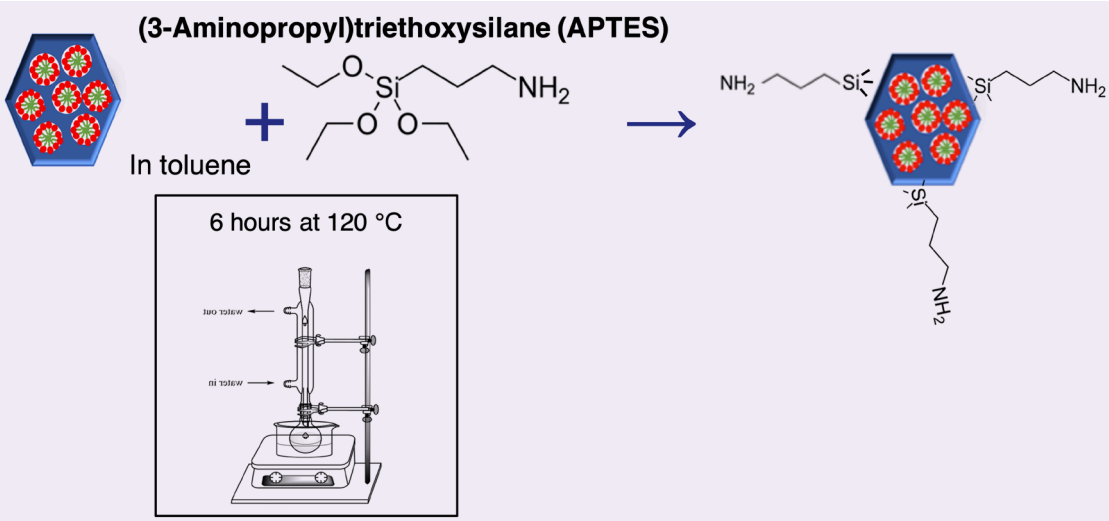

the heavy phase used was the nanoparticle suspension.

Surfactant Release Experiments

Release experiments were conducted by dissolving 1 mg of encapsulated surfactant per 1 ml of brine. The solution was continuously stirred to simulate the dynamic conditions of the reservoir, where fluids are in constant movement. This was done for a period of 5 days where a sample was collected each day to investigate the release behavior.

The collected sample was centrifuged at 6,000 rpm for 15 minutes and the powder was placed in the oven at 50 °C to dry. The dried powder was then analyzed utilizing TGA and IFT to determine the amount of surfactant remaining in the capsules.

Results and Discussion

Characterization

Figure 2 shows the SEM images. The images show spherical structures with a diameter of 103 ±10 nm. Moreover, it appears that the particles are porous where the surfactant molecules are encapsulated. The assembly of CTAB molecules appears as spherical-like micelles, which indicates that the ionic interaction of negatively charged silica species led to forming the mesostructured materials, in addition to the presence of the APTES on the surface that could have attributed to the complex surface.

Figure 3 shows the FTIR spectra of the MCM-41, indicating the peaks present from 2,850 cm^{-1} to 2,918 cm^{-1}. These are due to the stretching vibration of the C-H bonds, which are present in the CTAB surfactant. The peaks at 2,300 cm^{-1} to 2,400 cm^{-1} are due to the atmospheric carbon dioxide. The asymmetrical stretching vibration of the Si-O bond is seen from 1,000 cm^{-1} to 1,100 cm^{-1}, whereas the symmetrical stretching vibration of Si-O is at approximately 800 cm^{-1}. In addition to that, Zeta potential measurements were carried out and showed a positive surface charge, indicating amino surface functionalization.

Additionally, the TGA data in Fig. 4 indicates that the material encapsulates about 40 wt% CTAB in non-functionalized MCM-41, which is seen from the mass drop from 130 °C to 360 °C. The weight loss before that is due to the physically adsorbed water[8]. Moreover, it shows that the surfactant remained encapsulated in the nanoparticles even after functionalization as it shows 36% organic content in the amino-functionalized MCM-41 particles from the mass drop from 130 °C to 360 °C.

Surfactant Release

TGA measurements were performed to study the surfactant release behavior in the amino-functionalized MCM-41 in different aqueous solutions. Results shown in Fig. 5 demonstrate that the release of the surfactant in samples suspended in deionized (DI) water were almost identical to the non-suspended sample and negligible compared to the sample suspended in brine. This indicates that the CTAB release in the amino-functionalized MCM-41 sample is more responsive in the ionic medium.

Fig. 2 *The SEM images show that the individual particle size is about 100 nm.*

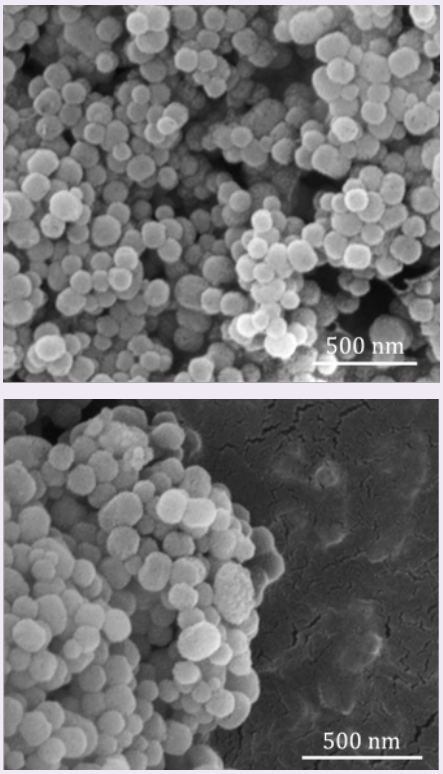

Fig. 3 *The FTIR of the MCM-41 indicating the presence of the organic material at the peaks present from 2,850 cm^{-1} to 2,918 cm^{-1}.*

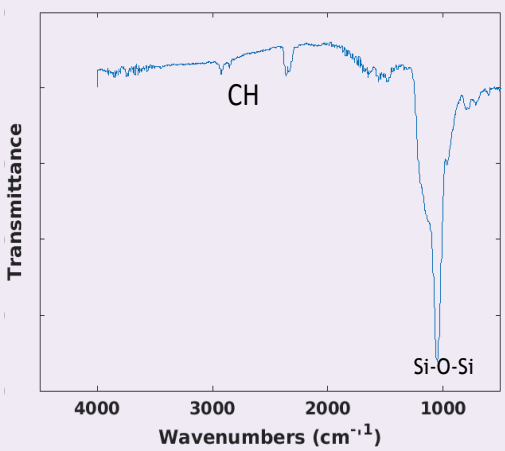

To investigate the release behavior further, surfactant release was measured for functionalized and nonfunctionalized samples after being suspended in high salinity water for a full day. Figure 6 shows a controlled release profile due to functionalization where acquired TGA shows 38% surfactant release after day 1 in the amino-functionalized MCM-41 sample.

Fig. 4 *The TGA indicates the presence of 36 wt% CTAB in amino-functionalized MCM-41 (orange) in contrast to 41 wt% CTAB in nonfunctionalized MCM-41 (blue).*

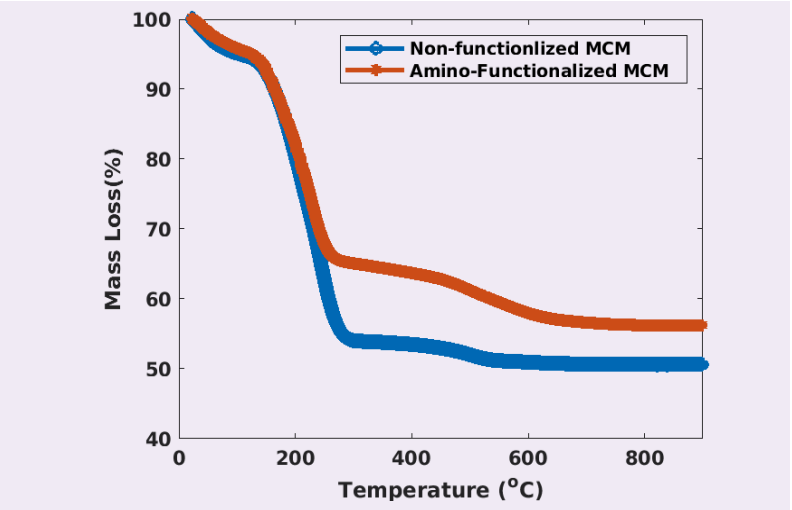

Fig. 5 *The TGA indicates that the release of CTAB in DI water (orange) is negligible compared to the release of CTAB in high salinity water (yellow).*

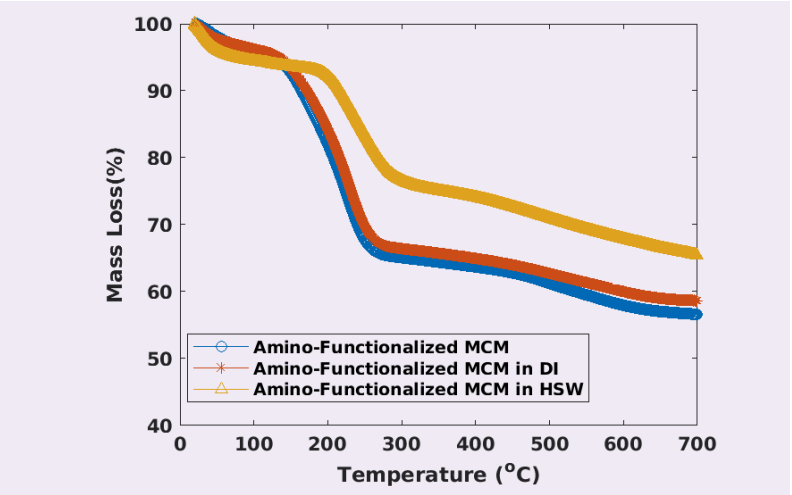

This is a higher release rate compared to the nonfunctionalized material, which showed a 20% surfactant release after 1 day.

IFT Experiments

Reduction of the IFT between oil and water is one of the main processes to enhance the recovery of oil[1]. It has been previously demonstrated that the release of CTAB only occurs when the particles are suspended in high salinity water and is negligible in DI water[8]. To study the behavior of the amino-functionalized capsules and to further demonstrate that the release of the CTAB from the nanocapsules are responsive to the ions present in high salinity water, we measured the IFT of 0.1 wt% of the suspension (MCM-41

Fig. 6 *The controlled release of CTAB in amino-functionalized MCM-41 is higher than the controlled release of CTAB in nonfunctionalized MCM-41.*

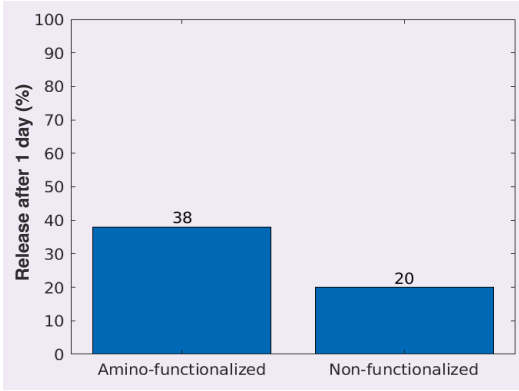

Fig. 7 *The IFT between crude oil and amino-functionalized and nonfunctionalized MCM-41 systems in water. Blue: suspended in DI water, and orange: suspended in high salinity water.*

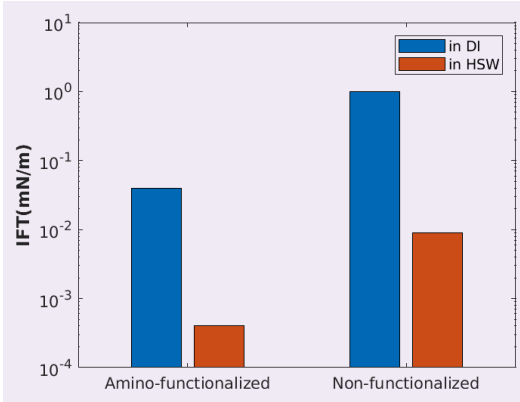

encapsulating CTAB in high salinity water) with crude oil in DI water and a brine aqueous medium. The IFT between high salinity water and crude oil ranges from 10 mN/m to 30 mN/m.

As shown in Fig. 7, in the case of amino-functionalized MCM-41, the IFT decreased to 3×10^{-4} mN/m in high salinity water compared to 3×10^{-2} mN/m for the case of the DI water. This indicates the preferential adsorption to the oil-water interface when the suspension is in high salinity water. The IFT is significantly higher when the particles are suspended in DI water, which confirms their responsiveness to the ions of the medium. In addition to that, the amino-functionalized MCM-41 had overall lower IFT values in both DI water and high salinity water solutions compared to the nonfunctionalized MCM-41.

To further investigate the mechanism of the IFT reduction, surfactant release experiments were conducted. The CTAB containing the amino-functionalized

MCM-41 solution was kept stirred to simulate the dynamic conditions of the reservoir, where fluids are in constant movement for a period of 5 days, and a sample was collected each day to investigate release behavior.

As shown in Fig. 8, there is a decreasing trend in IFT values, which indicates gradual surfactant release in the amino-functionalized sample. By day 4, the IFT values was reduced by two orders of magnitude in these samples. Therefore, this clearly indicates that there is a synergy that exists between the surfactant and the mesoporous material where both can achieve a lower IFT in comparison to the neat released surfactant or surfactant-free MCM-41.

Fig. 8 *The IFT trend between crude oil and amino-functionalized MCM-41 system in water over a period of 5 days.*

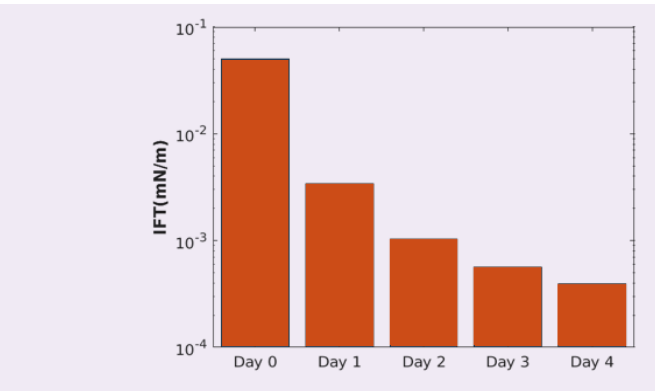

Summary and Conclusions

We demonstrated that MSNs present a promising platform for delivery of surfactant molecules for subsurface oil reservoirs. In this article we studied amino-functionalized MCM-41 release behavior in contrast to nonfunctionalized MCM-41 to assess the controlled delivery system of encapsulated CTAB surfactant for efficient wettability alteration and to achieve ultra-low IFT.

The main findings are as follows:

- The surfactant molecules are used as templates and are incorporated into the mesopores of the silica particles of approximately 100 nm in diameter.
- The release of CTAB from the silica particles is approximately 38% after 1 day.
- Both amino-functionalized and nonfunctionalized MSNs show that the release of the surfactant is preferential when suspended in high salinity water as indicated by the lower IFT values.
- The particles were able to reduce the IFT by two orders of magnitude higher with the amino-functionalized particles in comparison to the nonfunctionalized particles.
- The systems studied here are of potential use for surfactant delivery for EOR applications where minimizing surfactant adsorption is desired.

Acknowledgments

The authors would like to thank Mustafa AlSaffar for his support in conducting the IFT experiments.

This article was presented at the SPE Annual Technical Conference and Exhibition, Houston, Texas, October 3-5, 2022.

References

1. Kamal, M.S., Hussein, I.A. and Sultan, A.S.: "Review on Surfactant Flooding: Phase Behavior, Retention, IFT, and Field Applications," *Energy & Fuels*, Vol. 31, Issue 8, July 2017, pp. 7701-7720.
2. Cortés, F.B., Lozano, M., Santamaria, O., Marquez, S.B., et al.: "Development and Evaluation of Surfactant Nanocapsules for Chemical Enhanced Oil Recovery (EOR) Applications," *Molecules*, Vol. 23, Issue 7, June 2018.
3. AlOthman, Z.: "A Review: Fundamental Aspects of Silicate Mesoporous Materials," *Materials*, Vol. 5, Issue 12, December 2012, pp. 2874-2902.
4. Tukappa, A., Ultimo, A., de la Torre, C., Pardo, T., et al.: "Polyglutamic Acid-Gated Mesoporous Silica Nanoparticles for Enzyme-Controlled Drug Delivery," *Langmuir*, Vol. 32, Issue 33, August 2016, pp. 8507-8515.
5. Hammami, M.A., Croissant, J.G., Francis, L., Alsaiari, S.K., et al.: "Engineering Hydrophobic Organosilica Nanoparticle-Doped Nanofibers for Enhanced and Fouling Resistant Membrane Distillation," *ACS Applied Materials & Interfaces*, Vol. 9, Issue 2, December 2016, pp. 1737-1745.
6. Doadrio, A.L., Salinas, A.J., Sánchez-Montero, J.M. and Vallet-Regi, M.: "Drug Release from Ordered Mesoporous Silicas," *Current Pharmaceutical Design*, Vol. 21, Issue 42, 2015, pp. 6189-6213.
7. Betancur, S., Carrasco-Marín, F., Franco, C.A. and Cortés, F.B.: "Development of Composite Materials Based on the Interaction between Nanoparticles and Surfactants for Application in Chemical Enhanced Oil Recovery," *Industrial & Engineering Chemistry Research*, Vol. 57, Issue 37, August 2018, pp. 12367-12377.
8. Alsmaeil, A.W., Enotiadis, A., Hammami, M.A. and Giannelis, E.P.: "Slow Release of Surfactant Using Silica Nanosized Capsules," *SPE Journal*, Vol. 25, Issue 6, December 2020, pp. 3472-3480.
9. Abdel-Fattah, A.I., Mashat, A., Alaskar, M. and Gizzatov, A.: "NanoSurfactant for EOR in Carbonate Reservoirs," SPE paper 188046, presented at the SPE Kingdom of Saudi Arabia Annual Technical Symposium and Exhibition, Dammam, Kingdom of Saudi Arabia, April 24-27, 2017.
10. Gizzatov, A., Mashat, A., Kosynkin, D., Alhazza, N., et al.: "Nanofluid of Petroleum Sulfonate Nanocapsules for Enhanced Oil Recovery in High Temperature and High Salinity Reservoirs," *Energy & Fuels*, Vol. 33, Issue 11, 2019, pp. 11567-11573.
11. Wu, S-H., Mou, C-Y. and Lin, H-P.: "Synthesis of Mesoporous Silica Nanoparticles," *Chemical Society Reviews*, Vol. 42, Issue 9, 2013, pp. 3862-3875.
12. Alsmaeil, A.W., Hammami, M.A., Abdel-Fattah, A.I., Kanj, M.Y., et al.: "From Biomedical to Oil Industry:

Promising Mesoporous Materials for Oil Field Applications," SPE paper 205175, presented at the SPE Europec featured at the 82nd EAGE Conference and Exhibition, Amsterdam, the Netherlands, October 18-21, 2021.

About the Authors

Hala A. AlSadeg

B.S. in Materials Science and Engineering, Pennsylvania State University

Hala A. AlSadeg is a Petroleum Scientist working with the Reservoir Engineering Technology Team of Saudi Aramco's Exploration and Petroleum Engineering Center – Advanced Research Center (EXPEC ARC). She works on several research projects aimed at utilizing nanotechnology for enhanced oil recovery and reservoir characterization applications.

In 2018, Hala received her B.S. degree (highest honors) in Materials Science and Engineering from the Pennsylvania State University, State College, PA.

Her undergraduate research was focused on the fabrication and characterization of 2D heterostructures for sensing and electronic applications.

Ahmed Alsmaeil

M.S. in Chemical Engineering, King Fahd University of Petroleum and Minerals

Ahmed Alsmaeil is currently working on his Ph.D. degree at Cornell University where he studies modulating nanoparticles assembly at oil-water interfaces.

He has been working at Saudi Aramco since 2015. Ahmed's experience ranges from working in the Exploration and Petroleum Engineering Center – Advanced Research Center (EXPEC ARC), to working as a Reservoir and Production Engineer for the Southern Area Reservoir Management and Production Engineering departments.

Ahmed received his B.S. degree in Chemical Engineering from King Fahd University of Petroleum and Minerals (KFUPM), Dhahran, Saudi Arabia. He received his M.S. degree in Chemical Engineering from Cornell University, Ithaca, NY.

Ahmed's master's research investigated encapsulating surfactant molecules into silica nanoparticles to improve the surfactant delivery and adsorption at the oil-water interface.

Mohamed F. Alhassni

Mohamed F. Alhassni is a Lab Technician working with the Reservoir Engineering Technology Team of Saudi Aramco's Exploration and Petroleum Engineering Center – Advanced Research Center (EXPEC ARC). He joined the In-Situ Sensing and Intervention Focus Area (ISI) in January 2021.

During Mohamed's work with ISI, he has so far contributed to multiple publications, technology deployments, and one patent relevant to upstream oil and gas applications.

Dr. Amr I. Abdel-Fattah

Ph.D. in Chemical Engineering, University of New Mexico

Dr. Amr I. Abdel-Fattah is a Petroleum Engineering Consultant and Team Leader of the In-Situ Sensing and Intervention focus area in Saudi Aramco's Exploration and Petroleum Engineering Center – Advanced Research Center (EXPEC ARC). He joined EXPEC ARC's Reservoir Engineering Technology Division in late 2012 after working 16 years with the Los Alamos National Laboratory in New Mexico, U.S., where he reached a Senior Scientist status. Amr is currently spearheading a number of research and technology development programs in EXPEC ARC geared at utilizing nanotechnology for upstream oil and gas applications.

He has over 35 years of experience in subsurface energy and environmental applications of nanotechnology, colloid and interface science, and electrokinetics. Amr is a Society of Petroleum Engineers (SPE) Distinguished Lecturer, a founding Board Member of the International Association of Electrokinetics, a U.S. Representative on the International Board of Electrokinetics, a Technical Member on the Science Advisory Board of the International Association of Colloid and Interface Scientists, and a Guest Editor for the international *Journal of Colloids and Surfaces A*, and *Frontiers in Energy Research*.

He has published numerous papers in international journals, including some of the world's premier and most cited journals, and delivered numerous plenary and invited talks and lectures worldwide. Amr chaired the International Electrokinetics Conference in Santa Fe, NM, in 2008, in addition to several international workshops and conference sessions in the U.S., Canada, and Europe since 2005.

He received his B.S. degree in Civil Engineering and an M.Eng. in Geotechnical Engineering from Ain Shams University, Cairo, Egypt. Amr received his M.S. degree and his Ph.D. degree in Chemical and Nuclear Engineering from the University of New Mexico, Albuquerque, NM.

Effective Well Engineering Approach Involving Coiled Tubing, Perforation, Fracture Diversion, and Multiphase Flow Measurements to Enhance Efficiency and Maintain Production Performance

Ayman N. Alharbi, Abdul Muqtadir, Hashem A. Al-Obaid and Scott F. Ashby

Abstract /

Well completion practices in high-pressure, high temperature carbonates are challenging, especially for long lateral horizontal wells intended for fracturing applications. An integrated approach involving intervention and fracturing design and reliable post-fracturing flow measurements is very critical to optimize the well performance.

After initial intervention complexities due to wellbore accessibility in a 6,250-ft cemented lateral initially planned with 13 fracturing stages resulting in the loss of many operational days, a revamped engineering workflow was planned for Well-A. As a first step, coiled tubing (CT) was used for abrasive jetting perforations, clean out, and acid squeeze functionalities with a novel bottom-hole assembly (BHA). The BHA was equipped with a real-time telemetry to optimize intervention to a single run. Having real-time bottom-hole parameters helped in perforating the desired zones accurately, and enhanced the injectivity by creating cleaner perforation tunnels.

The number of stages were reduced to five with an optimized perforation design based on a rock typing approach, and short clusters were designed to divert the fracture fluids effectively using multimodal particulate diversion. Each fracturing stage was isolated with a mechanical plug. A novel high frequency pressure monitoring technique that analyzes fluid entry points from water hammers was utilized during the fracturing treatments to analyze on-the-fly diversion efficiency and optimize further treatments.

A multiphase flow meter (MPFM) was utilized to enhance milling and flow back to minimize losses and manage the choke schedule based on the actual well performance, leading to better fracture cleanup and recovery. The production performance of Well-A was compared with two offset horizontal wells drilled azimuthally parallel, intersecting the same carbonate sublayer. The post-fracturing absolute production enhancement analysis showed an 11% to 15% improvement, and the productivity index improvement was 40% to 63% when normalized by stage count. The effective integration of multiple technologies was applied successfully on the candidate well, yielding enhanced operational efficiency with optimized production performance.

Introduction

Development of tight gas carbonates with horizontal well completions relies to a large extent on creating multiple fractures across the lateral for production potential. Candidate Well-A is a well with a 4.5" (3.83" inside diameter) cemented lower liner that was initially planned with 13 fracturing stages across a 6,250-ft lateral length coil tube (CT) clean out, which was conducted initially with a 3.5" mill and motor in two passes with a gel sweep and bottoms up to displace the well with treated water.

A wireline was run in hole (RIH) for the stage 1 perforation with a 3.25" tractor bottom-hole assembly (BHA), but was held up 18-ft shallower than the target depth. After the wireline was freed, the CT was run again to repeat the clean out with a venturi junk basket. The run was started while pumping at 2.5 bbl/min, and the CT became locked up 200 ft shallower than the first perforation target depth. The run was continued with a friction reducer, and once clean returns were observed, the CT was pulled out of hole (POOH) to the surface.

At the surface, 110 grams of metal shavings and rust was recovered, and the entire BHA was covered in pipe dope. The clean out run was repeated with CT, following which a wireline perforation run was initiated with the same result, i.e., wireline getting stuck. The BHA was freed with an application of 50% overpull, and it was decided to run a 3.6" lead impression block BHA to investigate the obstruction.

After all these operational challenges and the loss of operational efficiency, due to a potential wellbore obstruction, a complete revamp of the engineering workflow was planned. It was decided to approach the well with

an experimental outlook to maximize the operational efficiency without impacting the production potential negatively. It was decided to:

- Switch from wireline perforation to CT abrasive jetting for stage 1.
- Run stage 1 abrasive jetting with a novel BHA, which would enable acid squeeze (if required) in the same run to save time.
- Reduce the stages from 13 down to five with an engineered perforation design.
- Utilize premium diversion chemistry and design to ensure all clusters effectively receive acid.
- Run novel diagnostic technology to evaluate the diversion efficiency stage by stage and optimize the diversion design plan.
- Utilize a flow meter for post-fracturing operations to make real-time efficient decisions.

Prefacturing CT Approach

Based on the above-mentioned accessibility challenges associated with the wireline, it was decided to perform perforations using CT. When CT is used for perforations, there is the possibility that the CT will encounter problems when it is run across the lower completion. Usually, CT with an e-line cable is deployed to perform the dummy run, and this is followed by the live gun run. Subsequently, a clean out cannot be performed efficiently if there is a need to perform a clean out during the deployment of the CT with an e-line. Additionally, the fluid cannot flow through the BHA with guns as the e-line BHAs are not flow through tools, and the fluid will exit above the logging/perforating BHAs.

Driven by the challenge to optimize the overall operation, the idea was to achieve all the objectives by utilizing the versatility of CT and its capabilities to provide a novel BHA that conducts both the clean out and perforations.

Efficiency-Based Perforation Approach

Figure 1 is the lithology profile of the pay zone for stages, where the rock type was a mixture of calcite

Fig. 1 *Well-A log montage for a 6,200-ft lateral section. Mineralogy: green represents dolomite and blue represents limestone. The porosity and permeability tracks reflect the reservoir development across the lateral, and the two rightmost tracks show the original plan of 13 stages and the revised approach with five-stage cluster designs.*

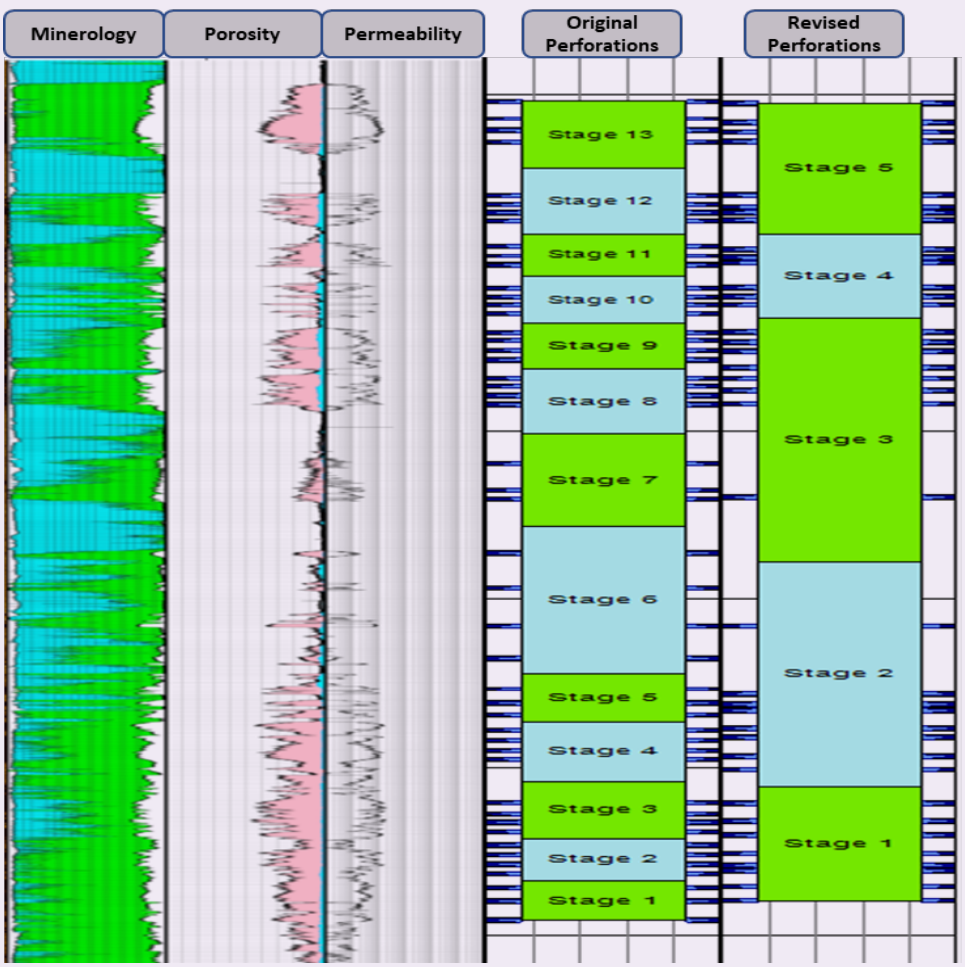

and dolomite. It is important to mention that stage 1 at the toe had to be completed in a dominantly dolomitic zone. Occasionally, when a zone is perforated using wireline guns (deployed by wireline or with CT), and when the injection is conducted in these zones, it can lead to achieving poor injectivity results, thereby requiring executing the contingency of acid and solvent spotting/squeeze. Subsequently, the use of abrasive jetting was preferred over the use of conventional perforations because the BHAs utilized for abrasive jetting can be used for conducting abrasive perforations followed by acid injection.

Additionally, in this case, one of the reasons to use abrasive perforations was the improvements observed, Fig. 2, where the injectivity improvement factor obtained by abrasive perforations were better than when the wireline perforations followed by solvent/acid squeeze were conducted.

Abrasive perforations use an abrasive jetting tool that creates holes penetrating past the near wellbore regions and enabling communication of the well with the formation. Abrasive perforations are conducted by conveying high-pressure jetting tools with CT to the desired depth and jetting the abrasive fluid to create the perforations.

Abrasive material is conveyed with gelled fluid that enables the sand to be transported back to the surface during the jetting operation. The pumping rate is adjusted to provide an approximate 2,200-psi to 2,500-psi pressure differential across the nozzle. A sufficient rate is also needed as it provides adequate annular velocity to carry the abrasive material back to the surface. Real-time downhole tools with a pressure gauge, casing collar locator, and gamma ray (GR) measurements are usually used to ensure the differential pressure across the tool is as required, to adjust the rates, to understand if the jetting nozzles are washed out, and to provide the accurate depth control.

Novel BHA Utilization

When an abrasive perforating tool is run, it has a nozzle (stationary or rotating) at its bottom. During CT RIH, the fluid is coming out of the bottommost nozzle, and when the abrasive perforations need to be conducted, then a ball is dropped to activate the abrasive perforator. After the abrasive perforator is activated, it is difficult to activate the bottommost nozzle again.

This novel BHA allows switching between the high-pressure jetting tool and the abrasive perforating tool, which allows cleaning out first, then performing the perforations followed by cleaning out again and applying acid squeeze to enhance the injectivity. The CT BHA was run with real-time downhole telemetry providing the real-time downhole parameters of pressure, temperature, and GR.

CT was RIH to the end of the tubing to perform the clean out, Fig. 3, which shows both the CT surface (top) and downhole parameters (bottom). Upon reaching the end of the tube, clean out fluids were pumped via high-pressure jet to clean the well to total depth (TD). Two clean out passes were performed and the well was

Fig. 2 *The effect of abrasive jetting in reducing the fracturing pressure and increasing rates achieved[1]; IIF indicates the injectivity improvement factor.*

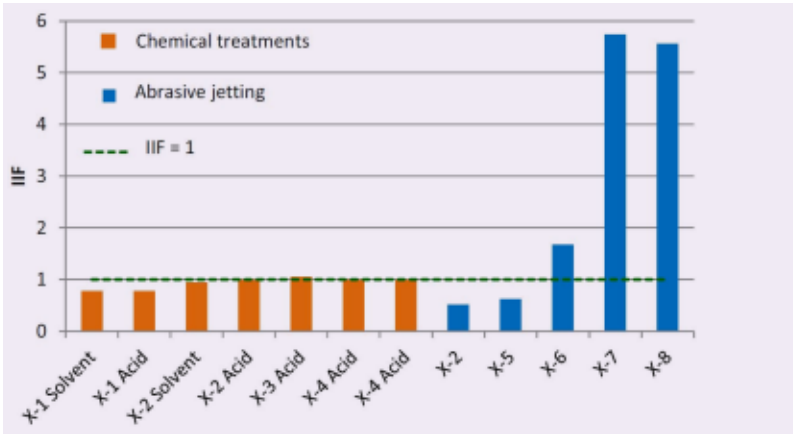

confirmed to be clean of all debris and accessibility issues. Throughout the high-pressure jetting clean out, the downhole differential pressure remained positive, i.e., CT BHP > annular BHP.

A depth correlation was then performed to ensure the slot placement, Fig. 4.

A ball was dropped and chased to the ball seat of the abrasive perforator to isolate the high-pressure jetting tool. Abrasive perforations were performed as CT was gradually POOH for each stage of the perforation following the pumping schedules. The successful evaluation of abrasive perforations is discussed later; briefly, the diagnostics showed fluid entry across all slots and that the fracturing pressures experienced during stage 1 were relatively lower in this perforated stage than in the other stages. Sixteen perforation stations were conducted, and after completing stages 8 and 16, bottoms up was conducted. After that, CT was POOH to the vertical section to drop the ball and activate the high-pressure jetting tool again, Fig. 5.

CT was POOH to the vertical section to wait for sand settling and then RIH again to TD to complete the clean out operation; later, CT was POOH above the perforations to conduct the injectivity test, Fig. 6. After the clean out, an attempt was made for a CT injection test on the well with treated water, but the injectivity was limited with the pressure reaching 7,500 psi with just 1 bbl/min. The injection was stopped, and 20% acid was spotted with CT across the perforations. The acid was then squeezed into the formation. After the acid squeeze was performed, injection treating lines were again lined up to both the CT and CT/tubing annulus for an injection test. With 0.5 bbl/min increments, the CT was able to achieve maximum injectivity of 4 bbl/min at a pressure of 8,500 psi. After a successful injectivity test, the CT was POOH to the surface.

After the tools reached the surface, a function test was conducted that showed fluid going toward the high-pressure jetting tool, and the remaining BHA

Fig. 3 *The CT operational parameters; surface (a), and downhole (b).*

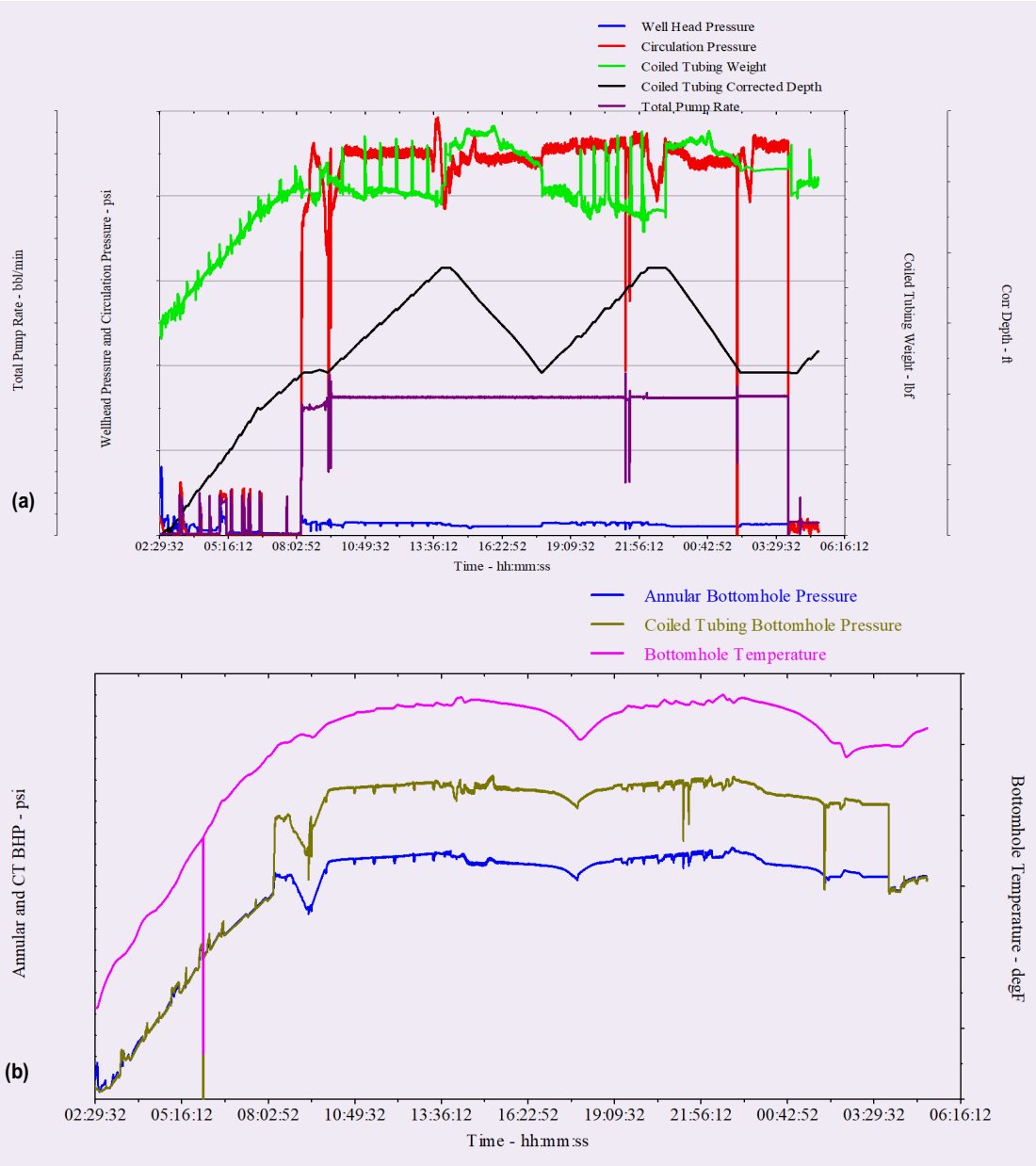

was intact with no leaks. The high-pressure jetting tool surface test before and after POOH to the surface showed the same parameters. An effective clean out performed at the polished bore receptacle led to successful wireline runs for plug and perf, which was not possible in previous trials.

Fracturing Approach

Optimizing the fracturing and diversion design were critical for the success of this completion approach where we attempted a large reduction in the stage count. The comprehensive workflow, summarized in Fig. 7, was used as a blueprint for lessons learned and future implementations.

Design and Execution

The perforation plan was the first step to be redesigned in this approach. The central idea behind decreasing stages was to increase the perforated clusters from three per stage up to eight per stage, and increase the stimulation efficiency per stage to realize the same production potential compared with the conventional approach. The cluster interval was minimized to 2 ft to achieve effective plugging with diverter materials. Perforation selection and design was done using composite indices for reservoir and completion quality calculated based on rock properties such as porosity, permeability, mineralogy, stress, etc.

Fig. 4 *The depth correlation to correct and confirm slot placement.*

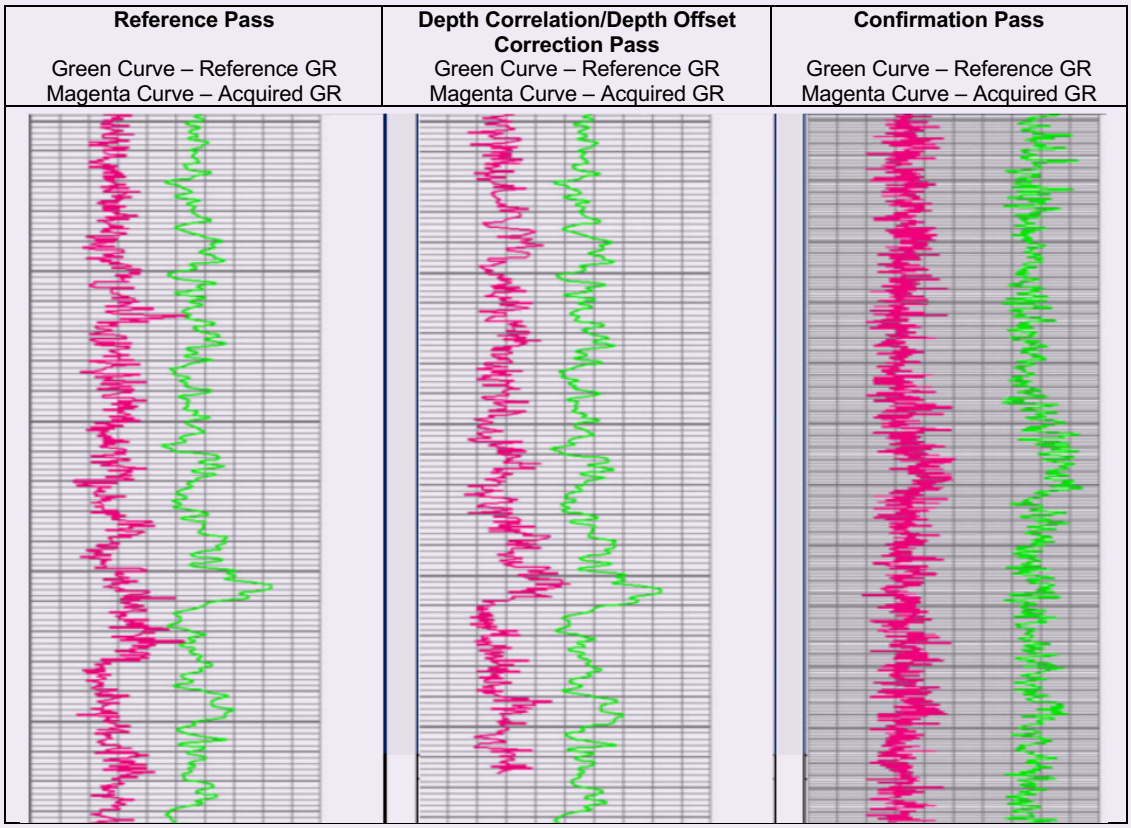

Polylactic-acid-based chemistry was utilized in multimodal bead morphology in the treatment cycles. The success of these particulates in the Middle East carbonates is detailed by Alabdulmuhsin et al. (2020)[2]. Similar approaches and case studies have been conducted in the past, but one of the differentiating factors in our study is the engineered design of diversion. We used two robust workflows to ensure the design of the diversion in terms of the number of acid diverter cycles and the amount of particulate mass sufficient for stimulating all or most clusters in the interval.

The first approach, called the β factor workflow[3], uses the system volumetrics balance to predict diverter mass required. High-resolution acid etching simulations are conducted to couple with the perforation geometry and analyze system volume, based on which a ratio (termed as β here) of particulate was added. A β of 0.79 was designed for this well to enhance chances of diversion success. The second approach was to use a very recent multiphysics numerical model[4] that can capture near wellbore diversion and predict flux redistribution based on digitized laboratory testing results of the diverter materials.

The β factor based design was run through multiple simulations in the fine-scale numerical model and showed most clusters receiving flux[5]. A detailed validation of both these approaches based on real field cases[6]. Based on the modeling and design tools, three diverter pills (particulates + linear gel base fluid), 6 bbl to 7 bbl each, were pumped in each stage, yielding a total particulate mass of 840 lbm per stage.

During the execution of each stage, the diversion pressures were noted during each pill placement to ensure sufficient pressure buildup was achieved, which is a signature of particulate skin increase in the stimulated fractures and allows for flux distribution to the unstimulated fractures.

Figure 8 shows the pressure charts for all three pill placements in stage 4. For each pill, an initial pressure stabilization can be seen indicating the spurt loss portion of the plugging, followed by a steep pressure spike of 1,280 psi, 1,460 psi, and 790 psi, respectively, for the pills. For the third pill, the pressure derivative was steep enough that it required a drop-in rate of 3 bbl/min to 4 bbl/min. The average diversion pressure in all stages across 15 pills was 1,012 psi with a maximum of 1,610 psi for one of the pills in stage 2.

Near Real-Time Diagnostics

Besides pressure analysis, a novel technology was used for validating the diversion efficiency. The tube-wave velocity is analyzed based on the water hammers to yield the fluid entry point. The pressure wave generated

Fig. 5 *The depth correlation to correct and confirm slot placement; surface (a), and downhole (b).*

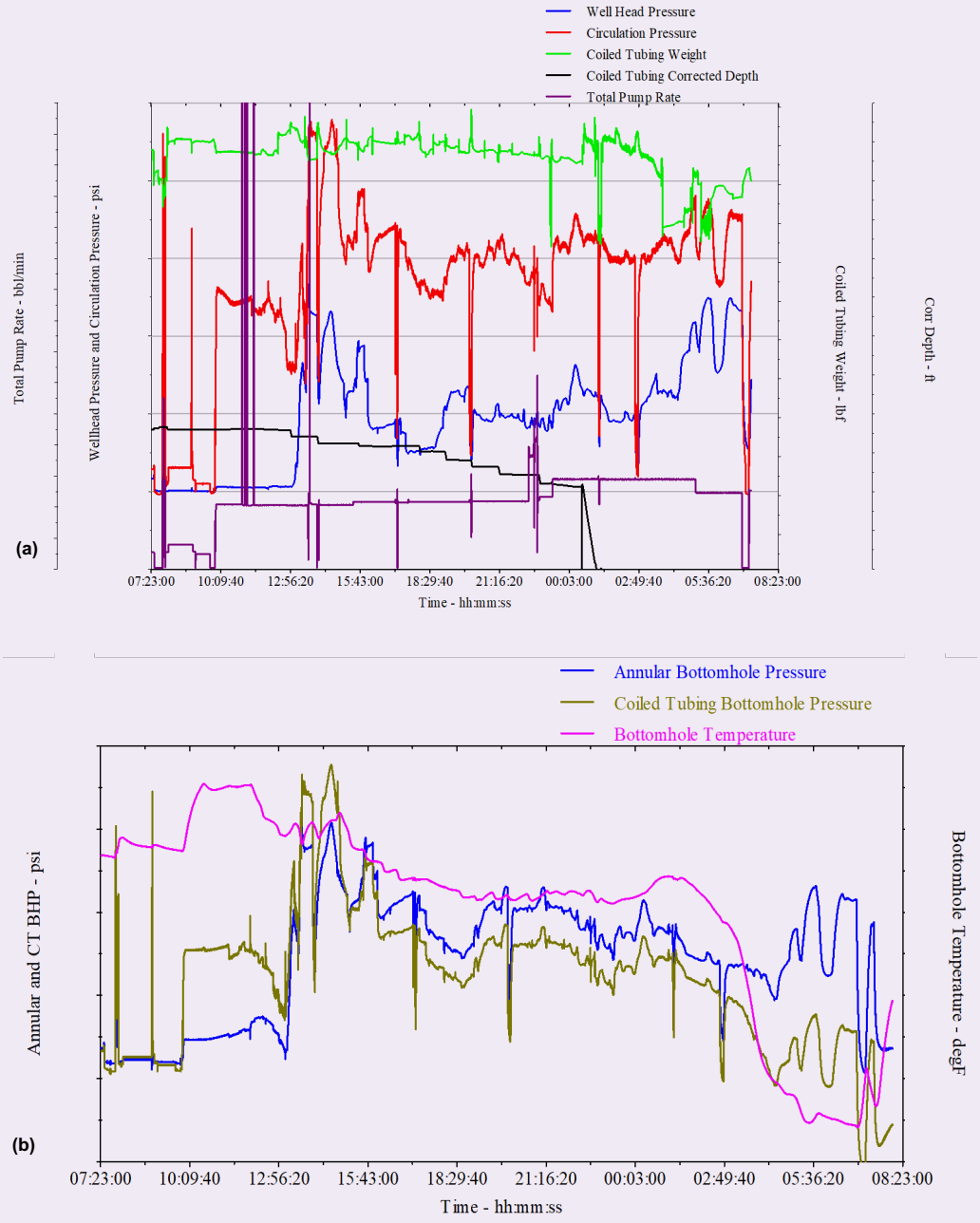

by the water hammer reflects off objects within the well and travels to the surface at different times. The longer the reflection time, the deeper the object, Fig. 9.

Figure 10 shows the display for all the events analyzed for multiple stages. Each blue cloud represents an event or water hammer that was analyzed by this algorithm. As we move from left to right, we go from stage 1 through stage 5 and different diversion cycles within each stage. The size of the cloud shows the resolution, and the intensity of the blue spectrum shows the probability of fluid entry point existence at that particular depth. Even with large stage intervals — distance between top and bottom cluster of each stage — the resolution of the fluid entry points analyzed was well within 80 ft.

The quality of the water hammer is critical for the fluid entry point prediction; therefore, multiple events were used for each stage because not all events produce a strong water hammer, especially after acid etching, which made it difficult to calculate the reflection times. Overall, the algorithm confirmed full stage interval coverage across different diverter pills. The sequence of clusters stimulated was also analyzed in correlation with rock mineralogy, and stress was found to be as

Fig. 6 *The injection test pumped through CT post-abrasive jetting to evaluate rates and pressures. The plot shows pressure maximum out at a low rate followed by acid squeeze and a repeat injection test with a higher rate achieved.*

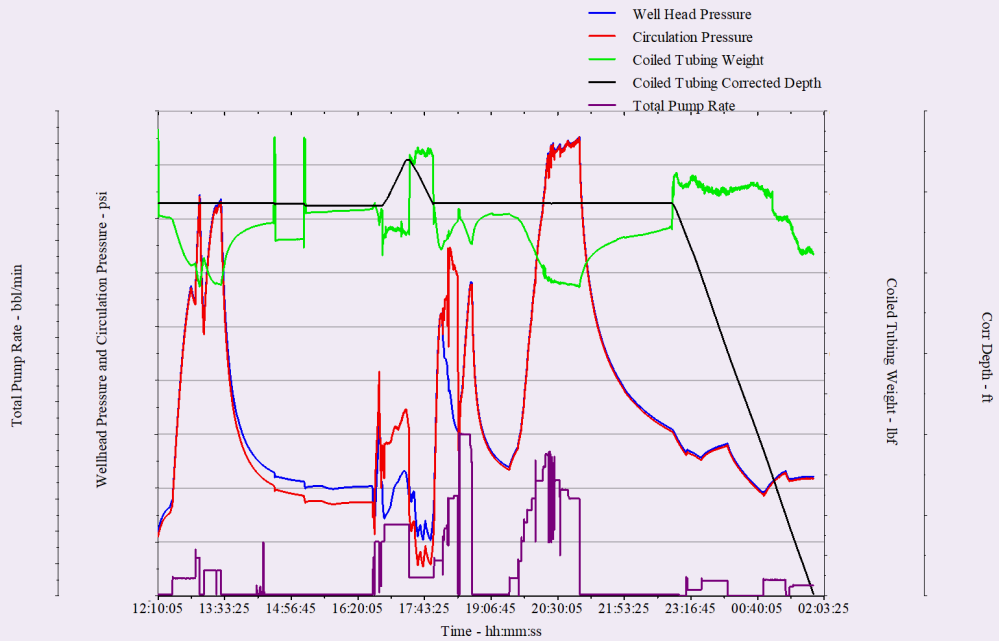

Fig. 7 *The engineered workflow for fracturing design to ensure fracture diversion success.*

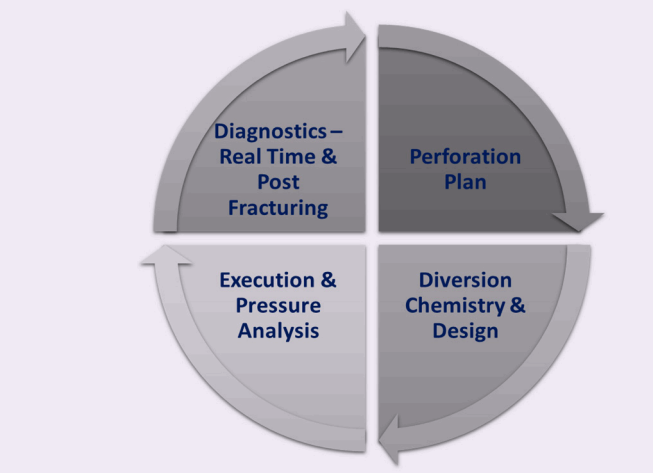

per the intuitive understanding.

Stage 4 showed interstage communication with stage 3 as per the water hammer analysis, which was also validated with the comparison of fracture pressure falloff. In this stage, the diverter was shown to be especially helpful to plug communication with stage 3 and stimulate stage 4[5].

Post-Fracturing Interventions

An efficient well engineering workflow requires attention to post-fracturing activities to ensure proper management aspects, such as wellbore access and production performance. The first common step in this phase is the plug drill out and fracture seat milling in cased hole and open hole multistage completions, respectively. This is followed by well flow back operations, which ensure fracture cleanup, recovery of foreign fluids from the formation, and well potential evaluation.

Usually, these operations rely on certain practices that could be flawed and affect the well negatively or lower the operational efficiency due to delayed decision making. In this well, a multiphase flow meter (MPFM) was used to optimize post-fracturing activities[7].

Plug Drill Out Operations

CT utilization for milling out the isolation plugs is common for all horizontal completions and is a critical operation to be optimized due to the high number of variables and uncertainties associated with reservoir and wellbore condition. Pumping in water during this operation can negatively affect the fracturing treatment by introducing rock destabilization at the wellbore connection, risk of scaling, etc. These challenges are accentuated further in proppant fracturing treatments due to the damage and destabilization of the proppant pack[8]. At the start of milling, we defined a differential rate (dQ) as dQ = Total CT rate (going in) – MPFM measured return rate (coming out).

Figure 11 shows how the MPFM was used when the start of milling saw a positive dQ of ~0.3 bbl/min (430 bbl/day), indicating a loss of water in the formation. Extrapolating from this trend, an average well requiring

Fig. 8 *The rate and pressures for the diversion pill response for three pills in stage 4 showing the pressure spikes. The green marker shows the particulate pill arrival at the perforations.*

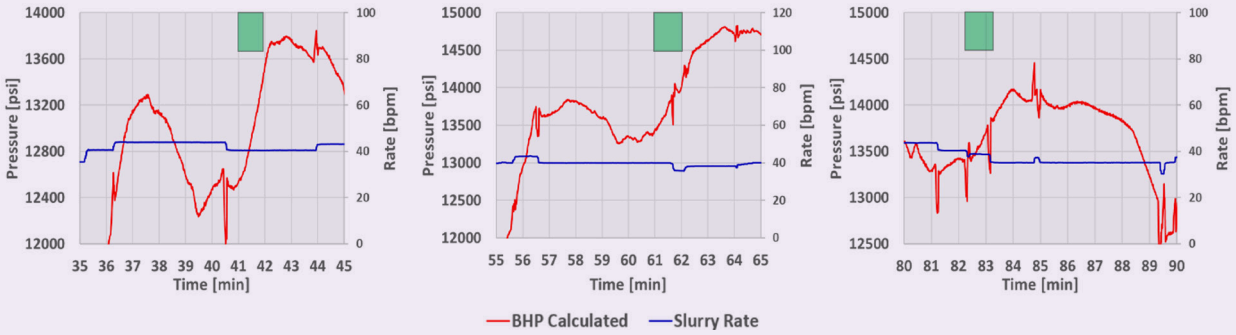

Fig. 9 *The physics behind the water hammer analysis yielding reflection time and depth; BP indicates the bottom plug.*

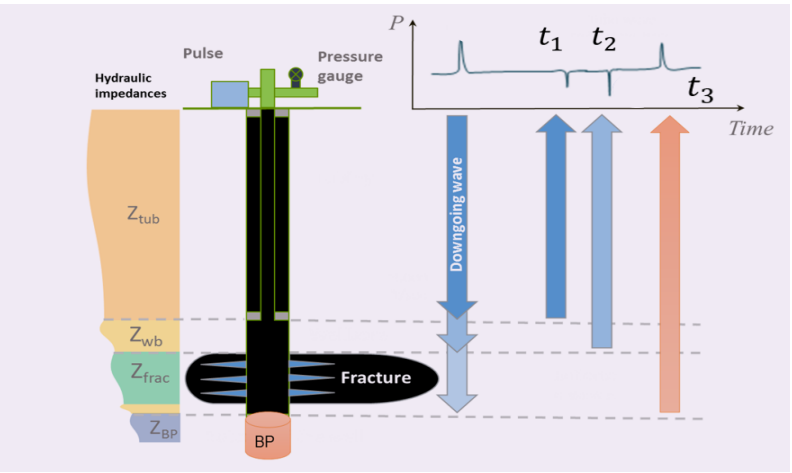

3 to 4 days for a mill out operation would inject more than 1,700 bbl of water in a stimulated well, exacerbating the formation damage scenario and requiring a longer time to clean up the extra fluid injected. An engineered decision was possible here due to the measured return rate, and the backpressure on the well was managed through choke opening, which was increased from 18/64" to 22/64" and later even to 24/64" to maintain a balanced condition where $dQ = 0$.

This operational condition is very critical but difficult to maintain. Whereas a positive dQ would imply fluid losses in the formation, a negative dQ can result in surface equipment issues for handling reservoir fluid returns. In addition to the choke management, the water and gas rates were measured during the entire milling operation to ensure the well is flowing gas and there is no need for a nitrogen kickoff to lift the well. Payne et al. (2021)[9] also detailed a case study of a digital monitoring system that accounts for returns, annular velocities, bottom-hole Reynolds number, etc., to provide a visual guide to optimize CT operations, including milling.

Flow Back and Fracture Cleanup

The use of the flow meter yielding actual rates of the different fluid phases enabled better choke management and efficient cleanup where the choke bean-up and bean-down decisions were taken based on the continuous changes in the actual return water rate, which eliminated the waiting time for flow stabilization. Figure 12 shows the measured transient rates for different phases that were monitored along with the choke opening changes to ensure the trends of increasing gas rate and decreasing water rate were observed.

Figure 13 shows a summary of how engineered decision making can be used with the flow back metrics. The water-gas ratio (WGR) parameter was calculated and can be seen for three regions demarcated based on the slope changes, which can be used for describing the cleanup phases. All the following inferences are usually made based on the changing flowing wellhead pressure (FWHP) used as a proxy to detect the changes in transient flow regimes. Moreover, it can be seen here that the FWHP parameter is not as descriptive as needed and could be potentially misleading for decisions.

- Region 1 shows the initial choke opening, which is marked by a sharp spike in the WGR at each choke opening. This can be understood as surges being created extract slugs of water in the gas flow. These peaks (surges) actually aid in better water recovery.
- Region 2 is marked by loss of the surging effect at choke openings beyond 34/64", which indicates a slowing of the cleanup process. The slope is still declining at a good rate in this region, and fluid recovery is good.
- Region 3 shows the change of cleanup behavior at choke openings of 40/64" and beyond. The WGR decline rate declines drastically (almost flow stabilization), which is indicative of a fluid recovery cap, and therefore, is an important point for evaluation, which was conducted along with the fluid recovery factor.

The decision to conclude the cleanup must be made by investigating the fluid recovery factor calculations; these can then be used to estimate the total recovery

Fig. 10 *The water hammer analysis results summary for stages 1 through 5 (left to right) and within each stage proceeding from the first acid cycle to last (left to right). The blue clouds indicate the fluid entry point analysis in the particular event, and the size of the cloud represents the depth resolution and the blue spectrum intensity gives the probability/confidence of the depth prediction.*

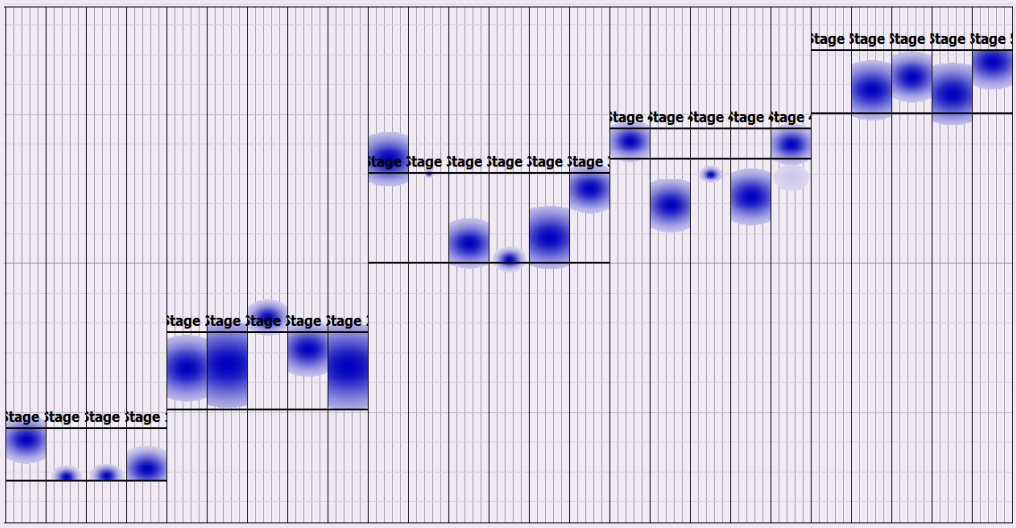

Fig. 11 *The flow rate and choke management enabled by flow metering to ensure a balanced condition and no losses of fluid in the formation. The green highlight shows the CT rate out increased to make dQ = 0 bbl/min, and the red highlight shows an unfavorable dQ.*

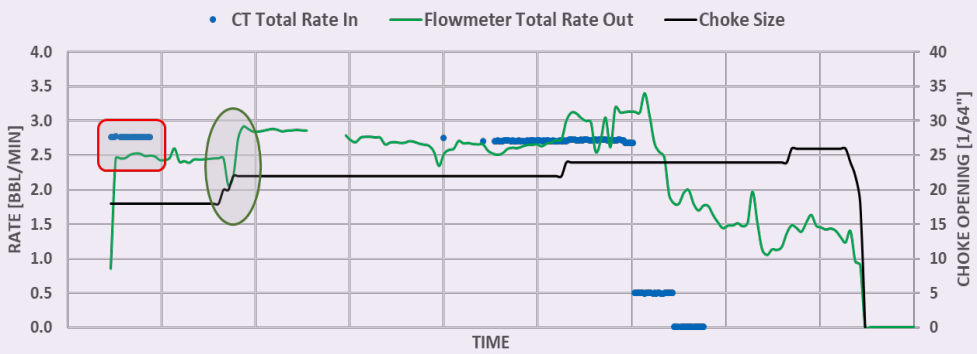

Fig. 12 *The normalized liquid and gas rates measured with the MPFM showing trends through the fracture clean up, well productivity, and deliverability evaluation phases. The dashed lines show the trends of the fluid rates through different phases of flow back.*

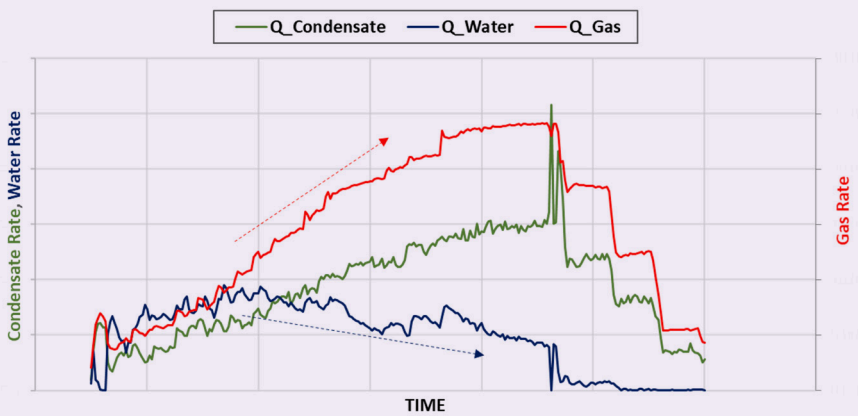

Fig. 13 *The WGR and FWHP trends during the fracture cleanup and well potential evaluation phases investigated through the choke bean-up and bean-down practice. The highlighted shapes are based on the changing WGR trends and indicate three regions of fracture cleanup.*

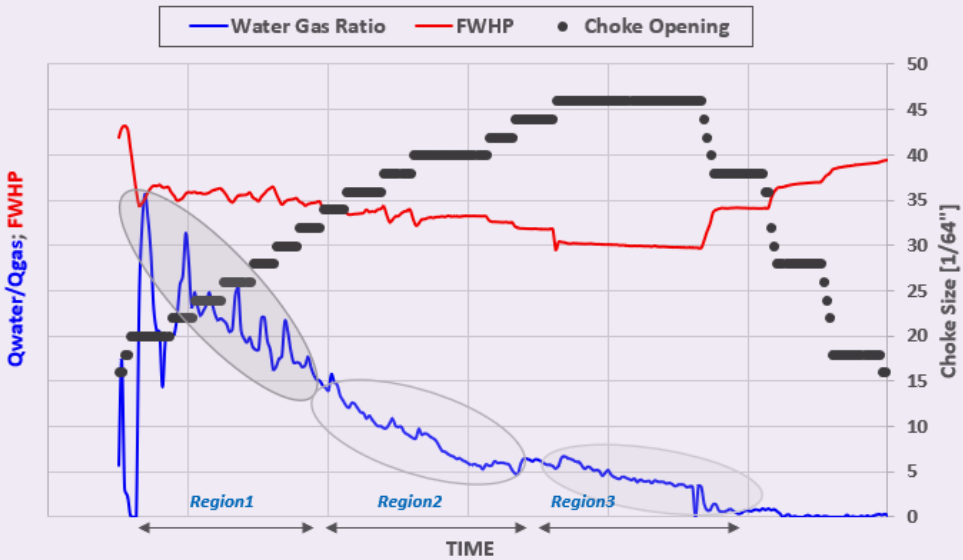

time based on stabilized water recovery rates. Figure 14 shows two recovery factors (RF) — one calculated based on the total water pumped during fracturing treatments and the other accounting for all treating fluids, including water and reactive fluids. Both of these factors give the upper and lower boundaries, and the actual RF lies closer to the upper boundary depending on actual stoichiometry dynamics (Appendix A).

Therefore, for the candidate well, the RF in region 3 was calculated between 19% and 34% (realistically around 30%), and the estimated time to reach 100% was between seven and 17 days based on the final stabilized water rate of 600 bbl/day. The large fraction of water unrecovered varies for different reservoirs depending on multiple factors such as fluids mixing with formation water, retention due to interfacial tension, cation exchange, uneven production from zones, etc.

Production Validation

Production performance comparison with offset wells is another robust validation of achieved stimulation efficiency. Wells B and C are offset horizontal wells with similar lateral lengths drilled parallel and within a 3-km bottom-hole distance from Well-A. Well-B was completed with 12 stages in a cemented well and

Fig. 14 *The water flow rate along with the fracturing fluid recovery fraction along the flow back phases. The black curve calculates the recovery based on water-based fluids injected in the formation during fracturing and CT operations. The red curve calculates the recovery based on all treating fluids (waterbased + reactive fluids) injected in the formation.*

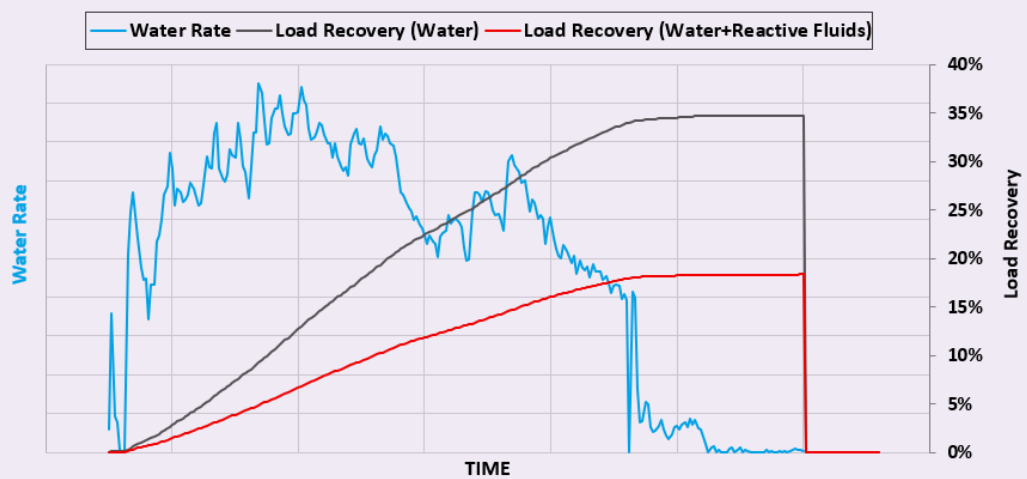

Fig. 15 A production comparison summary with Wells B and C showing flow back parameters (a), and normalized productivity (b).

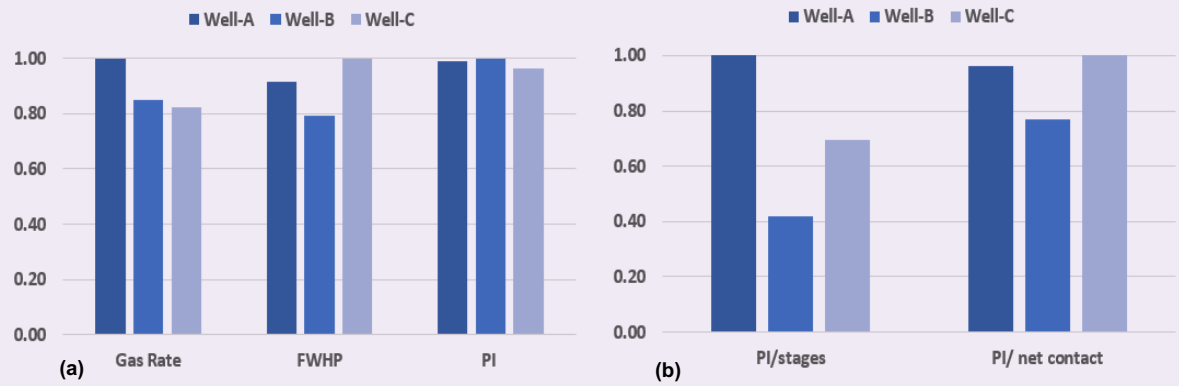

Well-C with seven stages in an open hole well with packers and fracturing sleeve.

In these types of completions, each stage develops multiple fractures, up to nine in some intervals as analyzed by a sonic noise log. After the flow back and well potential evaluation with the MPFM, the productivity index was compared using the gas rates and pressures after fracture cleanup was achieved.

Based on the analysis shown in Fig. 15, it is evident that Well-A shows similar stimulation efficiency as the offset horizontal wells effectively treated with a few folds higher number of stages.

Conclusions and Summary

1. The completion practices for the candidate well (Well-A) was optimized at each step of the workflow in prefracturing intervention, fracturing treatments, and post-fracturing interventions. This utilized techniques and technology implementation from CT, perforation, fracturing, chemistry, plug milling, and surface well testing disciplines.
2. The versatility of CT in this operation was proven to be capable of achieving multiple objectives and maximizing the outcome of a single run. The well was successfully cleaned, perforated, and a mini stimulation was conducted to improve the injection index prior to the planned acid fracturing operation.

   By combining several existing technologies with an innovative approach, we were able to avoid delays to the well completion workflow.

   a. First and last clean out, using a high-pressure rotating jetting tool and abrasive perforations were performed successfully.
   b. A real-time downhole tool was successfully utilized to conduct the GR correlation in real-time.
   c. During the abrasive perforations, real-time downhole pressure readings played a key role in understanding the downhole conditions and abrasive perforations behavior.
3. The operational efficiency of the entire well engineering was condensed by technologies such as:
   a. A novel BHA for CT abrasive jetting to be able to squeeze acid in the same run.
   b. Reducing the stage count by 62% from 13 down to five successfully by engineering perforation design, diversion chemistry, diversion design, and novel non-intrusive diagnostics.
   c. A MPFM, which allowed the reduction of losses during milling, and therefore, less water to recover during cleanup.
   d. A MPFM for fracture cleanup allowed for choke management and a precise timeline for cleanup and well potential evaluation.

Acknowledgments

This article was prepared for presentation at the SPE Asia Pacific Oil and Gas Conference and Exhbition, Adelaide, Australia, October 17-19, 2022.

References

1. Guizada, P., Rahim, Z., Al-Kanaan, A., Al-Rashed, A., et al.: "Best Practices in Pre-Fracturing Coiled Tubing Intervention Operations Increase Success Rate of Hydraulic Fracturing Treatments," SPE paper 184790, presented at the SPE/ICoTA Coiled Tubing and Well Intervention Conference and Exhibition, Houston, Texas, March 21-22, 2017.
2. Alabdulmuhsin, A., Alkulaib, H., Hansen, J. and Khan, A.M.: "Self-Degradable Particles Mitigate Communication between Stages in Multistage Acid Fracturing Completion," SPE paper 202612, presented at the Abu Dhabi International Petroleum Exhibition and Conference, Abu Dhabi, UAE, November 9-12, 2020.
3. Khan, A.M., Usova, Z. and Yudin, A.: "Integrated Workflow with Experimentation, Modeling, and Field Implementation Framework Enhances Fracture Diversion Understanding in Carbonate Reservoirs," SPE paper 205665, presented at the SPE/IATMI Asia Pacific Oil and Gas Conference and Exhibition, virtual, October 12-14, 2021.
4. Khan, A.M., Emelyanov, D., Romanovskii, R. and Nevvonen, O.: "Advanced Modeling Capability to Enhance

Near Wellbore and Far-Field Bridging in Acid Fracturing Field Treatments," SPE paper 206255, presented at the SPE Annual Technical Conference and Exhibition, Dubai, UAE, September 21-23, 2021.

5. Obaid, H., Khan, A.M., Hansen, J., et al.: "Maintaining Stimulation Efficiency with Significantly Fewer Stages: Perforation Strategy Combined with Multimodal Diverters and Novel Non-Intrusive Monitoring Method," SPE paper 210472, prepared for presentation at the SPE Annual Technical Conference and Exhibition, Houston, Texas, October 3-5, 2022.

6. Almulhim, A.A., Hansen, J., Khan, A.M., Emelyanov, D., et al.: "Validation of a Novel Beta Design Factor for Enhancing Stimulation Efficiency through Field Cases and Near Wellbore Diversion Model," SPE paper 210439, prepared for presentation at the SPE Annual Technical Conference and Exhibition, Houston, Texas, October 3-5, 2022.

7. Lomukhin, A. and Rymarenko, K.: "Experience of Multiphase Flow Measurement Systems Application in Arctic Conditions," SPE paper 149922, presented at the SPE Arctic and Extreme Environments Conference and Exhibition, Moscow, Russia, October 18-20, 2011.

8. Potapenko, D.I., Williams, R.D., Desroches, J., Enkababian, P., et al.: "Securing Long-Term Well Productivity of Horizontal Wells through Optimization of Post-Fracturing Operations," SPE paper 187104, presented at the SPE Annual Technical Conference and Exhibition, San Antonio, Texas, October 9-11, 2017.

9. Payne, C., Yip, W., Fajardo, S.R. and Leroux, R.: "Benefits of Digital Monitoring of Flow Back Returns during Coiled Tubing Milling and Cleanout Operations," SPE paper 204409, presented at the SPE/ICoTA Well Intervention Conference and Exhibition, virtual, March 22-25, 2021.

Appendix A

The calculation for total water available for recovery is complex when considering acid fracturing or matrix acidizing treatments. Acid fracturing has water-based fluids such as treated water (preflush, postflush, etc.), cross-linked systems used as pad fluids, and reactive fluids such as different acid systems. Acid reaction with carbonate reservoir systems broadly follow the below reactions:

$$CaCO_3\,(s) + 2HCl\,(aq) \rightarrow CaCl_2\,(aq) + CO_2\,(g) + H_2O \quad (1)$$

$$CaMg(CO_3)_2\,(s) + 4HCl\,(aq) \rightarrow CaCl_2\,(aq) + MgCl_2\,(aq) + 2CO_2\,(g) + 2H_2O \quad (2)$$

The above two expressions show the stoichiometric relations for the reaction of limestone (reaction 1) and dolomite (reaction 2) minerals with hydrochloric (HCl) acid. The water/liquids resulting from these reactions depend on byproduct salts (calcium chloride, magnesium chloride) and water. The salts have a high solubility in spent acid and do not pose any risk of precipitation and potential damage to the reservoir.

The amounts of water then depend on the molar masses of the components. Table A-1 shows the quantities of reactants and byproducts using 15% HCl acid and limestone, which follows reaction 1. These quantities can then be converted to volume based on the solution densities, etc.

The actual real field case calculations become more complex based on some of the following factors:

- Different HCl acid strengths.
- Rock fraction distribution of calcite, dolomite, anhydrite, etc.
- Acid systems such as emulsified acids, viscoelastic acids, and fiber laden viscoelastic acids.
- Acid spending process.

Table A-1 *The quantities of reactants and byproducts.*

HCl	$CaCO_3$	$CaCl_2$	CO_2	H_2O
1,000 gal	1,846 lbm	2,121 lbm	6,616 scf	343 lbm (41 gal)

About the Authors

Ayman N. Alharbi

B.S. in Petroleum Engineering, University of Portsmouth

Ayman N. Alharbi joined Saudi Aramco in 2014 as a Petroleum Engineer. He works in the South Haradh Gas Production Engineering Unit of Saudi Aramco's Southern Area Production Engineering Department.

During Ayman's eight years of service, he has had several different work assignments and his work experience includes production optimization and monitoring, stimulation, completion, well service and management systems.

Ayman is a member of the Society of Petroleum Engineers (SPE). He became a certified SPE Engineer in 2021.

In 2014, Ayman received his B.S. degree in Petroleum Engineering from the University of Portsmouth, Portsmouth, U.K.

Abdul Muqtadir

M.S. in Petroleum Engineering, University of Texas at Austin

Abdul Muqtadir joined Schlumberger in Houston in 2013 and was moved to Saudi Arabia in 2015. He is working as a DESC Engineer with the Saudi Aramco Production and Reservoir Engineering teams. Abdul's main objectives are to drive production enhancement for Saudi Aramco gas wells through production analysis and new technology solution portfolio implementation.

He has coauthored multiple technical papers.

Abdul received his M.S. degree in Petroleum Engineering from the University of Texas at Austin, Austin, TX.

Hashem A. Al-Obaid

B.S. in Petroleum Engineering, King Fahd University of Petroleum and Minerals

Hashem A. Al-Obaid is a Gas Reservoir Engineer working in the South Ghawar Gas Reservoir Management Division of Saudi Aramco's Gas Reservoir Management Department.

He joined Saudi Aramco as a Gas Production Engineer in 2013. Since then, Hashem has been involved in completing gas wells in both carbonate and sandstone reservoirs, with experience in coiled tubing, wireline, well integrity and pumping.

He is an active member in the Society of Petroleum Engineers (SPE). Hashem is a certified SPE Petroleum Engineer.

He is the author and coauthor of several papers and presentations.

Hashem received his B.S. degree in Petroleum Engineering from King Fahd University of Petroleum and Minerals (KFUPM), Dhahran, Saudi Arabia.

Scott F. Ashby

M.S. in Engineering Science, University of New South Wales

Scott F. Ashby is a Senior Production Engineer in the Gas Completion and Stimulation Unit of Saudi Aramco's Southern Area Production Engineering Department. He has been with Saudi Aramco since 2012, specializing in well interventions, integrity, completions, and stimulation.

Prior to joining Saudi Aramco, Scott worked with Halliburton as a Well Intervention and Stimulation Technical Professional and Operations Manager.

He received his M.S. degree in Engineering Science from the University of New South Wales, Sydney, New South Wales, Australia.

Preparation and Selection of Best Performing Fluorescent-Based Tracers for Oil and Gas Downhole Applications

Vladimir Khmelnitskiy , Dr. Nouf M. AlJabri and Dr. Vera Solovyeva

Abstract /

Cost-effective tracers with fast and simple detection and quantification methods at low detection that limits via on-site detection is a current industrial target for state-of-the-art tracers' tests. To bridge the gap between the desired tracers' properties and detection limits, we developed a broad spectrum of robust cost-effective fluorescent tags to innovate the current reservoir management practices. We engineered new tracers and extended tracer test applications for on-site real-time well drilling monitoring to label drill cuttings as they are made at the drill bit face to improve drill cuttings' depth correlation.

These developed fluorescent tracers not only have a low detection limit of fluorescent spectroscopy techniques, but also allow for the automated detection at minimal concentrations of 0.025 mol% to 0.037 mol%. These developed tracers open the horizon to detect in real-time the drilling depth to enhance the hydrocarbon recovery. Therefore, the reported innovative fluorescent tracing approach would: (1) reduce the drilling depth correlation uncertainty, (2) optimize well placement, and (3) maximize oil production.

Introduction

The application of tracing technology in the oil and gas industry has been utililized over a 70-year period. Tracers are materials that are used in the tracing technology, including isotopes[1], dyes[2, 3], chemical tracers, microelements[4], ions[5], nanoparticles[6], and gases, including noble gases[7].

They are used as a monitoring and surveillance tool to obtain the information about the reservoir along with other methods such as production rate of reservoir fluids, 4D seismic, and pressure tests[8]. Tracers provide very informative data especially in the complex reservoirs where other techniques could be complicated to use. Obvious information available from tracers in downhole conditions is direct proof of communication in the connected pore space of the reservoir, determination of the underground fluid's directional pathways, oil saturation, and well-to-well connectivity. Also, tracers are used to obtain a better understanding about the formation as the tracers are typically added to the injection fluids, water, or gas, to track the fluid movement inside the reservoir or between reservoirs. Accordingly, tracers are commonly applied to two major types of oil field tests — these are interwell tracer tests and the single well tracer tests (SWTT)[9].

A SWTT is performed around the borehole area (up to 10 m) as a partitioning and water tracers' injection followed by their back production after certain shut-in time. During the shut-in period, the injected partitioning tracer miscible with oil and water phases, overcome partial hydrolysis in formation brine to form secondary tracer miscible with water only. The difference in arrival times of partitioning and secondary tracers is proportional to the oil and water phases ratio downhole. Such test provides information on the residual oil saturation of the formation[10, 11]. Additionally, the formation permeability profile along the borehole can be estimated via the single-well tracer method through the injection of tracers with their consequent in situ measurements.

This technique can be further applied for quality control over cementing and packing operations; this way, detection of the well leakage and formation fractures could be performed. The examples of compounds that are used for SWTT as a partitioning tracer include esters (such as ethyl acetate, propyl formate, etc.); water tracers include dyes, alcohols (isopropanol, methanol, etc.) tritiated water, and gases (radon, carbon dioxide, noble gases, tritiated water steam, and many others)[8].

The partitioning interwell tracer test is performed as an injection of passive and partitioning tracers into the injection well followed by the tracers' propagation and monitoring of their production from the production well via produced fluids sampling and characterization. Propagation of partitioning tracers progresses with chromatographic retardation due to their equilibration with water and oil phases. These tests provide information on distant (hundreds of meters) interwell space characteristics such as reservoir residual oil saturation, communication between wells, reservoir porosity and heterogeneity, fluids flow paths, and hydraulic fracturing efficiency.

Some examples of passive tracers used for interwell tests include water-soluble chemicals[8] such as solvents (methanol, ethanol, n-/isopropyl alcohol, acetone), dyes (fluorescein, rhodamine), halogen- and other ions (Cl^-, I^-, SCN^-, $[Co(CN)_6]^{3-}$), substituted benzoic- and fluorobenzoic acids and isotopically labeled water (HTO, D_2O, $H_2{}^{18}O$). Tert-butanol, 2-propanol, tritiated n-butanol, ^{14}C-tagged iso-amyl alcohol and other C_{4+} long chained and branched alcohols could be mentioned as partitioning interwell tracers[9]. The non-partitioning interwell tracer test serves for the well connectivity and fluid flow studies, and implies injection of passive tags into the injection well (one specific tracer per well) and their consequent detection and monitoring at the observation or production well[12].

Along with conventional use of the tracing technique for well production surveillance and fracturing monitoring, tracers could be applied for the tracking of the well drilling progress, drilled formation characterization, and mud logging procedures. Therefore, it was reported that the addition of tracers to drilling mud allows for the estimation of the formation water composition[13]. Moreover, barcodable polymeric nanoparticles were applied for the drill cuttings labeling at the depth of their generation to improve lithological characterization of the formation and the cuttings' depth assignment upon the cuttings return[5].

Efficient chemical tracers require an indicator to possess and enable tracking by the unique chemical composition or unique property. Therefore, identification of radioactive isotope tracers could be done through their radioactivity via gamma ray logging or scintillation counting, the detection of gases, solvents and alcohols could be performed by their standard retention times via gas chromatography (GC) or gas chromatography-mass spectrometry (GC-MS) and/or high performance liquid chromatography (HPLC).

Chemicals such as fluorobenzoic acid derivatives could be analyzed by the presence of fluorine-atom via nuclear magnetic resonance and/or by molecular weight and retention times via HPLC-MS. Ions are commonly monitored and quantified using ionic chromatography (IC); heavy atoms and metal containing ions could be tracked by inductively coupled plasma atomic emission spectroscopy or by inductively coupled plasma mass spectrometry. All named tracer-based well monitoring methods require usage of expensive equipment and often time-consuming and labor-intensive sampling, probe preparation, and analytical techniques.

The main purpose of the current work was the design of easily detectable tags for drill cuttings labeling. To develop a fast, efficient, and simple tracing method, we engineered a novel type of fluorescent tracers and aimed these tracers' applications for on-site near real-time well drilling monitoring to label drill cuttings as they are made at the drill bit face and their identification upon cuttings sorting at the shale shaker to improve on-site drill cuttings depth correlation.

Knowing the simplicity and very low detection limit of fluorescent materials, we engineered several tracers composed of carrier matrices doped or covalently modified with various commercial fluorophores to determine these tracers' robustness for harsh downhole conditions and the possibility of their visual detection by the fluorescent emission under UV light.

Materials and Methods

Materials

The poly(vinyl alcohol) (PVA) fully hydrolyzed (M_W approximately 145,000); fluorescein isothiocyanate (FITC); fluorescein; Rhodamine B; SiO_2 high purity grade, average pore size 60 Å (52-73 Å), 70-230 mesh, 63-200 µm, for column chromatography; HPLC grade solvents: methanol; propanol-2; dimethyl sulfoxide (DMSO); pyridine; tetrahydrofuran (THF); and diethyl ether were purchased from Sigma Aldrich. Commercial superabsorbent polymer (SAP) based on sodium polyacrylate (Product #C001B1) was purchased from Orbeegun (Russia). Glutaraldehyde, 50% aqueous solution (Cat. #00001602) was purchased from Ruschim (Russia). Chitosan (water-soluble, MW 50-80 kDa, degree of deacetylation DD 80%) was purchased from Bioprogress (Russia). RADGLO® PS-11, green thermoset fluorescent pigment was purchased from Afaya (Russia). All materials and solvents were used without further purification. All aqueous solutions were prepared with deionized water (18.2 MΩ*cm), from Sartorius AG, using the Arium® Mini Plus benchtop combined water purification system.

Synthesis of FITC Labeled Chitosan

Chitosan (300 mg, 0.19 mmol) was dissolved in water (15 ml) under vigorous stirring at room temperature over ~3 hours. To the obtained solution, FITC (1.48 mg, 0.0038 mmol) dissolved in ethanol (25 ml) was added dropwise. The ratio of the reacting chemicals: FITC to *d*-glucosamine residue of chitosan was chosen to be 1:50. The reaction between FITC and chitosan proceeded for 2 hours at 50 °C in the dark to prevent fluorophore from photobleaching and yielded FITC labeled chitosan.

The product was precipitated from the reaction mixture with acetone (30 ml) and recovered by centrifugation. Purification of the obtained product was performed by dispersing the resulted off-white solid in acetone (30 ml) followed by centrifugation (three times). The resulted precipitate was freeze-dried to remove residual water to yield light yellow powder of fluorescein tagged chitosan (255 mg, 85%).

Synthesis of Pigment Loaded Chitosan-Based Hydrogel

Chitosan (460 mg, 2.86 mmol) was dissolved in water (19.54 ml) under vigorous stirring at room temperature over 3 hours. To the obtained solution, commercial pigment (50 mg) in powder form was added. The mass ratio of the pigment to chitosan was 1:10. The resulted mixture was transferred to a Petri dish followed by treatment with 50% aqueous glutaraldehyde (0.2 ml, 1 mmol). The produced hydrogel was dried in a vacuum oven at 50 °C overnight to yield fine powder of cross-linked chitosan (600 mg, 98%).

Synthesis of FITC Labeled PVA

The PVA-FITC adduct was synthesized[14]. PVA (300 mg, 0.68 mmol) was dissolved in DMSO (8 ml) containing (50 µL, 0.63 mmol) of pyridine, then a solution of FITC (50 mg, 0.13 mmol) in DMSO (1 ml) was added, and the mixture obtained was heated for 2 hours at 95 °C at the dark. (It was important to keep the reaction in the dark to prevent FITC photobleaching). After 2 hours, the reaction mixture was cooled down to room temperature and propanol-2 (30 ml) was added to remove any excess of FITC into solution and to precipitate the resulted FITC-PVA adduct.

The solid product was separated via centrifugation and further purified via dispersing in propanol-2 (30 ml) followed by centrifugation — three times, until an absence of the fluorescent signal of the supernatant solution in UV light. The resulted powder of the product was transferred to a beaker protected from light with aluminum foil and dried in a vacuum oven at 40 °C overnight. FITC labeled PVA was obtained as a yellow powder (273 mg, 92%).

General Procedure for Preparation of Dye Loaded Tracers (SAP and SiO_2)

Fluorescent dye (fluorescein or Rhodamine B) (10 mg) was completely dissolved in water (200 mL for SAP; 20 ml for SiO_2) under vigorous stirring for 2 hours at room temperature. To the obtained solution, SAP (5 g) or SiO_2 (5 g) was added, and the resulted mixture was kept for 4 hours at room temperature without steering to complete dye absorption into the matrix. Upon exposure to a dye solution, SAP or SiO_2 particles soaked fluorophore. The resulted wet tracers were dried over 24 hours at 70 °C under vacuum — 10 mbar. Four batches of fluorescein (or Rhodamine B) loaded SAP (or SiO_2) were obtained with the ratio of fluorophore to matrix 2 mg to 1 g.

Analytical Characterization of Obtained Materials

Fourier-transform infrared (FTIR) spectra were registered with a Nicolet iS 50 FTIR spectrometer using attenuated total reflection (ATR) sampling module in the range of 4,000 cm^{-1} to 500 cm^{-1}. The instrument was calibrated before sampling against a clear and dry crystal surface. Thermogravimetry curves of samples were registered on the thermogravimetric TGA 5500 instrument (USA) under nitrogen atmosphere at the temperature range from 25 °C to 400 °C and a heating rate of 10 °C/minute.

Spectrofluorometric analysis were performed on the Horiba FluoroMax-4 spectrofluorometer. The instrument was calibrated over deionized water; a sampling of the fluorescent dyes was performed with deionized water solutions; a sampling of the solids SAP and silica were performed with dry materials.

The tracers' chemical stability investigations were performed via exposure of materials over one day or one week to the five laboratory conditions mimicking downhole media. Tests included the treatment of tracers with pure organic solvents such as THF, diethyl ether, and diesel, as well as exposure of tracers to aqueous brines containing:

- Brine 1: NaCl (41.041 g/L), $CaCl_2$ (2.384 g/L), $MgCl_2$ (17.645 g/L), Na_2SO_4 (6.343 g/L), and $NaHCO_3$ (0.165 g/L).
- Brine 2: NaCl (150.446 g/L), $CaCl_2$ (69.841 g/L), $MgCl_2$ (20.396 g/L), Na_2SO_4 (0.518 g/L), and $NaHCO_3$ (0.487 g/L).

Results and Discussion

Preparation of Tracing Materials

To engineer efficient fluorescent tracers, we utilized a combinatorial chemistry approach for preparation and selection of the best performing combinations of fluorophores and carrier matrices. Knowing the possibility of aggregation caused fluorescence quenching of fluorophores[15], we proposed and fabricated several variants of fluorophore matrix combinations that included covalent linkage between matrix and fluorescent moiety that could be spatially tight as well as spatial compartmentalization of the fluorescent molecules within the cross-linked polymeric nets. Additionally, we investigated the possibility of loading fluorophores into the sorbent matrices with various ratios to estimate efficient fluorophore concentrations, excluding aggregation caused quenching.

Various matrices were studied for the trial loading of/modification with fluorophores, including silica, PVA, chitosan and SAP based on sodium salt of poly(methyl acrylate). A number of fluorophores, including FITC, fluorescein, Rhodamine B, and commercial pigments were used in the current investigation for matrices customization. Upon the development of tracers, we chose two different approaches of matrix modification: covalent binding of fluorescent agents and physical absorption of fluorophores into the carrier to result in fluorescence-bearing tags. These fluorescent labeled/loaded tracers were subsequently used for chemical stability evaluations and fluorescence studies.

For the development of tracers by carriers' modification through a physical absorption, selected matrices (silica and sodium polyacrylate SAP) were soaked with an aqueous solution of fluorescent dyes (fluorescein, Rhodamine B, and commercial pigments) followed by drying the resulted impregnated sorbents at the vacuum oven. A SAP was used as a matrix for tracers loaded with xanthene dyes — fluorescein and Rhodamine B. Similarly, a SiO_2 matrix was impregnated with fluorescein and fluorescent pigment.

To evaluate the efficiency of chemical modification of matrices, we choose readily available commercial polymers as chitosan and PVA for treatment with FITC. FITC chitosan adduct produced with 50:1 molar ratio of the fluorophore-to-matrix loading, Fig. 1, exhibited a low intensity of fluorescent emission in the powder form and high fluorescent emission in an aqueous solution, presumably due to the aggregation caused fluorescent quenching[16] at the solid-state.

To overcome this drawback and get an emissive tracer, tags based on chitosan loaded with 10 wt% of fluorescent pigment and cross-linked with glutaraldehyde were

Fig. 1 *The synthesis of the chitosan labeled with FITC.*

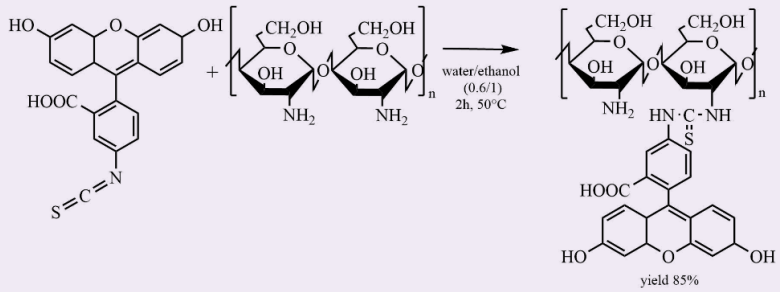

synthesized, Fig. 2. Obtained cross-linked chitosan network-bearing pigment demonstrated high fluorescent intensity visible to the naked eye, both in the powder form and in aqueous suspensions.

PVA was modified with FITC at molar ratio ~5:1 according to the published procedure[15], Fig. 3. Contrary to the FITC chitosan derivative, the FITC-PVA adduct exhibited high fluorescent intensity upon exposure to UV light in a dry state and in aqueous dispersions. Unfortunately, this labeled polymer has low resistance to high temperature and brines.

ATR-FTIR Characterization of Tracing Materials

All engineered tracing materials were characterized using ATR-FTIR spectroscopy to elucidate the molecular structure of products modified via fluorophores loading or covalent attachment.

ATR-FTIR Investigations of Chitosan-Based Tracers: The FTIR spectra of chitosan-based tracers are represented in Fig. 4. The FTIR spectrum of starting chitosan shows a broad absorption band at 3,451 cm^{-1}, attributed to O-H stretching vibrations, which overlaps the N-H stretching at the same region. Bands at 2,931 cm^{-1} to 2,925 cm^{-1} represents C-H stretching vibrations of aliphatic CH bonds of polysaccharide cycles and methylene groups. The band at 1,635 cm^{-1} is representing the N-H bending vibration. The bands at 1,167 cm^{-1} and 1,045 cm^{-1} are attributed to C-O-C stretching vibrations of glycoside link and the chitosan ring.

Similarly, the FTIR spectrum of the hydrogel based on chitosan cross-linked with glutaraldehyde exhibit broad absorption bands at 3,417 cm^{-1} representing overlapping O-H and N-H stretching vibrations; bands at 2,930 cm^{-1} to 2,925 cm^{-1} attributed to the C-H vibrations of CH- and methylene groups. Absorption bands at 1,167 cm^{-1} and 1,028 cm^{-1} are attributed to the C-O-C bond vibrations of the glycoside link and the chitosan ring. Contrary to the starting material, the N-H bending vibration band of the amine group at ~1,630 cm^{-1} diminished intensity, and an additional band attributed to C=N vibrations of the imine group[17] appeared at 1,652 cm^{-1}, confirming the formation of the cross-linked structure upon reaction of the chitosan amino group with glutaraldehyde.

Elucidating the structure of the FITC chitosan adduct, we noted characteristic bands at 3,417 cm^{-1} attributed to O-H and N-H stretching vibrations and absorption bands at 2,930 cm^{-1} to 2,925 cm^{-1} attributed to the C-H vibrations. Moreover, additional absorption peaks appeared at 1,594 cm^{-1}, 1,535 cm^{-1}, and 1,458 cm^{-1} that are representative for stretching vibrations of C=C bonds in aromatic rings of FITC moiety.

Noticeably, the additional N-H bending vibration band appeared at 1,640 cm^{-1} compared to and in addition to the amine group bending vibration of pure chitosan at 1,630 cm^{-1}, confirming partial modification

Fig. 2 *The synthesis of chitosan loaded with fluorescent pigment cross-linked with glutaraldehyde.*

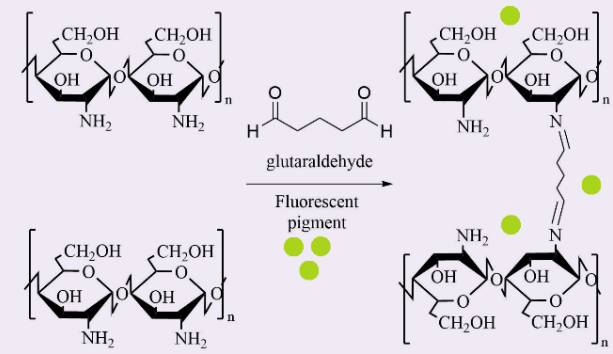

Fig. 3 *The synthesis of the FITC-PVA adduct.*

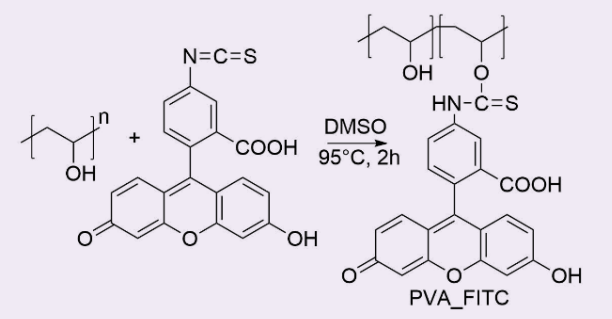

Fig. 4 *The ATR-FTIR spectra of chitosan (Chitosan); chitosan cross-linked with glutaraldehyde (Chitosan_Gly); and chitosan FITC adduct (Chitosan_FITC).*

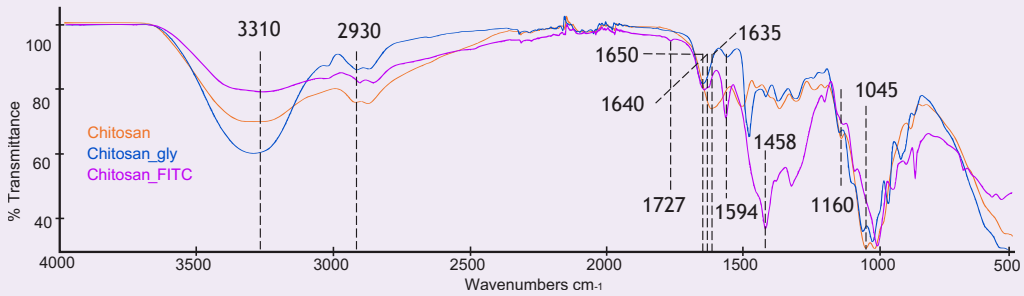

of the NH_2 residue. A small band of lactone carbonyl group appeared at 1,727 cm^{-1} assigned to lactone, forming FITC moiety. A strong band at 1,050 cm^{-1} can be attributed to the C=S group vibrations formed upon covalent attachment of the FITC group to chitosan amino function.

ATR-FTIR Spectroscopy of PVA-Based Tracers: To confirm chemical modification of PVA with FITC, we registered FTIR spectra of the starting polymer, fluorescent dye, and the resulted FITC-PVA product, Fig. 5. The ATR-FTIR spectrum of pure FITC demonstrates a strong absorbance peak at 2,015 cm^{-1}, characteristic for the isothiocyanate functional group. Absorption peaks at 1,594 cm^{-1}, 1,535 cm^{-1}, and 1,458 cm^{-1} are representative for stretching vibrations of C=C bonds of aromatic cycles.

A comparison of the spectra of PVA-FITC adduct and pure FITC shows an absence of absorption at 2,015 cm^{-1} and indicates that isothiocyanate was fully converted upon modification of PVA. The spectra B and C, Fig. 5, show strong broad absorbance bands at 3,288 cm^{-1} for pure PVA and 3,318 cm^{-1} for FITC labeled derivates. These bands are assigned to O-H stretching vibration of the hydroxyl group of PVA. This band possess reduced intensity in the FITC adduct of PVA, confirming that the hydroxyl group was involved in the additional reaction with isothiocyanate.

Bands corresponding to the C-H asymmetric stretching vibration of the CH_2 group occurs at 2,938 cm^{-1} and 2,941 cm^{-1}, both for the starting polymer and for the FITC modified PVA. The sharp band, 1,087 cm^{-1}, corresponds to the C-O stretching of secondary alcohol groups present on the PVA and FITC-PVA derivative; an additional absorbance band appeared in the spectrum of the FITC modified PVA at 1,013 cm^{-1} assigned to the newly formed C=S bond of the FITC adduct.

ATR-FTIR Characterization of Sodium Polyacrylate-Based Tracers: Figure 6 represents the FTIR spectra of tracers based on sodium polyacrylate before and after loading fluorescent dyes. The spectrum of pristine SAP exhibits a strong broad absorption area of approximately 3,400 cm^{-1} to 3,100 cm^{-1} corresponding to the stretching vibration of the hydroxyl groups from adsorbed water. Shoulder bands around 2,800 cm^{-1} attributed to C-H asymmetric stretching vibration of polymeric chained CH- and CH_2 groups. A characteristic absorption band at 1,650 cm^{-1} attributed to deformation vibrations of the C-OH group. Bands at 1,530 cm^{-1} and 1,310 cm^{-1} are typical for salts of carboxylic acids[18] and are attributed to symmetrical

Fig. 5 *The ATR-FTIR spectra of fluorescein isothiocyanate (A, FITC pure); PVA (B, PVA-pure); and FITC-PVA adduct (C, PVA-FITC).*

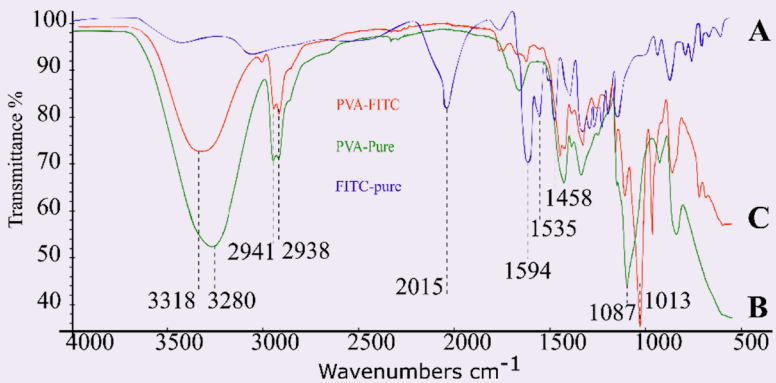

Fig. 6 *The ATR-FTIR spectra of pristine sodium polyacrylate (SAP pure); sodium polyacrylate loaded with fluorescein (SAP fluorescein); sodium polyacrylate loaded with Rhodamine B (SAP rhodamine).*

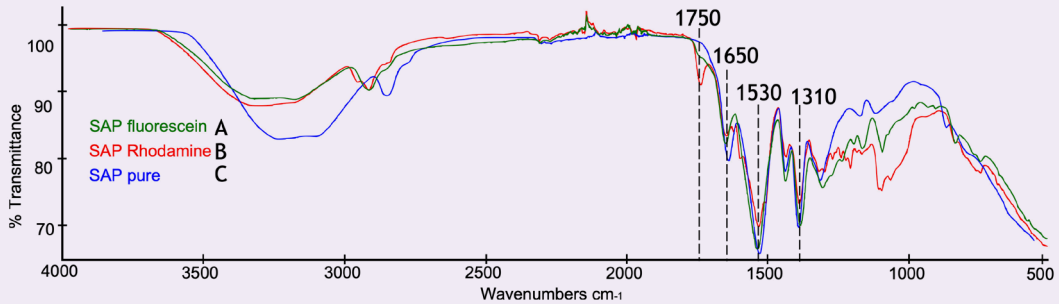

stretching vibrations of carboxyl anions $-COO^-$. Upon impregnation of SAP sorbent with xanthene dyes, the novel bands appear at 1,750 cm^{-1}, which is assigned to the -C=O vibrations of the carbonyl fragment of the lactone form of fluorescein and Rhodamine B.

Presumably, adsorption of dyes as fluorescein and Rhodamine B into the SAP matrix is associated with electrostatic acid-base interactions between the guest dye molecule and polar functional groups of the carrier matrix. At steady-state, the equilibrium between acid and base forms of dye will be reached and both spirolactone and opened dye structures will be presented in the matrix. The tautomeric forms of lactone Rhodamine B base and opened Rhodamine B acid are represented in Fig. 7.

ATR-FTIR Spectra of Silica-Based Tracers: We examined loading of the silica-based matrix with xanthene dyes and presented FTIR spectra of the pure and fluorescein loaded SiO_2 in the range of 4,000 cm^{-1} to 500 cm^{-1} in Fig. 8. Both spectra exhibited characteristic peaks for silica at 800 cm^{-1}, 980 cm^{-1}, and 1,085 cm^{-1} owing to Si-O-Si symmetric stretching, Si-OH stretching, and Si-O-Si asymmetric stretching vibrations, respectively[19]. Due to low molar ratio of SiO_2 to fluorescein there were almost no detectable differences in the spectra of initial and dye loaded samples.

Other than that, the porosity and nontransparent structure of the matrix can impede detection of dye inside SiO_2-based tracers by ATR-FTIR. The successful loading of silica with fluorescein was confirmed via UV-Vis fluorescence spectroscopy.

Chemical Stability Examination of Tracers

With the application of engineered tracers for downhole operations, we screened obtained materials for

Fig. 7 *The Tautomeric forms of lactone Rhodamine B base and opened Rhodamine B acid.*

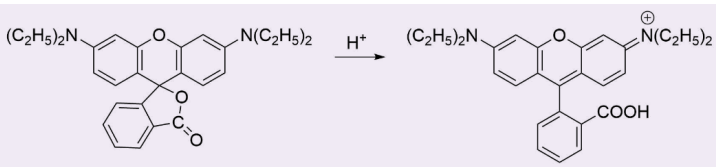

Fig. 8 *The ATR-FTIR spectra of pure silica (SiO_2 pure) and silica loaded with fluorescein (SiO_2 fluorescein).*

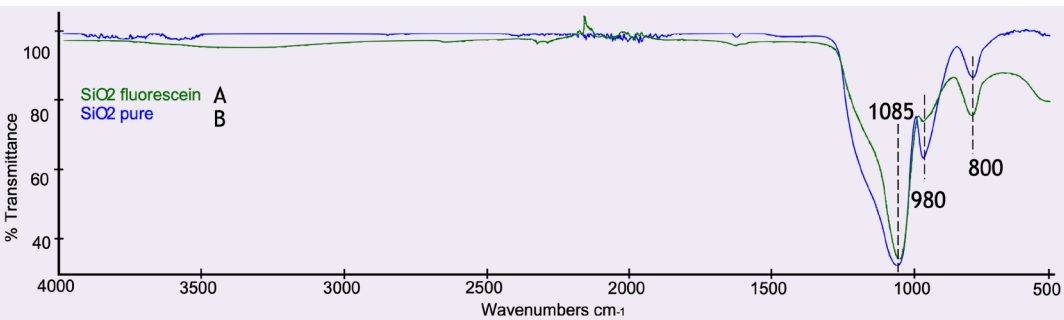

Table 1 *The examination of the chemical stability of the selected tracers.*

	Time	90 °C	90 °C	THF	Ether	Diesel
		Brine 1	Brine 2			
Fluorescent dye SiO_2	One day	Stable	Stable	Stable	Stable	Stable
	One week	Stable	Stable	Stable	Stable	Stable
Fluorescein SiO_2	One day	Stable	Stable	Stable	Stable	Stable
	One week	Stable	Stable	Reduce	Stable	Reduce
SAP loaded with Fluorescein	One day	Stable	Stable	Stable	Stable	Stable
	One week	Stable	Stable	Stable	Stable	Stable
SAP loaded with Rhodamine B	One day	Stable	Stable	Stable	Stable	Stable
	One week	Stable	Stable	Stable	Stable	Stable

Fig. 9 *The TGA curves: (a) SiO_2 pure, SiO_2 fluorescein, and SiO_2 fluorescent pigment; and (b) SAP fluorescein, and SAP Rhodamine B.*

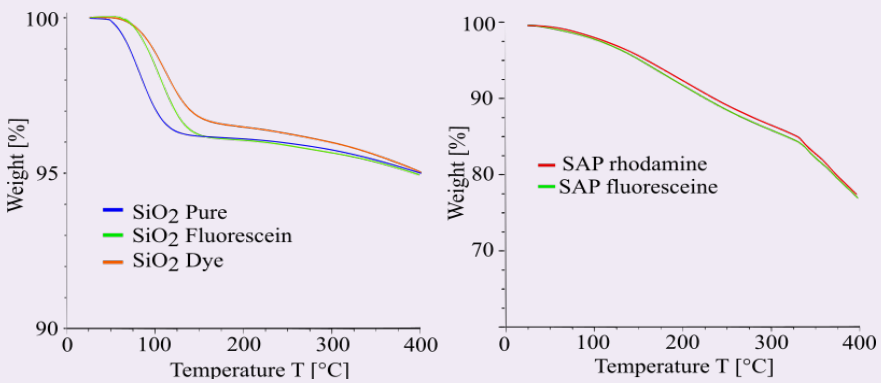

their chemical stability to sour media and treatment with formation fluids. For this goal, tracer samples were exposed to acidic aqueous solutions with a pH ~1. Chitosan-based materials exhibit fast degradation upon acid treatment and were detached from further tests as chemically unstable tracer carriers.

The remaining materials were further tested for stability to the conditions mimicking downhole media. Therefore, samples of fluorescent loaded tags were incubated at 90 °C with aqueous brines containing formation salts NaCl, $CaCl_2$, $MgCl_2$, Na_2SO_4, and $NaHCO_3$ for a period of 1 day up to 1 week. Degradation via hydrolysis was noted for fluorescent modified PVA upon exposure to electrolyte solutions over a few hours. Fluorescein and fluorescent pigment loaded silica (Flu-SiO_2) as well as xanthene dyes-loaded SAP (Flu-SAP) exhibited no visible decomposition and demonstrated almost no leakage of dyes at the described conditions.

Consequently, these stable matrices (Flu-SiO_2, Flu-SAP) were further tested for resistance to organic solvents (THF, ether, and diesel). Among materials tested for the exposure to organic media, fluorescein and Rhodamine B loaded SAPs, and fluorescein and pigment loaded SiO_2 exhibited no visible deterioration of the fluorescent properties.

Table 1 summarizes the results of these investigations.

Table 2 *The evaluation of the thermal stability of the selected tracers.*

Type of Tracers	$T_{5\%}$ (°C)	Yield (wt%)
SAP Rhodamine B	170	78
SAP fluorescein	168	77
SiO_2 pure	400	95
SiO_2 fluorescein	400	95
SiO_2 Rhodamine B	400	95

Fig. 10 *The fluorescence spectroscopy characterization of the tracers.*

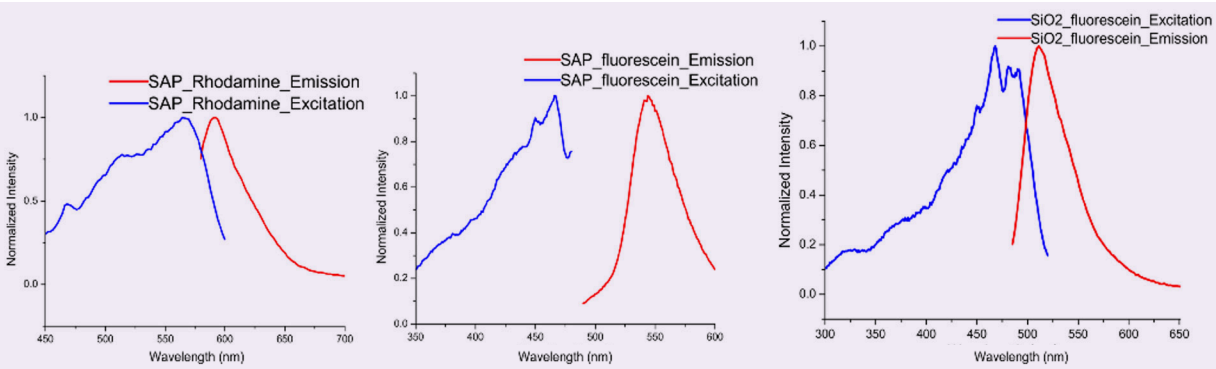

Investigation of the Thermal Stability of Tracers by TGA

To evaluate the thermal stability of the selected tracers, thermogravimetric analysis (TGA) monitoring of the sample's weight losses upon heat treatment from room temperature to 400 °C at the heating rate of 10 °C/minute in a nitrogen atmosphere was performed. As shown in Fig. 9a thermogravimetric curves of silica-based tracers as well as pure silica exhibited weight losses of about 5 wt% upon exposure to a 100 °C temperature and further kept almost the constant mass.

All curves in Fig. 9a demonstrated a similar behavior; where the highest weight losses occurred at the temperature range of 20 °C to 150 °C and corresponded to the loss of absorbed water.

Figure 9b represents the thermogravimetric curves of superabsorbent-based tracers. The total gradual weight losses of the SAP tracers at the temperature range of 20 °C to 400 °C reached up to 22% to 23%. The sharp inflection could be noted at 315 °C that is attributed to the degradation of the dyes.

Table 2 summarizes the thermogravimetric total weight losses of selected tracers and indicates limits of the thermal stability of the chosen specimens. Therefore, tracers based on SAPs loaded with xanthene dyes are relatively stable up to 170 °C with no deterioration of fluorescent properties. Silica-based tracers are even more robust to the high temperature exposure.

Fluorescence Spectroscopy Characterization of Selected Stable Tracers

The fluorescent behavior of fluorescein and Rhodamine B loaded tracers was explored using UV visible fluorescence spectroscopy. Excitation and emission wavelengths were recorded for SAP Rhodamine B, SAP fluorescein and silica fluorescein loaded tracers and compared with published data since photochemical properties of xanthene dyes are sensitive to the measurements medium[20]. Tracers based on SAP Rhodamine B demonstrated standard maxima of excitation and emission wavelengths (λ_{Ex} 560 nm and λ_{Em} 590 nm) characteristic for Rhodamine B (λ_{Ex} 554 nm and λ_{Em} 578 nm)[20], without much deviation due to the interactions of dye with the matrix.

Fig. 11 *Samples of the drill cuttings collected and mixed with tracers. (1A) SAP fluorescein tags in daylight; (1B) SAP fluorescein tags in UV light; (1C) SAP fluorescein tags in daylight; and (1D) SAP fluorescein tags in UV light. (2A) SAP Rhodamine B tags in daylight; (2B) SAP Rhodamine B tags in UV light; (2C) SAP Rhodamine B tags in daylight; and (2D) SAP Rhodamine B tags in UV light. (3A) Silica fluorescein tags in daylight; (3B) Silica fluorescein tags in UV light; (3C) Silica fluorescein tags in daylight; and (3D) Silica fluorescein tags in UV light.*

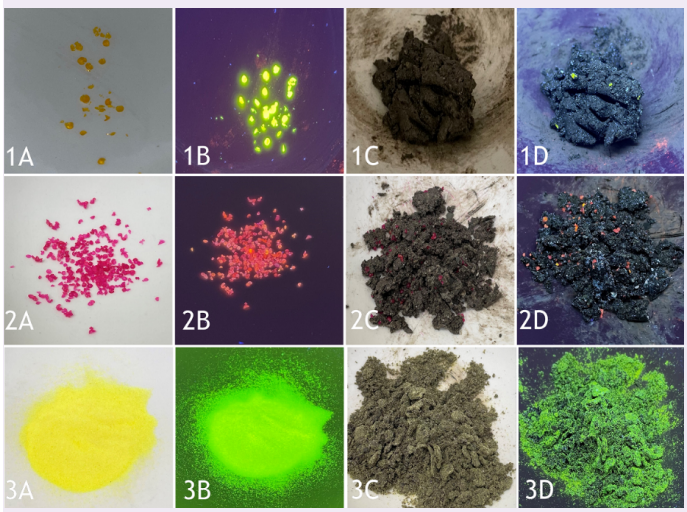

Similarly, tracers based on silica loaded with fluorescein demonstrated reported excitation and emission wavelengths (few peaks at λ_{Ex} 470 nm to 491 nm and λ_{Em} 515 nm) corresponding to literature reported[21] (λ_{Ex} 488 nm and λ_{Em} 515 nm). Deviation from the standard values was detected only for SAP loaded with fluorescein (λ_{Ex} 462 nm and λ_{Em} 545 nm) presumably, due to basic pH of sodium polyacrylate matrix.

Figure 10 summarizes the emission and excitation spectra for SAP and SiO_2 matrices loaded with fluorescent agents.

Applications of Tracers in the Drill Cuttings Tagging

Selected fluorescent tracers, stable to downhole

conditions, namely SAP fluorescein, SAP Rhodamine B, and silica fluorescein loaded tags, were tested for their ability to label drill cuttings in the laboratory conditions with further camera detection. For this goal, samples of the drilling cuttings collected from the oil fields were mixed with the selected tracer and pictures of the tagged cuts under daylight and UV light were recorded via camera, Fig. 11.

The library of photos of the tagged drill cuttings is further used for development of an image recognition system. It is noted that tracers based on the silica fluorescein were barely detectable as a separate particle with a camera, both in daylight and UV light, due to their small size of 60 µm to 200 µm, however, the SAP dyes loaded tags of 0.5 mm to 1 mm in size were well detectable with a camera under UV light upon drill cuttings labeling.

These obtained SAP-based tracers were clearly visible after mixing with drill cuttings samples, especially under the UV light. This type of tag is primarily selected for drill cuttings colored tagging according to the depth at the mud cuttings circulation prototype equipped with a shale shaker and UV camera. Recorded photographs and video of the tagged formation cuts are planned for further engineering of camera detection and an AI-based image recognition system, and its consequent field trials that are currently ongoing with our group.

Conclusions

In the present study, we demonstrated the design and preparation of a variety of cost-effective and readily available fluorescent tags composed of carrier matrices loaded with and covalently modified by fluorophores. This novel engineered library of tracers was screened at various harsh medias to select stable fluorescent particles resistant to the conditions mimicking a downhole environment. The most stable of the obtained materials exhibited high chemical stability and thermal robustness up to and over a temperature of 170 °C. Based on this data, it is proven that prepared tracers can be used in downhole applications. Prepared fluorescent loaded tags are planned for downhole tests on drill cuttings labeling accompanied by tagged cuttings detection and drilling depth assignment via a wellhead camera on a shale shaker.

Therefore, we innovated a fast and efficient concept of downhole fluorescent drill cuttings tracing developed for on-site near real-time detection with a UV camera and image recognition system. Fast and simple drill cuttings depth determination would improve the accuracy of a drilling depth correlation and advance petrophysical characterization of the formation to allow for optimal well placement.

References

1. Ciszkowski, C., Ouled Ameur, Z., Forsyth, J.P.J., Nightingale, M., et al.: "Application of Geochemical and Isotopic Tracers for Characterization of SAGD Waters in the Alberta Oil-Sand Region," *SPE Production & Operations*, Vol. 35, Issue 1, February 2020, pp. 188-201.
2. Hemed, T.S.: "Development of a Tracer Analysis System Using Dye Tracers," SPE paper 204275, presented at the SPE Annual Technical Conference and Exhibition, virtual, October 26-29, 2020.
3. Green, L., Entzminger, D., Tovar, D., Alimahomed, A., et al.: "Tying Horizontal Measurements to Well Performance Using Production Logs and Chemical Tracers in Multiple Wolfcamp Shale Wells, Delaware Basin," SPE paper 194318, presented at the SPE Hydraulic Fracturing Technology Conference and Exhibition, The Woodlands, Texas, February 5-7, 2019.
4. Li, J., Jiang, H. and Liu, Y.: "Investigation of Pore-Scale Dispersion in Polymer Flooding," IPTC paper 14119, presented at the International Petroleum Technology Conference, Bangkok, Thailand, November 15-17, 2011.
5. Hall, C. and Hughes, T.L.: "Ion Chromatography Tracer Experiments during Drilling," SPE paper 25178, presented at the SPE International Symposium on Oil Field Chemistry, New Orleans, Louisiana, March 2-5, 1993.
6. Antoniv, M., Sherry Zhu, S., Chang, S., Poitzsch, M.E., et al.: "Method for Detecting Nanoparticles on Cuttings Recovered from a Gas Reservoir," *Energy and Fuels*, Vol. 35, Issue 9, April 2021, pp. 7708-7716.
7. Khan, M.N., Iwama, H., Al-Neaimi, A., Al-Shehhi, O., et al.: "A to Z of Gas Tracers — A Decade of Learning and Experience," SPE paper 183413, presented at the Abu Dhabi International Petroleum Exhibition and Conference, Abu Dhabi, UAE, November 7-10, 2016.
8. Serres-Piole, C., Preud'homme, H., Moradi-Tehrani, N., Allanic, C., et al.: "Water Tracers in Oil Field Applications: Guidelines," *Journal of Petroleum Science and Engineering*, Vols. 98-99, November 2012, pp. 22-39.
9. Anisimov, L.A., Kilyakov, V.N. and Vorontsova, I.V.: "The Use of Tracers for Reservoir Characterization," SPE paper 118862, presented at the SPE Middle East Oil and Gas Show and Conference, Manama, Kingdom of Bahrain, March 15-18, 2009.
10. Tomich, J.F., Dalton Jr., R.L., Deans, H.A. and Shallenberger, L.K.: "Single-Well Tracer Method to Measure Residual Oil Saturation," *Journal of Petroleum Technology*, Vol. 25, Issue 2, February 1973, pp. 211-218.
11. Khaledialidusti, R., Kleppe, J. and Enayatpour, S.: "Evaluation and Comparison of Available Tracer Methods for Determining Residual Oil Saturation and Developing an Innovative Single Well Tracer Technique: Dual Salinity Tracer," IPTC paper 17990, presented at the International Petroleum Technology Conference, Kuala Lumpur, Malaysia, December 10-12, 2014.
12. Al-Murayri, M.T., Al-Qenae, A., AlRukaibi, D., Chatterjee, M., et al.: "Design of a Partitioning Interwell Tracer Test for a Chemical EOR Pilot Targeting the Sabriyah Mauddud Carbonate Reservoir in Kuwait," SPE paper 187549, presented at the SPE Kuwait Oil and Gas Show and Conference, Kuwait City, Kuwait, October 15-18, 2017.
13. McCartney, R.A. and de L.G. Solbe, M.J.: "Use of Tracers in Drilling Muds to Allow the Estimation of In Situ Formation Water Compositions from Drilling Mud Contaminated Formation Water Samples," SPE paper 50721, presented at the SPE International Symposium on Oil Field Chemistry, Houston, Texas, February 16-19, 1999.
14. Kaneo, Y., Hashihama, S., Kakinoki, A., Tanaka, T., et al.: "Pharmacokinetics and Biodisposition of Poly(Vinyl

Alcohol) in Rats and Mice," *Drug Metabolism and Pharmacokinetics*, Vol. 20, Issue 6, 2005, pp. 435-442.

15. Tang, Y. and Tang, B.Z.: *Handbook of Aggregation-Induced Emission, Volume I: Tutorial Lectures and Mechanism Studies*, John Wiley & Sons Inc.: New Jersey, 2022, 640 p.
16. Chen, S., Wang, H., Hong, Y. and Tang, B.Z.: "Fabrication of Fluorescent Nanoparticles Based on AIE Luminogens (AIE Dots) and their Applications in Bioimaging," *Materials Horizons*, Vol. 3, Issue 4, April 2016, pp. 283-293.
17. Triana-Guzmán, V.L., Ruiz-Cruz, Y., Romero-Peñaloza, E.L., Zuluaga-Corrales, H.F., et al.: "New Chitosan-Imine Derivatives: From Green Chemistry to Removal of Heavy Metals from Water," *Revista Facultad de Ingeniería Universidad de Antioquia*, Vol. 89, 2018, pp. 34-43.
18. Grabowska, B. and Holtzer, M.: "Structural Examination of the Cross-Linking Reaction Mechanism of Polyacrylate Binding Agents," *Archives of Metallurgy and Materials*, Vol. 54, Issue 2, January 2009, pp. 427-437.
19. Yadav, A.K. and Singh, P.: "A Review of the Structures of Oxide Glasses by Raman Spectroscopy," *RSC Advances*, Vol. 5, Issue 83, July 2015, pp. 67583-67609.
20. Kathiravan, A., Anbazhagan, V., Jhonsi, M.A. and Renganathan, R.: "Fluorescence Quenching of Xanthene Dyes by TiO_2," *Zeitschrift fur Physikalische Chemie*, Vol. 221, Issue 7, June 2007, pp. 941-948.
21. Sjöback, R., Nygren, J. and Kubista, M.: "Absorption and Fluorescence Properties of Fluorescein," *Spectrochimica Acta Part A: Molecular and Biomolecular Spectroscopy*, Vol. 51, Issue 6, June 1995, pp. L7-L21.

About the Authors

Vladimir Khmelnitskiy

M.S. in Chemical Technology, D. Mendeleev University of Chemical Technology of Russia

Vladimir Khmelnitskiy is a Petroleum Scientist working with the Advanced Materials Team at Aramco Innovations, in the Aramco Global Research Center in Moscow. Before joining Aramco Innovations in 2021, he worked for the All-Russian Scientific Research Institute of Aviation Materials as an Engineer for polymer composite for four years.

Vladimir's research area includes polymer chemistry, polymer resins, and reinforced polymer materials, and their novel applications. His present research interests include synthesis, scale up, and physical and chemical characterization of new functional materials for fluorescent tracer technology.

In 2017, Vladimir received his B.S. degree and in 2019, he received his M.S. degree, both in Chemical Technology from the D. Mendeleev University of Chemical Technology, Moscow, Russia.

Dr. Nouf M. AlJabri

Ph.D. in Chemical Engineering, King Abdullah University of Science and Technology

Dr. Nouf M. AlJabri is a Geophysicist and Team Leader of the Advanced Material Domain in Saudi Aramco's Exploration and Petroleum Engineering Center – Advanced Research Center's (EXPEC ARC) King Abdullah University of Science and Technology (KAUST) Upstream Research Center (KURC).

Nouf and her team are spearheading multiple disruptive technologies to foster sustainability using advanced material on several fronts, including hydrogen, carbon dioxide capture and utilization, functionalized material, and bio-inspired material.

Previously, she worked as a visiting scientist with Professor Timothy M. Swager at MIT to design and synthesize novel advanced materials to resolve key upstream challenges.

Nouf has several published articles in high-impact journals, and a number of patents. She has delivered numerous plenary and invited talks and lectures worldwide. Because of her contribution to the energy sector, Nouf is a recipient of several international prestigious awards and governmental recognitions.

She received her M.S. degree and Ph.D. degree in Chemical Engineering from KAUST, Thuwal, Saudi Arabia.

Dr. Vera Solovyeva

Ph.D. in Chemistry, Lomonosov Moscow State University

Dr. Vera Solovyeva is a Science Specialist working with the Advanced Materials Team at Aramco Innovations, in the Aramco Global Research Center in Moscow. Prior to this, she spent several years in Saudi Arabia (2011-2018) working as a post-doctoral student at the King Abdullah University of Science and Technology (KAUST) Catalysis Center and in materials engineering at the Advanced Membranes and Porous Materials Center and Economic Development Department of KAUST.

Previously, Vera was working as Senior Research Scientist in drug design and customized pharmaceutical synthesis for Ely Lilly, Novartis, and other Big Pharma customers at the Russian subsidiary of global biotech company ChemDiv Inc.

Her previous research interests involved pharmaceutical chemistry, catalysis, metal-organic, and covalent organic frameworks engineering, and their novel applications. Over the last few years, the focus of her interests has changed to petroleum chemistry, oil and gas exploration, and corrosion mitigation research.

Vera received her Ph.D. degree in Chemistry from Lomonosov Moscow State University, Moscow, Russia.

A Deep Learning Optimization Framework for Geothermal Energy Production Based on Carbon Dioxide

Dr. Klemens Katterbauer, Dr. Abdulaziz S. Qasim, Dr. Abdallah A. Al Shehri and Dr. Abdulkareem M. Al Sofi

Abstract /

Carbon dioxide (CO_2) plume geothermal (CPG) technology has been developed in recent years by several companies. The technology strives to utilize CO_2 stored in saline aquifers to produce geothermal energy. CPG is different from conventional geothermal concepts. Here, the feedstock utilizes CO_2 as a carrier fluid through which heat is extracted from the subsurface reservoir. The system does not necessarily rely on shallow natural hydrothermal locations but can utilize a conventional sedimentary basis. At last, CPG can still harvest energy in low temperature environments that are currently not suitable for conventional geothermal extraction.

We present a new deep learning optimization framework for the maximization of power generation from a CPG system. The framework utilizes an adapted neural basis expansion analysis for an interpretable time series (N-BEATS) approach. The approach is based on a stack of ensembled feedforward networks that are also stacked by interconnecting backcast and forecast links. The advantages of the framework are its flexibility with respect to different input parameters and various forecastable time series. This is particularly important for CPG to easily capture variations in the temporal dynamics and temperature responses across the various CO_2 injection and production wells.

We evaluated the framework on a simulated CO_2 storage reservoir based in the Taranaki Basin in New Zealand. The Taranaki Basin has been well studied for CO_2 storage, given the presence of a large saline aquifer that may be well suitable for both CO_2 storage and CPG energy production. We simulated 3.5 years of CO_2 injection and production for geothermal energy production as input to the N-BEATS framework. The training performance of the network was strong, and the model's performance was then evaluated on a subsequent two years of energy production. The deep learning framework is then integrated into a global optimization framework to optimize energy production while adapting CO_2 injection.

The new deep learning N-BEATS optimization framework for CPG power generation represents an innovative way to enhance energy generation from CO_2 storage reservoirs providing a sustainable way to minimize the carbon footprint while delivering energy.

Introduction

Carbon capture and storage (CCS) has attracted strong interest from the oil and gas industry and the scientific community alike, due to the ability to store carbon dioxide (CO_2) in subsurface reservoirs[1]. Deep saline aquifers may be well suited for safe and long-term storage given their geological structure. The long-term underground storage in saline aquifers depends on a variety of interrelated trapping mechanisms in addition to the caprock sealing efficiency. Well integrity plays another critical role in reducing uncertainty[2]. When evaluating CO_2 storage sites, both natural and artificially induced hydraulic fractures are important factors to be considered for the risk assessment of CO_2 storage[3].

Fractures are commonplace in many geological settings and represent a crucial role in hydrocarbon migrations and entrapment. Fractures impact fluid flow in a variety of forms, particularly due to the complexity and varying natures of the fractures, which channel the injected CO_2 throughout the reservoir formation. This is especially important for tight gas reservoirs and low permeable cap rock structures whose permeability is primarily characterized by fault and fractures. For these fractures, the spatial distribution of the faults and fractures, the orientation, conductivity, and the overall contribution to the effective permeability are essential to know. Fractures interfacing with the wellbore are critical to determine, given that they are the main channel for the CO_2 to flow into the reservoir[4].

The CO_2 plume geothermal (CPG) approach utilizes a sedimentary basis that is naturally permeable, which allows the CO_2 to move from the injector well to the producer well. The entire CO_2 plume process technology is demonstrated in Fig. 1[5]. The CO_2 is injected in supercritical form into the reservoir, which heats the

Fig. 1 *An illustrative process description of the CO_2 plume technology[5] (Source: Think Geoenergy).*

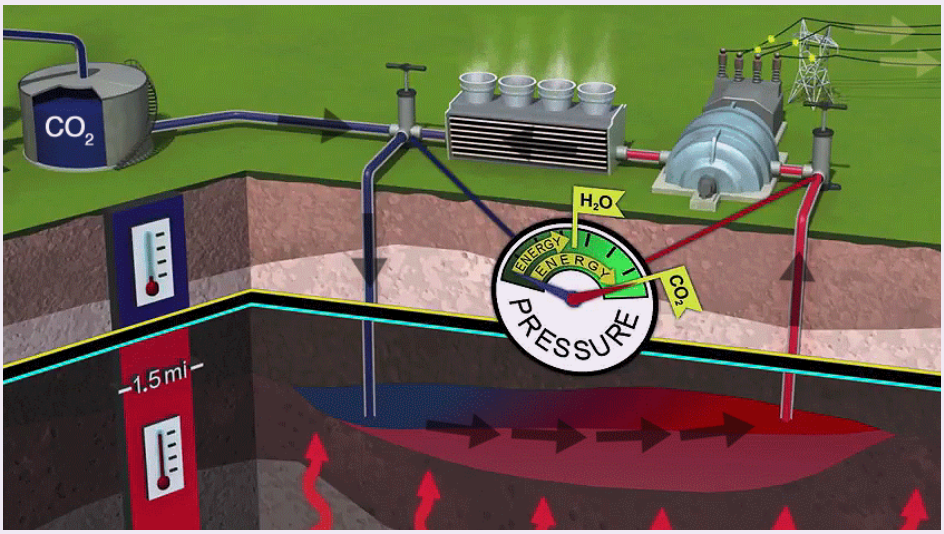

liquid up. The supercritical CO_2 is then retrieved on the surface for power generation and subsequently re-injected or stored.

The system consists of either single or multiple CO_2 injection and production wells and a permeable sedimentary reservoir that has a low permeability caprock. The reservoir temperature has to be sufficient, and the technology requires a surface power plant that converts the heat and pressure energy to transform the generated heat into electrical power. The system may also be utilized only to generate heat to exchange the heat for another working fluid[6]. In a direct system, no secondary fluid is needed as the supercritical CO_2 is heated in the reservoir and produced on the surface via a production well.

The expansion in the turbine drives the turbine to produce electricity. The expanded CO_2 is then condensed again into a liquid, compressed, and re-injected into the reservoir. Depending on the energy requirements of the compression, the CO_2 can be stored in a shallow reservoir to optimize power production and utilize the CO_2 on an as needed basis[7]. Specifically, when there is a significant demand for power generation, the CO_2 from the shallow reservoir is retrieved to be compressed and injected into the reservoir, while during off-peak hours, more CO_2 is injected into the shallow reservoir, which may be utilized at a later stage.

To achieve efficient power generation, the compression and cooling of the CO_2 has to be as efficient as possible. There are uncertainties about how efficient the CO_2 transfers are within the reservoir, and the expected CO_2 production levels based on various injection strategies. Therefore, a firm understanding of the optimal injection and production quantities of CO_2 is essential to achieve a net electrical energy surplus[8].

Therefore, real-time optimization of the injection and production of CO_2 for geothermal energy production is essential to support electricity demands and maximize the performance of the CPG system. Being able to accurately and efficiently forecast possible electricity production levels is essential to meet this objective. Given the complexity of the CO_2 fluid movement, a joint artificial intelligence global optimization approach seemed to be best feasible.

Methodology

The neural basis expansion analysis for interpretable time series (N-BEATS) framework is based on a number of principles. These principles state that the base architecture shall be simple and generic, but sufficiently deep to deliver high quality estimates. Second, the architecture should be robust with respect to time series specific feature engineering and input scaling, which allows investigating a pure deep learning architecture for time series forecasting. Finally, interpretability represents a key objective of the framework to enable the interpretation to be as easily accessible as possible[9].

The basic building block of the adapted N-BEATS architecture is a fork architecture approach that utilizes a block outline. The n-th block incorporates the input parameters and has two output vectors, z and y. The input vector, x, is the overall model input, which also incorporates a history lookback window of a pre-specified length. This lookback window includes the last measured observations and is typically a multiple of the forecast horizon, H. A preferred lookback range is from 2H to 7H. For the rest of the blocks, the inputs are the residual outputs of the previous blocks. Each block has two outputs, which contain the block's forward forecast, y of length H, and the block's best estimate z of x, which is also known as the backcast. Given the functional space's constraints, the block uses approximate signals[10].

Internally, the basic building blocks have two parts. The first is the fully connected network that has the forward, *pf*, and backward, *pb*, predictors of the expansion coefficients. The second is the backward, *gb*, and forward, *gf*, basic layers that incorporate the *pf* and *pb* expansion coefficients. These project them internally on the set of basic functions and also produce the backcast, $\underline{z}$, and the *y*. For the forecasting, a fully connected layer with RELU nonlinearity is deployed, and the task of the architecture is to predict the *pf* to optimize the accuracy of the partial forecast via mixing the basis vectors supplied by *gf*. The sub-network predicts the *pb* used by *gb* to achieve an estimate of *x*. The ultimate objective is to help downstream blocks to remove components within the input, which may not benefit the forecasting[9].

A major benefit is the deployment of doubly residual stacking that introduces extra connections from the output of each stack to the input of all other stacks that succeed it. The approach has clear advantages in helping the ability to train the deep architectures. The disadvantages are that they are challenging to interpret. The new architecture has two residual branches, with one running over the backcast prediction of each layer and the other one running over the forecast branch of every layer.

The basic building block of the multilayer fully connected network incorporating RELU nonlinearities includes blocks that are organized according to stacks using the doubly residual stacking principle, where the stacks have layers shared both with *gb* and *gf*. The forecasts are aggregated in a hierarchical fashion. This enables the easier interpretation of the deep neural network.

Results

The Pohokura gas field is located northeast of New Plymouth in the Taranaki Basin, which is close to the Methanex Motunui site in Waitara, New Zealand, Fig. 2. The Taranaki Basin covers more than 100,000 km^2, primarily beneath the shelf and the continental slope offshore or in the central-western area of the North Island of New Zealand. The land sections are beneath the Taranaki Peninsula and in the northwest area of the South Island[11].

The basin incorporates a late Cretaceous to Quaternary sedimentary fill-up that may be up to 8 km thick. The basin comprises an undeformed block and a heavily deformed area. The heavily deformed area contains the Taranaki Fault that leads to a Miocene basement over thrusting into the basin. The sedimentary fill of the Taranaki Basin may have arisen due

Fig. 2 *A map of the central and southern Taranaki Basin, with the Maui and Pohokura fields indicated in orange.*

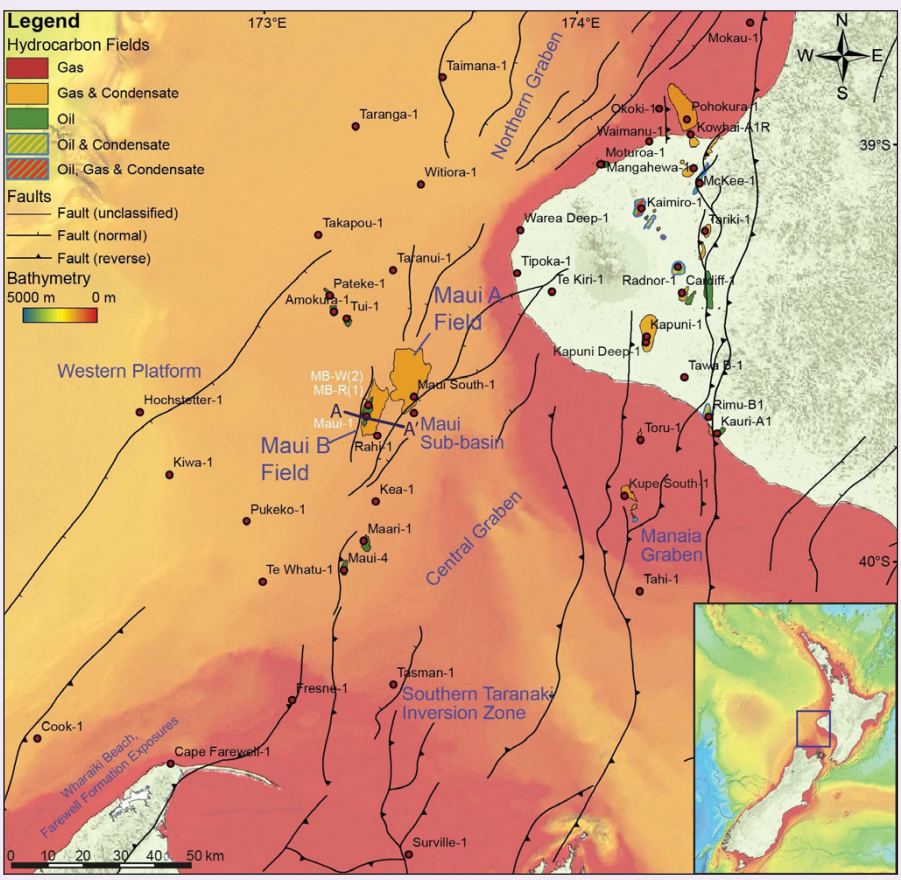

to an intracontinental manifestation of a transform fault offsetting or a failed rift[11]. There were several tectonic episodes that influenced the generation of the Taranaki Basin, which included the rifting between the Cretaceous-Eocene period, the compression within the Eocene period, and an extension that arose from the late Miocene.

The Pohokura field is the largest gas condensate field and is a low relief N-S trending anticline in the Northern Graben. The boundaries of the field are supported by the Taranaki Fault Zone in the east and the Cape Egmont Fault Zone in the west. The reservoir underwent compressional and extensional stress regimes, and most of the drilling was in the northern part of the Pohokura Field[12]. The petroleum play is a transgressive marginal marine sand within an inverted anticline. The coal seams of the Rakopi formation are the main sources for the hydrocarbons in the Pohokura field. The Rakopi Formation represents the deepest stratigraphic unit within the Taranaki Basin, and represents the major source for oil and gas fields within the basin.

The Rakopi Formation is heavily dominated by fluvial-to-marginal marine lithofacies. The Mangahewa Formation from the Eocene Epoch is the primary reservoir zone, being the most prolific and thickest. The Mangahewa Formation contains interbedded sandstone, siltstone, mudstone, and coal. The Turi Formation represented a top seal for the Pohokura Field and arose from Paleocene to the Eocene. The top seal is composed of non-calcareous, dark-colored, micaceous, and carbonaceous marine mudstone that is distributed throughout the Taranaki Basin.

The water depth is approximately 35 m in block PMP 38154. The Taranaki Basin has several reservoirs that range from the Paleocene to Pliocene, and is a gas condensate field in a low relief anticline, that is N-S elongated. The reservoir is 16 km long, and 5 km wide.

The Pohokura-1 gas well, Fig. 3, targeted the Kapuni group Mangahewa Formation sands in the Pohokura structure, where 700 m of shallow marine sands were encountered. The overall gas column extended to 130 m in the upper part of the Mangahewa structure. A deepening of the well was performed to potentially access the lower Mangahewa formation and reach the total depth in the mid-Eocene shales of the Omata Formation. The lower part of the formation was not economically viable and never produced gas condensates.

To measure the gas production performance, two drill stem tests were conducted in the upper section within the interval of 3,625 m to 3,634 m measured depth (MD) and between 3,553 m to 3,570 m MD. The flow measurements for the first interval were 3.5 million standard cubic feet per day (MMscfd), and 16.5 MMscfd for the second interval. The well was rather valuable in mapping the reservoir with seismic and having a control point for determining the overall structure of the Pohokura field.

The Mangahewa structure was identified as a prospect early in the exploration of the Taranaki Basin and was first drilled in 1961. Mangahewa-1 encountered some gas in the Kapuni Group, but at that point in time it was not considered to be sufficiently economic. Further exploration in the 1990s led to the drilling of the Mangahewa-2 discovery well in 1996. Following

Fig. 3 *The Pohokura-1 gas well log and formation characteristics.*

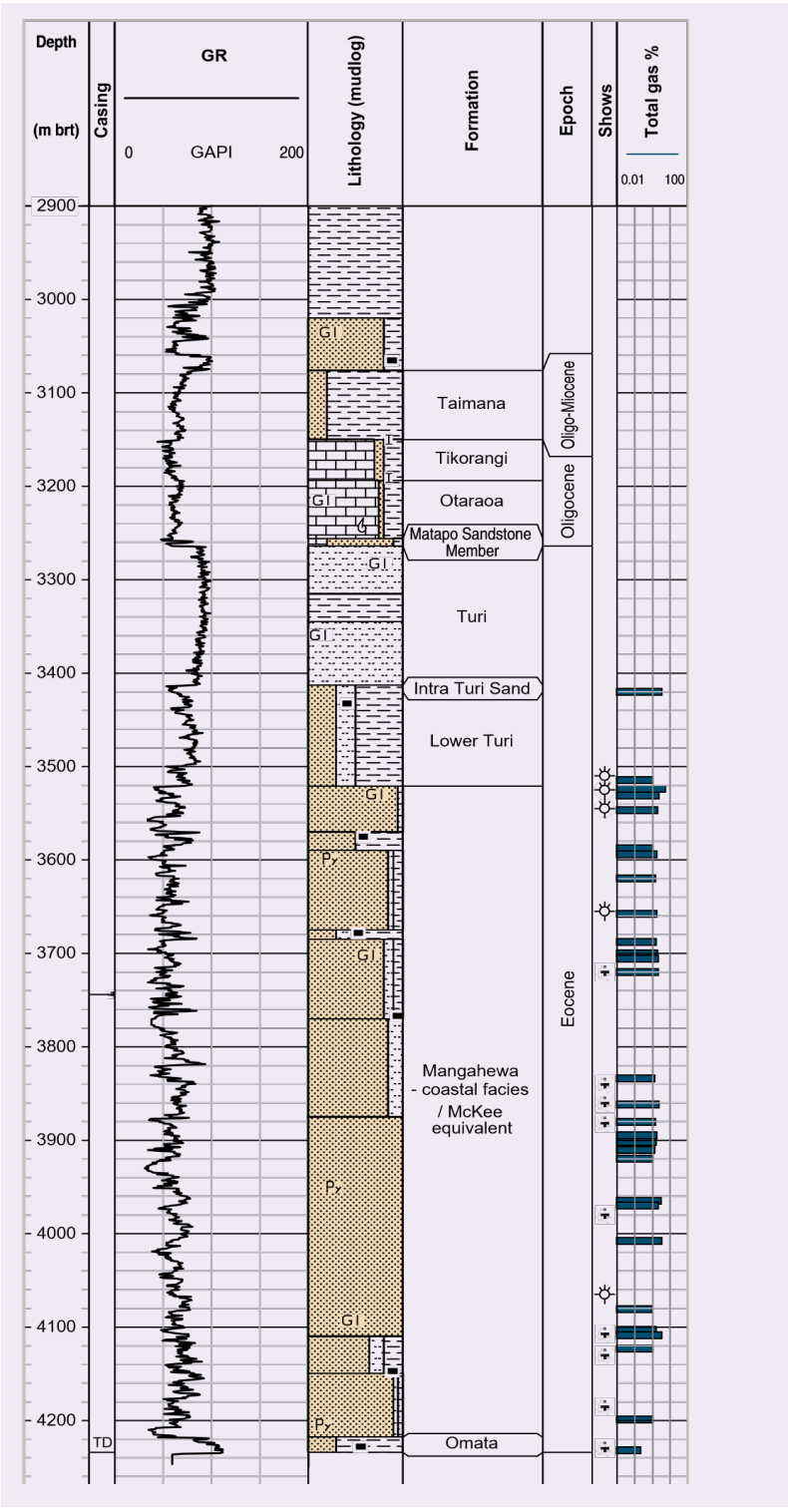

the flow tests, acquisition of 3D seismic in 1997, and appraisal of the northern flank of the structure with the Ohanga-2 well (1998), permanent production from the field started in September 2001[13]. Figure 4 is a diagram of the well log and formation characteristics.

Further appraisal wells, Mangahewa-3, Mangahewa-4, and Mangahewa-6, were drilled in the 2000s. The results of those appraisal wells provided the foundation for the Mangahewa Expansion Project that increased the project size and facilities. The Mangahewa is a gas condensate field located west of the McKee Field and 18 km southeast of New Plymouth. The structure is a broad, low relief anticline at Kapuni Group level, formed by regional shortening along the eastern margin of Taranaki Basin in the Early to mid-Miocene. The field is on the same broad structural trend as Pohokura, offshore to the north.

In the Mangahewa Field, the Eocene Mangahewa reservoir sands are sealed by intra-formational shales. Vertical isolation of the various reservoir layers is indicated by different fluid contents, gas composition, and pressures. The reservoir has been more deeply buried than it is today and reservoir porosity and permeability are relatively low as a result. Reservoir quality also varies from sand to sand, depending on grain size, diagenetic effects, and clay content. Porosities range up to 12%, and the main producing interval (MA-72) has an average porosity of 9%, and an average permeability of 4.5 mD. Production delivery relies on artificial fracturing of the reservoir[14].

The CPG study focuses on the Pohokura wells. Specifically, Pohokura-2 is the CO_2 injection well, while Pohokura-1 is the well producing the supercritical CO_2 that is then converted in the CPG production. For demonstration purposes, we simulated 3.5 years of the injection and production data for training the model with various expected CO_2 quantities. Figure 5 outlines the simulated injection and produced CO_2 quantities for Pohokura-1 and Pohokura-2. The CO_2 injection quantities vary throughout the simulation period, but incorporate the assumption that robust continuous injection is needed to satisfy continuous power demand achieved via CO_2 power production.

The deep learning framework then utilizes the simulated data for training and testing to develop an efficient artificial intelligence proxy model for geothermal energy production optimization. As previously indicated, the model is efficient to be evaluated within the optimization framework to support real-time decision making and adapt to power generation requirements. The simulated data were separated into a training and testing data set. The training period is from 0 to 2.8 years (80% of the data), and the testing period is from 2.8 to 3.5 years (20% of the data).

Figure 6 demonstrates the performance of the framework in estimating production levels. Forecasting performance for both the training and testing periods is strong, with the predictions being rather accurate in

Fig. 4 *The Mangahewa-2 well log and formation characteristics.*

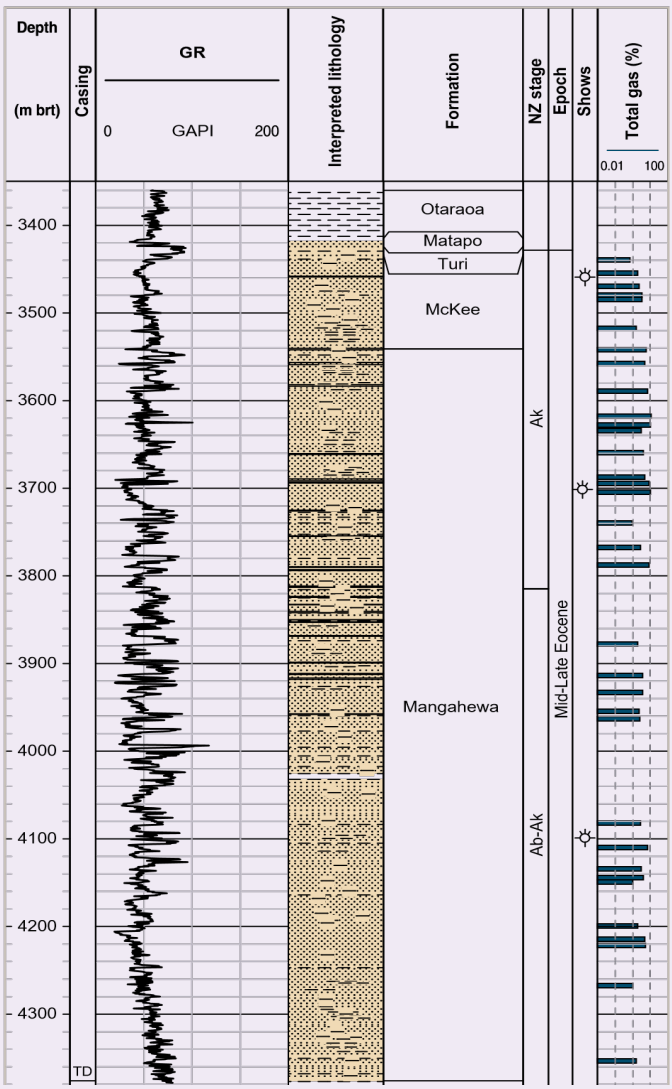

Fig. 5 *The simulated injection and produced CO_2 data for the Pohokura-1 and Pohokura-2 wells.*

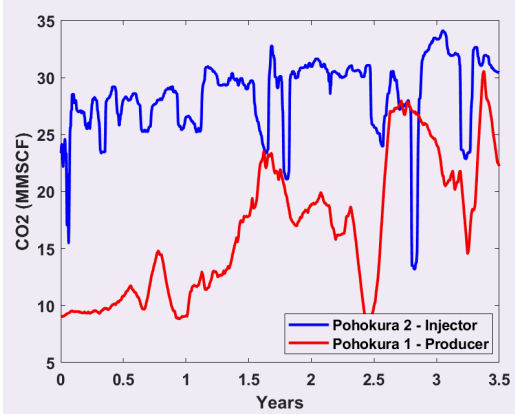

relation to the actual data. For the study, this provided sufficient confidence.

Figure 7 visualizes the CO_2 demand profile based on the power generation requirements. The assumption is that there is a cyclical power demand with intermittent off- and on-peak periods.

The optimized injection profile is then provided in Fig. 8, which shows an adequate adaptation between the high and low production times for satisfying the CO_2 demand profile. The injection profile sufficiently adapts to the variations in power demand, being able to sufficiently forecast well in advance the peak demands and inject the CO_2 to satisfy demand.

Conclusions

CPG has become an attractive geothermal energy production technology in which CO_2 is utilized for the production of electricity from reservoirs. CPG does not necessarily rely on shallow natural hydrothermal locations but can utilize conventional sedimentary basins, and it allows for harvesting energy even in low temperature environments that are conventionally not economically viable for geothermal extraction.

We present a new deep learning optimization framework for the maximization of power generation from a CPG system. The framework utilizes an adapted N-BEATS approach. The approach is based on a stack of ensembled feedforward networks that are also stacked by interconnecting backcast and forecast links. The advantages of the framework are its flexibility with respect to different input parameters and various forecastable time series. This is particularly important for CPG to easily capture variations in the temporal dynamics and temperature responses across the various CO_2 injection and production wells.

We evaluated the framework on a simulated CO_2 storage reservoir based in the Taranaki Basin in New Zealand. The Taranaki Basin has been well studied for CO_2 storage given the presence of a large saline aquifer that may be well suitable for both CO_2 storage and CPG energy production. We simulated four years of CO_2 injection and production for geothermal energy production as input to the N-BEATS framework. Training performance of the network was strong, and the model's performance was then evaluated on a subsequent three years of energy production. The deep learning framework is then integrated into a global optimization framework to optimize energy production while adapting CO_2 injection.

The new deep learning N-BEATS optimization framework for CPG power generation represents an innovative way to enhance energy generation from CO_2 storage reservoirs, providing a sustainable way to minimize the carbon footprint while delivering energy.

Acknowledgments

This article was prepared for presentation at the SPE Annual Technical Conference and Exhibition, Houston, Texas, October 3-5, 2022.

Fig. 6 *A comparison of estimated vs. actual performance.*

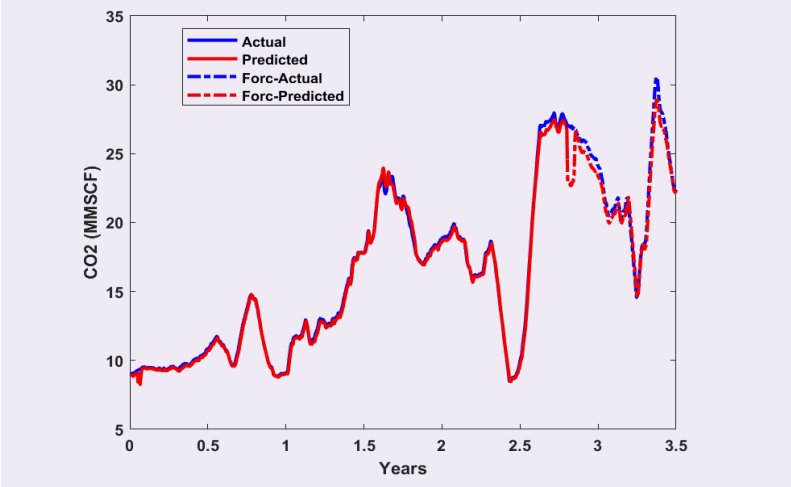

Fig. 7 *The CO_2 demand profile for power generation requirements.*

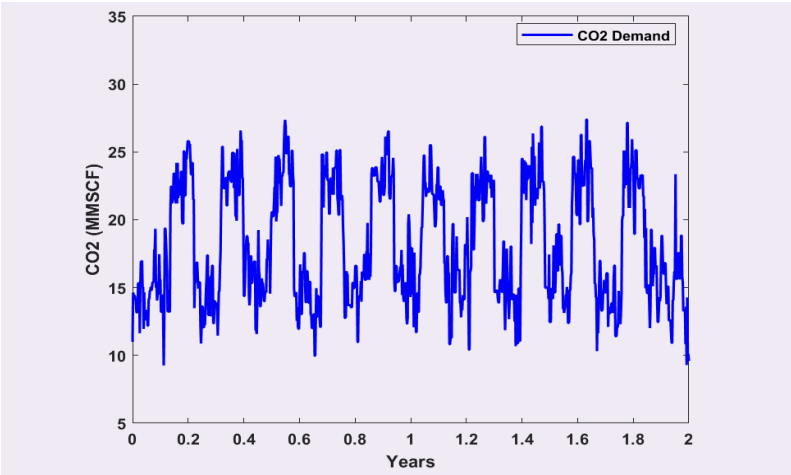

Fig. 8 *The optimized CO2 injection profile for satisfying the CO_2 power demand profile.*

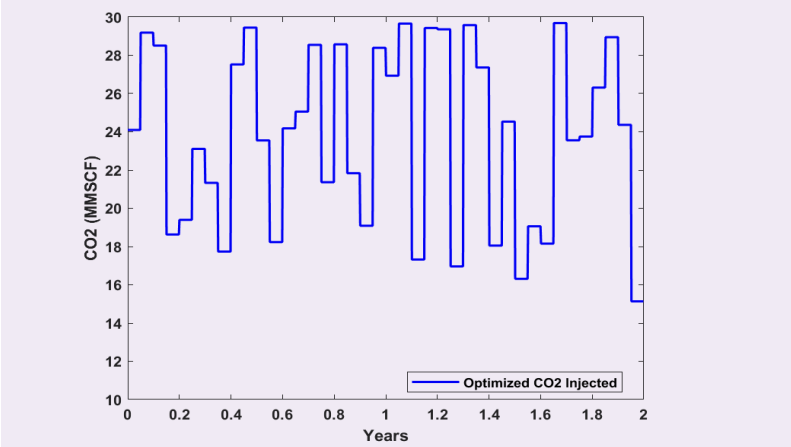

References

1. Boot-Handford, M.E., Abanades, J.C., Anthony, E., Blunt, M.J., et al.: "Carbon Capture and Storage Update," *Energy & Environmental Science*, Vol. 7, Issue 1, January 2014, pp. 130-189.
2. Rackley, S.A.: *Carbon Capture and Storage*, 2nd edition, Elsevier Inc., 2017, 698 p.
3. Ghiat, I. and Al-Ansari, T.: "A Review of Carbon Capture and Utilization as a CO_2 Abatement Opportunity within the EWF Nexus," *Journal of CO_2 Utilization*, Vol. 45, March 2021.
4. Tursunov, O., Kustov, L. and Kustov, A.: "A Brief Review of Carbon Dioxide Hydrogenation to Methanol Over Copper and Iron Based Catalysts," *Oil & Gas Science and Technology — Rev. IFP Energies Nouvelles*, Vol. 72, Issue 5, September-October 2017.
5. Adams, B.M., Kuehn, T.H., Bielicki, J.M., Randolph, J.B., et al.: "A Comparison of Electric Power Output of CO_2 Plume Geothermal (CPG) and Brine Geothermal Systems for Varying Reservoir Conditions," *Applied Energy*, Vol. 140, February 2015, pp. 365-377.
6. Ezekiel, J., Adams, B.M., Saar, M.O. and Ebigbo, A.: "Numerical Analysis and Optimization of the Performance of CO_2-Plume Geothermal (CPG) Production Wells and Implications for Electric Power Generation," *Geothermics*, Vol. 98, January 2022.
7. Esteves, A.F., Santos, F.M. and Magalhaes Pires, J.C.: "Carbon Dioxide as Geothermal Working Fluid: An Overview," *Renewable and Sustainable Energy Reviews*, Vol. 114, October 2019.
8. Ezekiel, J., Ebigbo, A., Adams, B.M. and Saar, M.O.: "Combining Natural Gas Recovery and CO_2-Based Geothermal Energy Extraction for Electric Power Generation," *Applied Energy*, Vol. 269, July 2020.
9. Oreshkin, B.N., Dudek, G., Pełka, P. and Turkina, E.: "N-BEATS Neural Network for Mid-Term Electricity Load Forecasting," *arXiv:2009.11961v3* [cs.LG], 2021.
10. Sbrana, A., Rossi, A.L.D. and Naldi, M.C.: "N-BEATS-RNN: Deep Learning for Time Series Forecasting," paper presented at the 19th IEEE International Conference on Machine Learning and Applications, Miami, Florida, December 14-17, 2020.
11. Islam, M.A., Yunsi, M., Talha Qadri, S.M., Shalaby, M.R., et al.: "Three-Dimensional Structural and Petrophysical Modeling for Reservoir Characterization of the Mangahewa Formation, Pohokura Gas-Condensate Field, Taranaki Basin, New Zealand," *Natural Resources Research*, Vol. 30, Issue 3, February 2021, pp. 371-394.
12. Sim, C.Y. and Adam, L.: "Are Changes in Time — Lapse Seismic Data due to Fluid Substitution or Rock Dissolution? A CO_2 Sequestration Feasibility Study at the Pohokura Field, New Zealand," *Geophysical Prospecting*, Vol. 64, Issue 4, June 2016, pp. 967-986.
13. Gundersen, B.N. and MacDonald, P.: "Todd v Shell and OMV: Implications for JV Parties of Using Model Agreements," *The Journal of World Energy Law & Business*, Vol. 4, Issue 2, June 2011, pp. 193-194.
14. Knox, D.A., Parr, I., Tan, I., de Lange, F., et al.: "New Zealand Gas Development Sets New Performance and Environmental Milestones Onshore and Offshore — The Role of Drilling Fluid Selection and Performance in the Pohokura Development," SPE paper 114653, presented at the SPE Asia Pacific Oil and Gas Conference and Exhibition, Perth, Australia, October 20-22, 2008.

About the Authors

Dr. Klemens Katterbauer

Ph.D. in Petroleum Engineering, King Abdullah University of Science and Technology

Dr. Klemens Katterbauer is a Petroleum Scientist working in the Reservoir Engineering Technology Division of Saudi Aramco's Exploration and Petroleum Engineering Center – Advanced Research Center (EXPEC ARC), where he uses his experience as a Petroleum Engineer and software developer to focus on the development of the latest Fourth Industrial Revolution IR 4.0 technologies for reservoir engineering applications.

Klemens has a proven track record having developed data driven uncertainty frameworks for enhancing oil recovery and strengthening sustainability of existing oil and gas reservoirs. A strong focus was laid on solar and wind energy and providing dedicated solutions for optimizing grid transfer rates, reduce downtime, and enhance efficiency in the power transmission.

He has in recent years developed some major technologies, such as enhanced artificial intelligence technologies for tracking waterfronts in subsurface reservoirs, and forecasting their movements. Furthermore, Klemens has developed robotics systems for enabling real-time logging while drilling, as well as subsurface sensing and logging operations.

Having been an experienced young professional member in several energy related societies, he has been an active member and heavily focused on mentoring young students that may dream to go into the oil and gas industry. In doing so, Klemens has advised several students and assisted them in broadening their expertise to focus on learning about new digital technologies, code development, as well as robotics.

He received his M.S. degree in Petroleum Engineering from Heriot-Watt University, Edinburgh, Scotland, U.K. Klemens received his Ph.D. degree in Petroleum Engineering from King Abdullah University of Science and Technology, Thuwal, Saudi Arabia.

Dr. Abdulaziz S. Al-Qasim

Ph.D. in Petroleum Engineering, University of Tulsa

Dr. Abdulaziz S. Al-Qasim is a Petroleum Engineer and a Champion of Enhanced Oil Recovery Monitoring and Surveillance on the Reservoir Engineering Technology team of Saudi Aramco's Exploration and Petroleum Engineering Center – Advanced Research Center (EXPEC ARC). Since joining Saudi Aramco in 2007, he has been involved in enhanced oil recovery and improved oil recovery projects, reservoir management, field development, and production related challenges. Abdulaziz's experience includes working in a variety of departments within Saudi Aramco.

He has more than 40 patents, disclosed and granted, with many providing innovative sustainability and decarbonization solutions. Abdulaziz has written more than 30 technical papers and journals, and deployed many technologies.

He was selected to serve as a member of the Saudi Ministry of Energy (MoE) and King Abdulaziz City for Science and Technology (KACST) joint CCUS committee. Abdulaziz was selected as one of the Hart Energy E&P's "40 under Forty" 2021 honoree for his contributions to advancing E&P innovations. He was selected to join the CERAWeek 2021 Future Energy Leaders program.

Abdulaziz is a member of the World Energy Council Future Energy Leaders (FEL-100) Board. He was named as one of Standard & Poors 2020 Global Platts Energy Rising stars and as one of the "World Oil" innovative thinkers of the year.

In 2020, Abdulaziz was recognized by the Energy Institute in 2019 as one of the young energy professionals of the year. He previously served as a Vice Chairman of the Society of Petroleum Engineers-Young Professionals (SPE-YP) regional symposium held in Oman in February 2009. Abdulaziz has also served in numerous SPE events at different levels.

He received his B.S. degree in 2007 from King Fahd University of Petroleum and Minerals (KFUPM), Dhahran, Saudi Arabia; his M.S. degree in 2011 from the University of Texas at Austin, Austin, TX; and his Ph.D. degree in 2016 from the University of Tulsa, Tulsa, OK, all in Petroleum Engineering.

Dr. Abdallah A. Alshehri

Ph.D. in Electrical Engineering, Georgia Institute of Technology

Dr. Abdallah A. Alshehri is the champion of the Deep Diagnostic team with Reservoir Engineering Technology in Saudi Aramco's Exploration and Petroleum Engineering Center – Advanced Research Center (EXPEC ARC).

He is undertaking various industry leading research projects to develop novel technologies to increase hydrocarbon discovery and reservoir recovery, capitalizing on Fourth Industrial Revolution technologies and artificial intelligent (AI) technologies.

Abdallah has received several national and international awards, including the 2022 ADIPEC Award on FracBots: The Next Real Reservoir IoT, the 2022 IOT Solutions World Congress Award for smart CO_2 downhole monitoring for sustainable reservoir operations, and the 2019 World Oil New Horizons Idea Award on the FracBots Technology.

He has more than 20 granted and disclosed patents, and more than 40 publications, including journal articles, book chapters, and conference papers.

Abdallah received his Ph.D. degree in Electrical Engineering from the Georgia Institute of Technology, Atlanta, GA.

Dr. Abdulkareem M. AlSofi

Ph.D. in Petroleum Engineering, Imperial College London

Dr. Abdulkareem M. AlSofi is a Reservoir Engineer with the Reservoir Engineering Technology Division of Saudi Aramco's Exploration and Petroleum Engineering Center – Advanced Research Center (EXPEC ARC). He is currently the champion of the chemical enhanced oil recovery focus area and is leading a new research initiative on heavy oil mobilization and recovery. Abdulkareem has also worked with the Reservoir Management, Reservoir Description and Simulation, and Reserves Assessment Departments.

He is the recipient of the 2009 Society of Petroleum Engineers (SPE) Annual Technical Conference and Exhibition Young Professional Best Paper Award in reservoir engineering, the recipient of the 2011 EXPEC ARC Best Presentation Award, and the recipient of the 2013 Middle East Young Engineer of the Year Award.

Abdulkareem has authored 15 conference papers and seven peer-reviewed journal papers.

In 2006, he received his B.S. degree from the University of Texas at Austin, Austin, TX, and in 2010, Abdulkareem received his Ph.D. degree from Imperial College London, London, U.K., both degrees in Petroleum Engineering.

Constraining Hydrocarbon Charge Factors Using Natural Tracers: A Modeling Study Applied to Hydrocarbon Migration and Accumulation

Dr. Constantin Sandu, Dr. Khaled Arouri and Dr. Ibrahim Z. Atwah

Abstract /

Estimating the amount of hydrocarbon initially in place (HCIIP) is important for optimizing the development of new fields and for efficiently allocating production resources. The current methods employed for the initial assessment of HCIIP are based on geological models that integrate the rock properties of the reservoirs over the structural geometry of the trap determined from petrophysical and seismic interpretations. Initial wells may be drilled to test the nature of fluids and confirm the presence of hydrocarbons. The tests typically do not place constraints on the size of the accumulation. More detailed methods, based on material balance or production history, for example, can only be applied post-drill after production is established.

In this article, we describe a method to estimate HCIIP based on a set of molecular tracers naturally occurring in crude oil. These tracers are a set of nitrogen compounds from the carbazole and benzocarbazole chemical series that are generated from source rocks along with the oil. The volumes of hydrocarbons accumulated in conventional reservoirs are a result of hydrocarbon fluid migration from the source rock to the trap location, often over considerable distances.

As oil and gas migrate and accumulate in the trap, the increasing volume of hydrocarbons is also accompanied by changes in the physicochemical properties of fluids as a result of differential migration and accumulation of various components forming the fluids. Subsequently, the carbazole compounds are extremely sensitive to the migration processes and their composition in the reservoir progressively evolves with oil accumulation.

The composition of tracers can be measured in small samples of oil collected from a pilot well drilled in a new prospect or extrapolated from offset wells. The measured composition is then used to constrain a tracer migration and accumulation model whose output can predict the HCIIP.

Using an in-house tracer composition simulator, multiple unconstrained models of the tracers' evolution are simulated for a particular petroleum system configuration. A free parameter within the models is used to control the charge of hydrocarbons to the trap, and for each simulation a pair of tracer composition vs. volume is calculated. An envelope function is then constructed that quantify the dissimilarity between the measured and simulated composition along the simulated interval. Finally, the predicted HCIIP corresponds to a minimum of the envelope function when plotted against the volume simulated. This facilitates constraining the HCIIP early in a field's life cycle.

Introduction

Production estimation is an important task that provides valuable input for business decisions regarding oil field development activities. Typically, production estimation methods are based on indirect calculations that require the integration of complex geological and engineering analyses[1]. Reservoir models, built using static data and simulations, can predict the production for specific well placement scenarios. Once the wells are drilled and production is established, initial production data points are added to the simulations, and model parameters are continuously updated to improve confidence in production forecasting[2].

Other methods combine field measurements with statistical modeling to obtain production ranges, with each range having assigned a risk estimate. These methods can be employed in the early stages of field development and be based on geological interpretations of seismic data acquired in the exploration phase and on regional information about the source and reservoir rocks properties.

A first step in estimating the production potential based on statistical methods is to estimate the amount of hydrocarbon initially in place (HCIIP)[3]. Today, this is accomplished by running basin simulations on geologic models built with a complete set of petroleum system elements. Basin simulators are complex applications designed to predict in place accumulations based on a set of parameters characterizing a particular geologic scenario[4, 5].

A conventional petroleum system consists of a source rock that underwent thermal maturation and generated hydrocarbons, a carrier bed represented by a permeable reservoir formation that facilitated migration, and a trap where the hydrocarbons accumulate in commercial quantities, Fig. 1. The accumulations are held in place by a sealing bed that prevents hydrocarbon leakage (not presented in Fig. 1).

Basin simulation starts by calculating the mass of hydrocarbons generated within the liquid and vapor phases from organic matter in the source rocks. The mass of components within the liquid (oil) and vapor (gas) is calculated using empirical kinetic schemes integrated over the thermal evolution of the source rock, and the mass is converted into volumes of each phase produced according to the mixture's phase diagram. The basin simulator calculates the fluxes of fluids migrating through the subterranean carrier beds and their subsequent accumulation in the reservoir.

Different solvers can be employed to determine the migration parameters, but the main goal of the simulation is to produce an estimate of the HCIIP and properties of the accumulated fluids. Current methods constrain the HCIIP only later in the field development phase. Estimating HCIIP through independent geochemical techniques can help constrain this parameter in the early stages of field development, thereby reducing uncertainties and cost.

This article presents such a technique to constrain the factors that determine the mass of hydrocarbons accumulated in a reservoir resulting from the compositional evolution of a set of molecular tracers present in the accumulated oil. The "tracers" referred to here are carbazoles, benzocarbazoles and their isomeric variants[6]. They are naturally generated from the same source rock as the oil and migrate along with oil as dissolved components[7, 8]. Carbazoles and derivatives can be identified and measured[9] in oil samples recovered from various locations in the oil field or from different fields. By deconvolving the composition of tracers measured in a test well or a set of wells, we can relate the tracer concentration and composition to the amount of oil in the reservoir expressed as a volume.

The composition, in our context, refers to the particular mixture of tracers in the accumulated oil at any moment in time. This can be defined by their relative proportions in the mixture and in general evolve during generation and migration. In this study we employed an in-house developed tracer migration modeling application, which simulates the compositional evolution of several tracer components as a result of the hydrocarbon migration processes occurring in the subsurface.

A correlation index is selected to assess the composition predicted by the simulation to the actual composition from a test well. The correlation index is assessed over the entire range of simulations to create a filling envelope function. Because the filling envelope function shows the relationship between the expected composition of tracers and the corresponding in place amount of oil filling the trap, it serves as a probability function for the in place estimates. The predicted HCIIP is selected based on a critical point of the filling envelope function, e.g., the minimum error of measurement.

Numeric Modeling Application

We developed a simplified numeric petroleum system simulator that considers all the major components of basin and fluids evolution and includes a parameterization of the tracer component evolution. The simulator integrates the thermal evolution of a predefined source rock and calculates the mass of oil and tracer components generated according to their kinetic parameters. The oil represents the single bulk phase of the hydrocarbons generated, and it carries the tracers

Fig. 1 *A diagram showing two hydrocarbon migration paths within a generic petroleum system. Oil is generated within an area of mature source rock (MSR) and migrates in a carrier bed (reservoir type rock) to be trapped on various accumulations along the way (A, B, C). The volume accumulated within each trap is critical for the design of field development.*

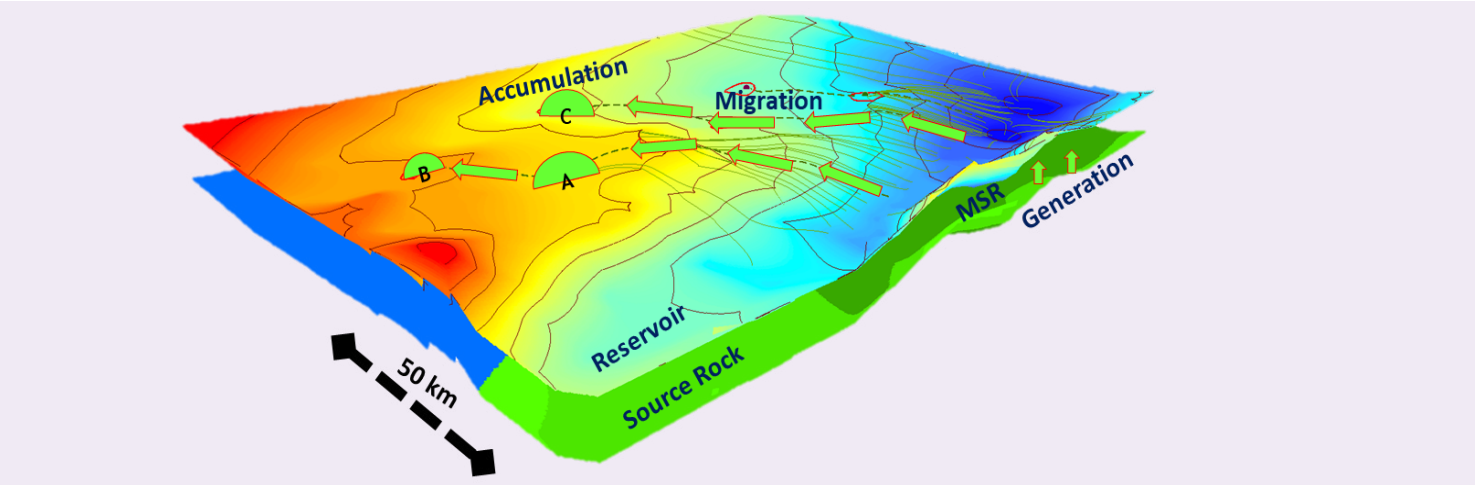

as dissolved components along the migration pathway. According to their individual kinetics, a set of tracers is also generated simultaneously in parallel with the oil.

A water phase is assumed to occupy all the pore spaces that are not occupied by oil. The flow system is a 1D representation of a migration pathway characterizing a petroleum system. It consists of a source rock and one or more flow segments. Each flow segment represents a portion of the carrier bed that serves as a migration conduit and ends with an accumulation. The goal of the simulator is to quantify expected tracer composition in oil accumulations, which is a net result of three processes: (1) generation of the tracers from the source rock simultaneous with the oil, (2) redistribution of the tracers along migration conduits, and (3) mixing during oil accumulation, Fig. 2.

Generation of the Bulk Oil Phase and of the Tracer Components

The hydrocarbon components found in a petroleum system, including the tracer components, are generated from the organic-rich portion of a source rock (kerogen). Kinetic models have been developed to calculate the component's yield for each source rock type[10]. Petroleum components can also be obtained in laboratory conditions by artificially maturing the source rock at much higher thermal regimens to compensate for the short timespan available for experiments.

Laboratory experiments are therefore useful for determining the kinetic parameters that can extrapolate the kinetic models over geologic time scales[11]. Like other hydrocarbon components, carbazole and derivatives are generated in source rock undergoing thermal maturation, and their distribution in source rock is affected by the maturation level[12].

Artificial heating experiments performed on source rocks have revealed that petroleum generating reactions are quasi-irreversible, and the reaction kinetics can be described by a first-order reaction rate[13]:

$$\frac{\partial y(t)}{\partial t} = k(T) * (1 - y(t)) \quad (1)$$

where y is the normalized mass of component generated as a function of time, t, and k is the reaction rate constant with an absolute temperature dependence, T (in Kelvin) in the form of the Arrhenius equation:

$$k(T) = Ae^{-E/RT} \quad (2)$$

where E is the activation energy of the reaction (in *J/mol* or *cal/mol*) and R is the gas constant (*J/(mol K)* or *cal/(mol K)*). The pre-exponential factor A has the dimension of a frequency (*1/s*), also termed frequency factor, and has been related to the vibration frequency. The values of E and A are determined from the analysis of laboratory heating experiments[14].

A pair of values are selected for the bulk phase and for each tracer component. Based on these values, the numeric simulator calculates the mass of oil and tracer components generated by integrating Eqn. 1 over geologic time. Since each component has different kinetic parameters, their generation rate is differentiated for the entire simulation time, Fig. 3.

The generated components dissolved in the bulk phase are expelled from the source rock and enter the migration channel of the carrier bed. The expulsion process is not 100% efficient, and the exact ratio of oil expelled vs. retained in the source represents a large source of uncertainty in the petroleum system analysis. The composition of tracers that enter the migration conduit are further altered due to the migration differentiation process.

Migration of the Bulk Phase and Redistribution of Tracers along Migration Conduits

The modeling application simulates the oil migration using a simplified invasion percolation algorithm[15]. The invasion percolation model is applied on a two-phase (oil and water) fluid to estimate the position of the oil migration front at any given moment. Each discretized volume of rock (cell) along the migration conduit, Fig. 4a, is characterized by a threshold saturation (S_{cr}) at which the migrating oil phase will form a cluster of saturated pores across the cell, Fig. 4b. Once enough

Fig. 2 *The relationship among processes involved in tracer differentiation. Each process affects the concentration of tracers at any moment in time. The petroleum system simulator quantifies the processes and calculates the evolution of each tracer.*

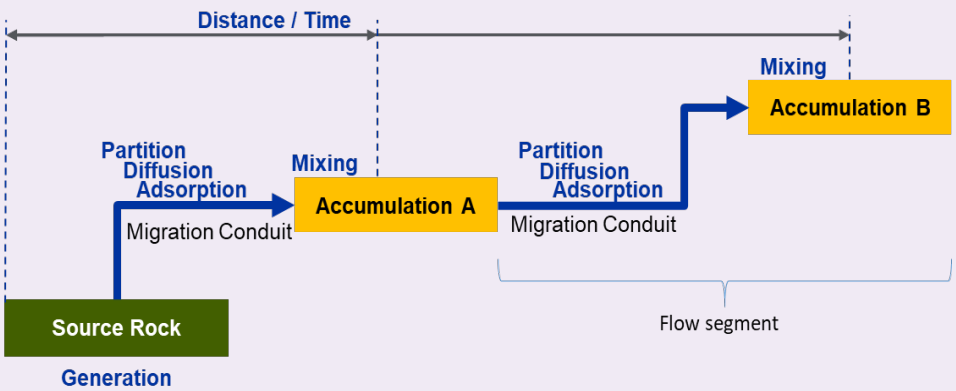

Fig. 3 *The generation history of the oil and tracer components resulting from the source rock evolution. Each tracer is generated at a different rate over time, resulting in a differentiated concentration evolution within the oil produced by the source rock.*

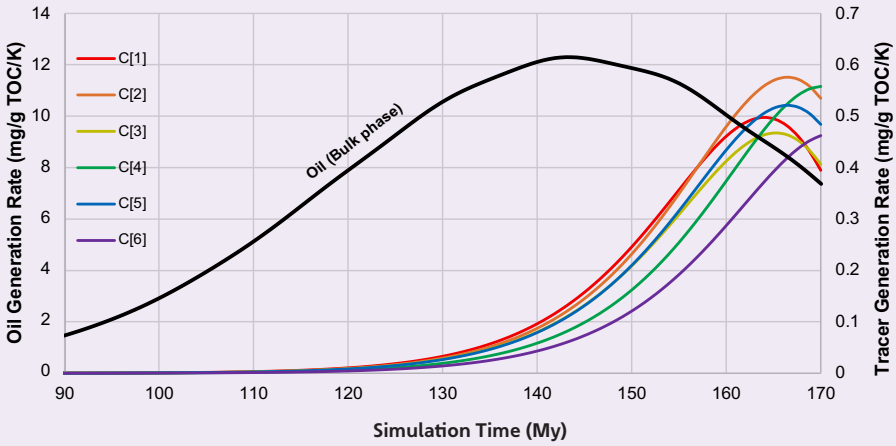

Fig. 4 *The basic elements of the numeric model: (a) Migration modeling using the petroleum system simulator. The simulator calculated the migration from cell to cell based on a threshold criterion applied to the volume of oil that is supplied by the source. (b) The section through a migration channel showing invaded and uninvaded cells. When a cell is invaded, the migration front moves to the next cell along the path. (c) The pore scale description of the processes modeled. The processes are upscaled to field size for mass balance calculations.*

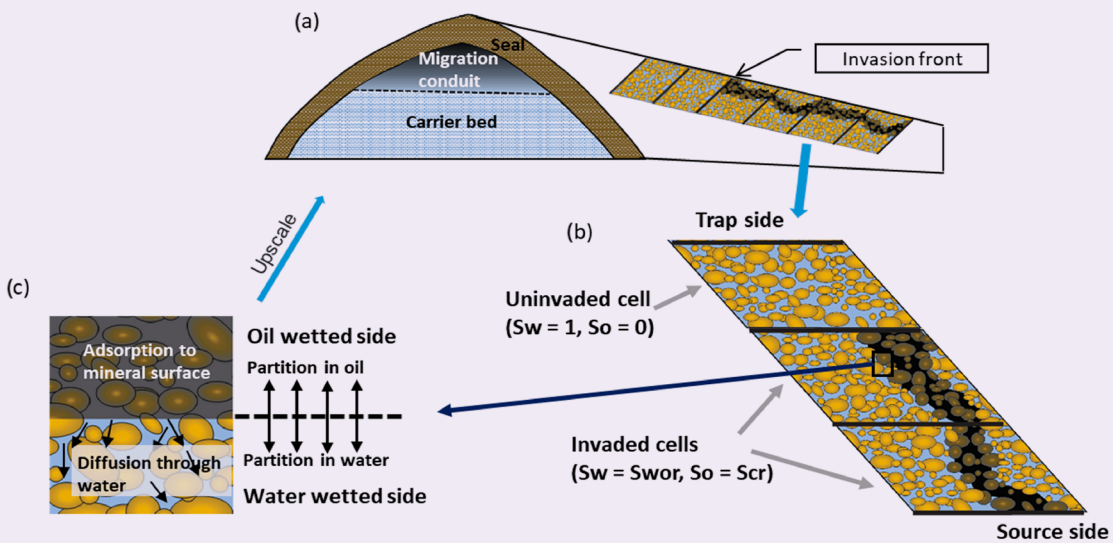

volume of oil is generated to saturate the cell at S_{cr}, the cell is invaded and the front moves forward. The relationship that relates the invaded volume, V_i, to the saturation can be expressed as:

$$V_i = S_o * \Phi * V_{cell} \quad (3)$$

where S_o is the oil saturation (equal to S_{cr} after invasion), Φ is the carrier formation porosity and V_{cell} is the volume of the migration cell. The V_{cell} is determined by the meshing algorithm and varies with the model resolution chosen.

The numeric simulator assumes that the bulk fluid phase will migrate at a certain distance and velocity, as the volume of oil expelled from the source rock can spread out while remaining fully interconnected through the invaded cells. Since every cell remains saturated at S_o after oil migrates through it, a volume of oil will be left in the migration channel along the entire length of the migration train. At any given moment, a mass balance of all tracer components is enforced within each cell that satisfies the processes affecting the tracer concentration.

Processes Affecting the Tracer Concentration along the Migration Path

The tracer components vary in both their absolute concentrations and relative composition along a migration pathway[16].

Three phases are considered for interaction within our model: the liquid hydrocarbons (oil), water, and the solid phase (mineral matrix). When oil migrates through a carrier bed, the tracer components present in the oil will redistribute partially into the other two phases. The three major distribution processes are: (1) partitioning into the water, (2) adsorption onto the surface of solid phases, and (3) diffusion in the water phase, Fig. 4c.

Adsorption to the solid phase takes place at the oil mineral contact. Adsorption can be treated as an instantaneous process at a geologic time scale, i.e., an equilibrium adsorption model may apply. The adsorption algorithm distributes the components between the rock matrix and the oil according to the equilibrium value of the concentration relative to a Freundlich-type adsorption isotherm[17]. The amount of each tracer component that partitions into the water phase is controlled by the diffusion process described by Fick's law[18].

Just as in the adsorption case, we assume a steady-state condition over geologic time scales. Therefore, the terms of Fick's law representing partial derivatives with respect to time are ignored. The diffusion coefficient in a porous medium is much smaller than that in free liquid[19]. Therefore, the diffusing particles acting in a porous space need to go around the mineral grains and cross a longer path related to tortuosity. The simulator scales this effect by using an effective diffusion coefficient to accommodate for the tortuosity. It was shown in laboratory experiments[20] and field data analysis[21, 22] that the described processes effectively alter the concentration of carbazole and benzocarbazole tracers along the migration conduit.

The second stage of tracer component distribution happens in the trap. When a trap is filled with fluids, oil begins to migrate further along the migration pathway, bypassing the accumulation and invading the next flow segment. Eventually, the migration front may encounter another trap and start filling it as long as enough oil is generated.

Tracers are continuously brought into the accumulation by the migrating oil, and their concentration increases until the trap is fully filled. Therefore, the tracer concentration in an accumulation: (1) positively correlates with oil volume, and (2) negatively correlates with migration distance. A migration model containing uncertain parameters that control the volume accumulated in a trap can therefore be constrained using the volume-concentration correlation.

Simulations of Oil Accumulation and Tracer Composition Evolution

The model in this example involves a single flow segment and defines a set of six tracers C[1] to C[6] to be monitored. In a simple scenario, the oil generated in the mature source rock (MSR) migrates upwards and laterally to accumulate in a trap within the reservoir formation, Fig. 1.

Assuming that a sample of the oil can be collected from the accumulation and the concentration of the tracers determined, we identify a scenario from tracer simulations that best matches these measured concentrations. This in turn will help constrain the volume of accumulation in the trap. Several input parameters are known that control the charge of the trap, and therefore the amount of in place hydrocarbons. For example, some of the most critical parameters include source

Table 1 *A set of free parameter values used as input for each simulation along with the corresponding in place volume accumulated and tracer concentrations.*

	Eff (%)	Oil Vol (m^3)	C[1] (ppm)	C[2] (ppm)	C[3] (ppm)	C[4] (ppm)	C[5] (ppm)	C[6] (ppm)
Simulation #1	0.1	3.16E+07	46.43	25.45	44.67	20.82	29.35	15.53
Simulation #2	0.2	6.32E+07	65.53	44.96	57.85	32.04	45.94	23.49
Simulation #3	0.3	9.48E+07	73.61	54.46	63.12	37.05	53.44	27.00
Simulation #4	0.4	1.26E+08	78.01	59.94	65.93	39.84	57.63	28.95
Simulation #5	0.5	1.58E+08	80.71	63.41	67.64	41.57	60.24	30.16
Simulation #6	0.6	1.90E+08	82.51	65.76	68.77	42.73	61.99	30.97
Simulation #7	0.7	2.21E+08	84.01	67.75	69.70	43.71	63.46	31.65
Simulation #8	0.8	2.53E+08	85.03	69.10	70.33	44.37	64.46	32.11
Field Measurement 1		TBD	83.1	67.5	68.2	44.3	62.5	31.9

rock quality, size of the MSR, expulsion efficiency, and leakage through the sealing formation.

In the simulations presented here, the source rock kinetic parameters were selected to match a classical Type II-S source rock. The expulsion efficiency, a parameter difficult to constrain, was selected as a free variable, i.e., a variable without independent constraints, in the simulations noted[23]. Table 1 presents the set of free parameter values used as input for each simulation along with the corresponding in place volume accumulated and tracer concentrations. The output of the simulations is then presented on a plot of tracer composition evolution vs. the predicted accumulated volume.

In Fig. 5, we present the graphical results of the simulations. The concentration of each tracer is plotted against the final oil volume (m^3) accumulated in place. The curves are interpolated from individual points representing each simulation result. The volume of oil is therefore continuously related to the tracer composition.

The simulation results represent an idealized case based on a simple model. The petroleum system is more complex and more challenging to constrain in real geological settings and field applications. Simulation of the tracers' evolution, which migrate through several kilometers of heterogeneous rocks, will likely produce a variable accuracy of the concentration of tracers in accumulation. We can improve the prediction by tracking multiple tracers to spot and filter outliers from field measurements. Index parameters based on tracer analyses were suggested to characterize migration distance[24, 25].

In this study we identified an index-based analysis that convolves multiple tracer concentrations and offers a simple application that can be used to estimate HCIIP in business decisions.

Data Analysis and Hydrocarbon Charge Estimation

As the amount of oil accumulated is to be determined based on the composition of tracers, a correlation index is defined first to relate the composition to the volume accumulated. Since simulations cannot estimate each individual tracer concentration with the same precision, defining a correlation index is a desirable approach to characterize the accumulation based on a set of multiple tracers.

A correlation index will statistically combine the predicted values for each tracer and compare them with a measured set of values from the field. Therefore, the correlation index is a derived parameter that takes a unique value at the location of the in place volume prediction. For example, the correlation index may be the mismatch between the average of all tracer components predicted and the measured concentration. We can call this the Error Factor (EF). A filling envelope function is built by interpolating the values of the EF obtained for each simulation point to create a single function that maps the EF to the volumes of oil accumulated.

In the first step, we calculate each tracer's simulation error in relation to the corresponding value measured in the field (Field Measurement 1 from Table 1). The difference between the measured value and predicted value for the concentration is applied to a normalized interval for each tracer component and plotted against the simulation volume accumulated, Fig. 6a:

$$Err_i(Vol) = \frac{cs_i(Vol) - cm_i}{cs_{i,max} - cs_{i,min}} \quad (4)$$

Fig. 5 *The results of numeric simulations showing a variation of concentration of each tracer component with the volume of oil produced. A set of six undefined tracers were selected for the simulation and the results of discrete simulations are interpolated to obtain the variation curves.*

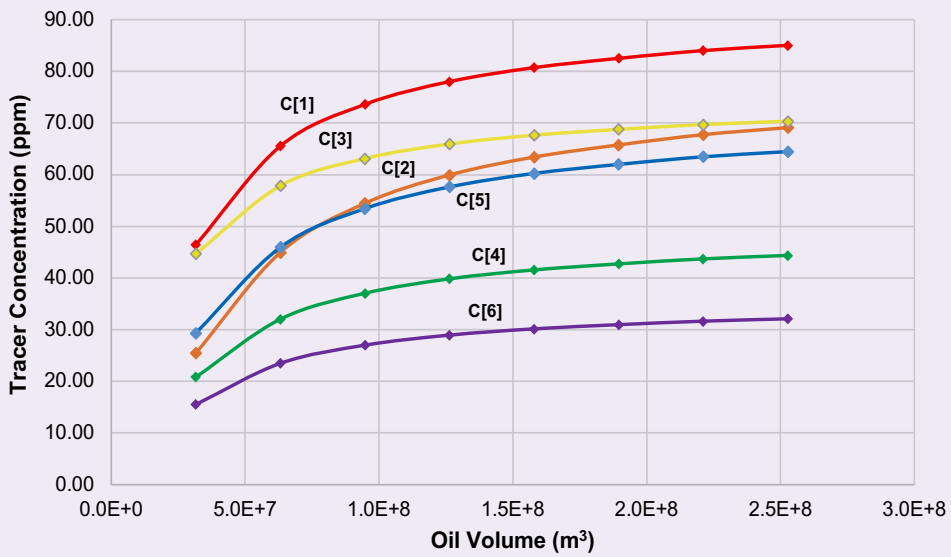

Fig. 6 *The in place volume estimation based on minimizing the field measurement error. (a) The relationship between the accumulated volume and an estimated error of the field measurement for each tracer concentration (normalized for all tracers). (b) The filling envelope function derived by convolving all tracers' data and the in place volume prediction located at the minimum of the filling envelope function.*

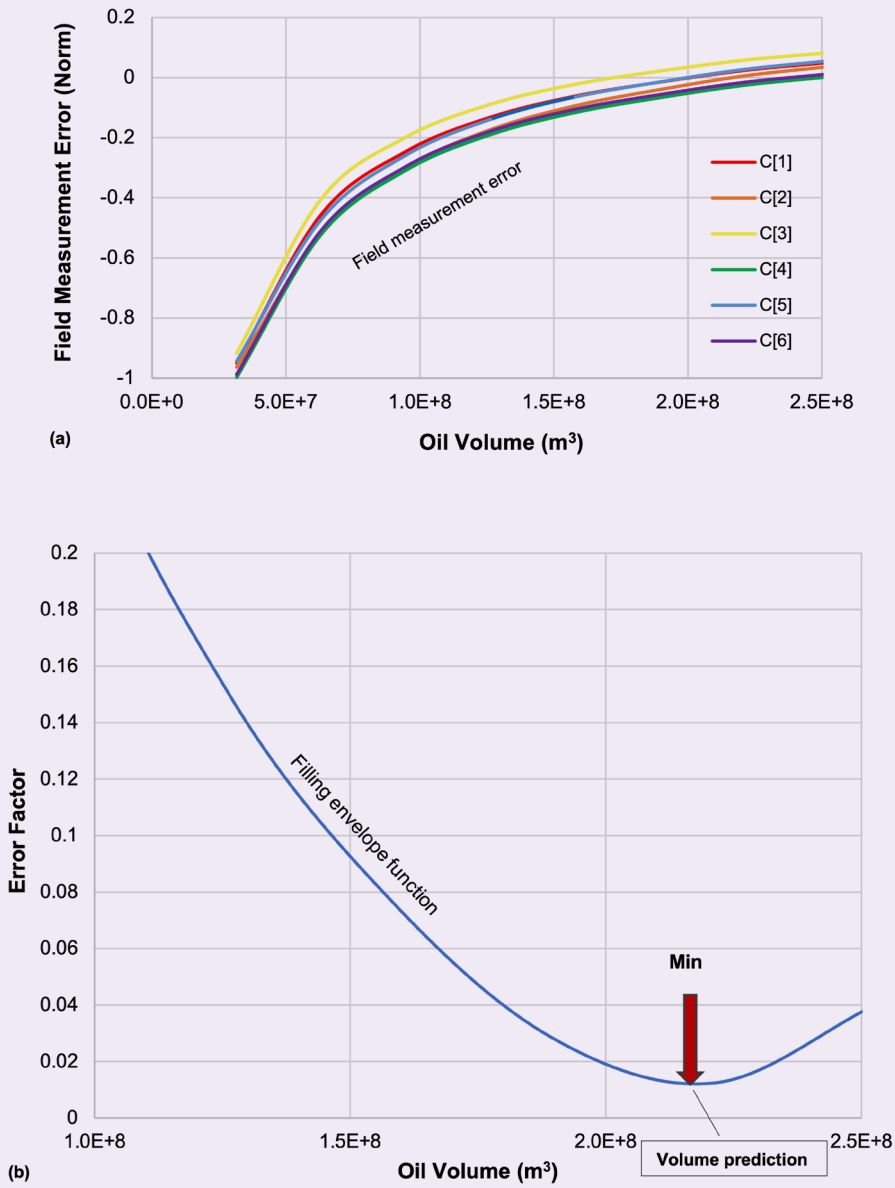

where $Err_i(Vol)$ is the error estimation for the simulated tracer component, i vs. the measured value, Vol is the simulated volume of accumulation, $cs_i(Vol)$ is the simulated concentration of tracer i, cm_i is the measured concentration of tracer i, and $cs_{i,max}$ and $cs_{i,min}$ are the maximum and minimum values of the simulated concentration of tracer i, respectively. An average of errors across all the tracers represents the EF index:

$$EF_i(Vol) = ABS\left[\frac{\sum_{i=1}^{n} Err_i(Vol)}{n}\right] \quad (5)$$

where n is the number of tracer components, and ABS is the absolute value function applied for convenience.

We obtain the filling envelope function by interpolating the EF_i points in the volume domain, Fig. 6b. The envelope filling function presents a minimum for the accumulated volume associated with the smallest simulation error of the tracer composition. This value of ~$2.2*10^8$ m^3 is the predicted volume of in place accumulation. Since the minimum of the envelope function represents a unique value, scripts can be easily programmed in most data analysis applications to build the envelope function and identify its minimum automatically.

There could be more than one accumulation in many

geological settings along the same migration path. As previously seen in the simple scenarios in Fig. 1, the volume in one accumulation (A) can subsequently spill and fill a second trap (B). It is beyond the scope of this article to study fill-spill migration scenarios. A first-order approach can assume that once the first trap is filled, the subsequent migration phase bypassed the accumulation and charged the second accumulation without any alteration of the tracer composition in the first accumulation.

In this case, once the volume in the first accumulation is constrained, the petroleum system simulator will also offer a prediction of composition in the second accumulation for each subsequent simulation covering the range of free parameters. Using the set of predicted compositions, a different filling envelope function can be derived similarly for the second accumulation and the in place oil volume can also be predicted for this location.

Conclusions

1. We presented a methodology to estimate the amount of in place resources based on combined analyses and simulations of a set of natural hydrocarbon tracers.
2. The method represents a practical tool for rapidly evaluating liquid HCIIP. Because the tracers are dissolved in the liquid phase of the hydrocarbons, the method is not suitable for accumulations where the gas component is significant, unless phase corrections are applied.
3. The case illustrated here represents a simplified scenario, but the method can be adapted for more complex settings if sufficient data is available to decompose the complexity into a number of simpler configurations.
4. A suggested workflow for rapid estimates is presented in Fig. 7. The main steps consist of building a petroleum system model of a geologic scenario, identifying a free parameter of the model, which has a large uncertainty and is a controlling factor for the HCIIP volume, and creating a filling envelope function by comparing a tracer composition measured in the field with a set of compositions resulted from the model simulations that account for the uncertainty range of the free parameter. If a minimum is not identified, the range may be extended manually or by using a predefined search algorithm.

Fig. 7 *The general workflow to estimate the volume of oil initially in place.*

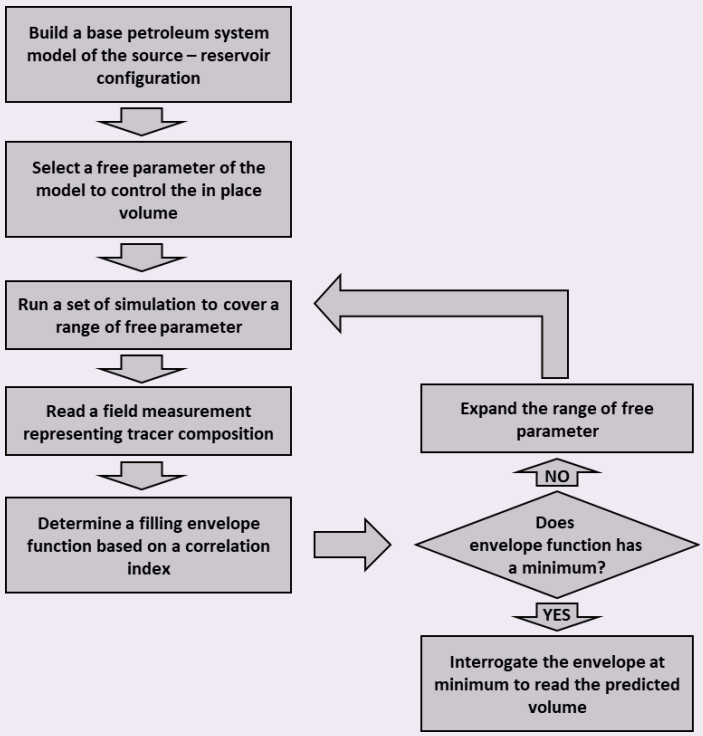

References

1. Sustakoski, R.J. and Morton-Thompson, D.: "Reserves Estimation," Chapter in Part 10 of *Development Geology Reference Manual*, (eds.) Morton-Thompson, D. and Woods, A.M., AAPG, 1993, 550 p.
2. Fetkovich, M.J., Fetkovich, E.J. and Fetkovich, M.D.: "Useful Concepts for Decline Curve Forecasting, Reserve Estimation, and Analysis," *SPE Reservoir Engineering*, Vol. 11, Issue 1, February 1996, pp. 13-22.
3. Matthews, M.D.: "Migration of Petroleum," Chapter 7 in *Exploring for Oil and Gas Traps*, (eds.) Beaumont, E.A. and Foster, N.H., AAPG, 1999, 1150 p.
4. Al-Hajeri, M.M., Al Saeed, M., Derks, J., Fuchs, T., et al.: "Basin and Petroleum System Modeling," *Oilfield Review*, Vol. 21, Issue 2, June 2009.
5. Ungerer, P., Burrus, J., Doligez, B., Chénet, P.Y., et al.: "Basin Evaluation by Integrated Two-Dimensional Modeling of Heat Transfer, Fluid Flow, Hydrocarbon Generation, and Migration," *AAPG Bulletin*, Vol. 74, Issue 3, March 1990, pp. 309-335.
6. Larter, S.R., Bowler, B.F.J., Li, M., Chen, M., et al.: "Molecular Indicators of Secondary Oil Migration Distances," *Nature*, Vol. 383, October 1996, pp. 593-597.
7. Yang, Y. and Arouri, K.: "A Simple Geotracer Compositional Correlation Analysis Reveals Oil Charge and Migration Pathways," *Scientific Reports*, Vol. 6, Issue 1, March 2016.
8. Fang, R., Li, M., Wang, T-G., Liu, X-Q., et al.: "Trimethyldibenzothiophenes: Molecular Tracers for Filling Pathways in Oil Reservoir," *Journal of Petroleum Science and Engineering*, Vol. 159, November 2017, pp. 451-460.
9. Frolov, E.B.: "Liquid Chromatography of Petroleum Carbazoles," *Organic Geochemistry*, Vol. 26, Issues 1-2, January 1997, pp. 43-47.
10. Pepper, A.S. and Corvi, P.J.: "Simple Kinetic Models of Petroleum Formation. Part I: Oil and Gas Generation from Kerogen," *Marine and Petroleum Geology*, Vol. 12, Issue 3, 1995, pp. 291-319.

11. Ungerer, P. and Pelet, R.: "Extrapolation of the Kinetics of Oil and Gas Formation from Laboratory Experiments to Sedimentary Basins," *Nature*, Vol. 327, May 1987, pp. 52-54.

12. Clegg, H., Horsfield, B., Wilkes, H., Damsté, J.S., et al.: "Effect of Artificial Maturation on Carbazole Distributions, as Revealed by the Hydrous Pyrolysis of an Organic-Sulfur-Rich Source Rock (Ghareb Formation, Jordan)," *Organic Geochemistry*, Vol. 29, Issue 8, December 1998, pp. 1953-1960.

13. Schenk, H.J., Horsfield, B., Krooss, B., Schaefer, R.G., et al.: "Kinetics of Petroleum Formation and Cracking," Chapter 4 in *Petroleum and Basin Evolution*, (eds.) Welte, D.H., Horsfield, B. and Baker, D.R., Springer, 1997, pp. 231-269.

14. Lewan, M.D.: "Evaluation of Petroleum Generation by Hydrous Pyrolysis Experimentation," *Philosophical Transactions of the Royal Society of London. Series A, Mathematical and Physical Sciences*, Vol. 315, Issue 1531, July 1985, pp. 123-134.

15. Carruthers, D.J.: "Modeling of Secondary Petroleum Migration Using Invasion Percolation Techniques," Chapter 3 in *Multidimensional Basin Modeling*, (eds.) Duppenbecker, S. and Marzi, R., AAPG, 2003.

16. Yang, Y., Aplin, A.C. and Larter, S.R.: "Mathematical Models of the Distribution of Geotracers during Oil Migration and Accumulation," *Petroleum Geoscience*, Vol. 11, Issue 1, February 2005, pp. 67-78.

17. Ayawei, N., Ebelegi, A.N. and Wankasi, D.: "Modeling and Interpretation of Adsorption Isotherms," *Journal of Chemistry*, Vol. 2017, September 2017.

18. Cussler, E.L.: "Diffusion in Dilute Solutions" Chapter 2 in *Diffusion — Mass Transfer in Fluid Systems*, Cambridge University Press, 1997, pp. 13-49.

19. Huseby, O., Haugan, A., Sagen, J., Muller, J., et al.: "Transport of Organic Components from Immobile and Bypassed Oil in Porous Media," *AIChE Journal*, Vol. 49, Issue 5, May 2003, pp. 1085-1094.

20. Larter, S.R., Bowler, B.F.J., Clarke, E., Wilson, C., et al.: "An Experimental Investigation of Geochromatography during Secondary Migration of Petroleum Performed under Subsurface Conditions with a Real Rock," *Geochemical Transactions*, Vol. 1, Issue 9, October 2000.

21. Li, M., Larter, S.R., Stoddart, D. and Bjorøy, M.: "Fractionation of Pyrrolic Nitrogen Compounds in Petroleum during Migration: Derivation of Migration-Related Geochemical Parameters," in *The Geochemistry of Reservoirs*, (eds.) Cubitt, J.M. and England, W.A., Vol. 86, January 1995, pp. 103-123.

22. Han, Y., Poetz, S., Mahlstedt, N., Karger, C., et al.: "Fractionation of Pyrrolic Nitrogen Compounds during Primary Migration of Petroleum within the Barnett Shale Sequence of Marathon 1 Mesquite Well, Texas," *Energy & Fuels*, Vol. 32, Issue 4, March 2018, pp. 4638-4650.

23. Leythaeuser, D., Radke, M. and Schaefer, R.G.: "Efficiency of Petroleum Expulsion from Shale Source Rocks," *Nature*, Vol. 311, October 1984, pp. 745-748.

24. Zhang, L., Li, M., Wang, Y., Yin, Q-Z., et al.: "A Novel Molecular Index for Secondary Oil Migration Distance," *Scientific Reports*, Vol. 3, August 2013.

25. Faboya, O.L., Sonibare, O.O., Faboya, O.T., Agrawal, U., et al.: "Data Modeling for Crude Oil Migration Studies Using Ranking Method: A Rapid Geotracer Technique for Geochemists," *Acta Geochimica*, Vol. 37, 2018, pp. 901-910.

About the Authors

Dr. Constantin Sandu

Ph.D. in Geophysics,
Rice University

Dr. Constantin Sandu is a Research Geologist at the Aramco Americas Houston Research Center. In this role, he conducts research in quantitative geochemistry and geochemical modeling of petroleum systems, including modeling geochemical/geological processes and mechanisms of gas and oil generation, migration, accumulation, and alteration.

These research projects will help to improve the understanding and calibration of hydrocarbon migration in the subsurface by developing numeric models of migration and running laboratory experiments in geochemistry to constrain the model parameters. Constantin's research experience is in geophysical fluid dynamics and computation geochemistry.

He has more than 14 years of experience in petroleum exploration within the United States and Europe, having worked for leading service and operating oil companies. Constantin's main expertise is in petroleum systems analysis and basin modeling with experience acquired working multiple projects around the world in settings from simple clastic depositional structures to thrust belts and carbonate environments.

He is a contributor to several research papers, patents, and software applications.

Constantin received his B.S. degree in Geological Engineering from the University of Bucharest, Bucharest, Romania. He received his M.S. degree in Geology from the University of Houston, and his Ph.D. degree in Geophysics from Rice University, both in Houston, TX.

Constantin's academic research background ranges from organic geochemistry applied in petroleum systems to geophysical fluid dynamics and planetary evolution.

Dr. Khaled Arouri

Ph.D. in Petroleum Geochemistry and Basin Modeling,
Adelaide University

Dr. Khaled Arouri is a Senior Geological Consultant working in the Geology Technology Division of Saudi Aramco's Exploration and Petroleum Engineering Center – Advanced Research Center (EXPEC ARC). He joined Saudi Aramco in 2005, and leads projects to develop geochemical solutions to improve oil and gas exploration and field development.

With his team, Khaled won Aramco's CEO Excellence Award (2017), Effective Publications Award (multiple years), Best Mentor Award (multiple years), and the 2017 World Oil Award co-finalist for Best Exploration Technology.

He is a member of the American Association of Petroleum Geologists (AAPG), the Society of Petroleum Engineers (SPE), the European Association of Geoscientists and Engineers (EAGE), and the European Association of Organic Geochemists (EAOG).

Khaled served as the International SPE Distinguished Lecturer for the 2019-2020 season on fluid geochemistry, covering a number of SPE sections around the world, campaigning for the importance of integrating fluid geochemistry and pressure-volume-temperature within proper geological context.

He has authored and coauthored more than 100 technical papers in international journals, special volumes, conferences, and patents, and served on many regional and international conference and workshop committees.

In 1996, Khaled received his Ph.D. degree in Petroleum Geochemistry and Basin Modeling from the Australian School of Petroleum, Adelaide University, Adelaide, South Australia, followed by postdoctoral fellowships and consultancy in Australia until 2004, Assistant Professor and Research Coordinator at UAE University (2004-2005).

Dr. Ibrahim Z. Atwah

Ph.D. in Geology,
Texas A&M University

Dr. Ibrahim Z. Atwah is one of the Focus Area Champions in the Geology Technology Division of Saudi Aramco's Exploration and Petroleum Engineering Center – Advanced Research Center (EXPEC ARC). He is the team lead for the Geofluids and Basin Modeling Research team, which develops technologies to track hydrocarbon and non-hydrocarbon fluids in the subsurface from the original source to the accumulation trap.

Ibrahim joined Saudi Aramco in 2011 as a Research Geologist with EXPEC ARC as part of the research arm of the Exploration and Petroleum Engineering business line. During his early career, Ibrahim went through multiple assignments involving geological operations such as geosteering, resources assessment, and basin modeling.

Ibrahim has collectively published over 30 peer-reviewed and conference papers. His research interest is focused on the geochemistry and petrography of organic matter in sedimentary rocks and the associated petroleum fluids chemistry.

Ibrahim served as the Vice President for the American Association of Petroleum Geologists (AAPG) student chapter at Texas A&M University and continues to serve as a technical reviewer for several peer-reviewed scientific journals related to geochemistry, geology, and basin modeling.

He received his B.S. degree in Geology from the University of Tulsa, Tulsa, OK, his M.S. degree in Geology and Geochemistry from Oklahoma State University, Stillwater, OK. Ibrahim then received his Ph.D. in Geochemistry and Basin Modeling from Texas A&M University, College Station, TX.

2D Surface Roughness Quantification for Enhanced Petrophysical Applications

Dr. Gabriela Singer, Dr. Shouxiang M. Ma, Dr. Songhua Chen and Mahmoud Eid

Abstract /

Surface roughness is an essential rock parameter affecting petrophysical properties that are surface sensitive, such as characterization of pore structure and wettability. For instance, Wenzel's contact angle formula for rough surfaces requires knowledge of the surface roughness, as surface roughness is expected to speed up the aging of cores in crude oil for wettability restoration. In addition, proper quantification of surface roughness is critical for obtaining a representative, roughness independent, pore size for applications such as the prediction of permeability and interpretation of capillary pressure curves.

Intuitively, a surface is better characterized in 2D than in 1D. This 2D study is a continuation and enhancement of the previous 1D work[1]. In this current article, a comprehensive investigation of 1D vs. 2D surface roughness measurements is conducted to evaluate and cross validate the two approaches. In this study, surface roughness is measured on 26 carbonate rock samples by laser scanning confocal microscopy (LSCM), where both the 1D absolute increment surface roughness, *Sr*, as well as 2D interfacial area ratio of surface roughness, *Sdr*, are reported. As expected, results indicate that surface roughness characterized by 2D *Sdr* has a greater dynamic range than the 1D *Sr* measurement, i.e., the 2D *Sdr* provides a more representative characterization of surface roughness.

A detailed account of methodologies, assumptions, limitations, validation, and applications of the 1D and 2D surface roughness characterization is documented in this article. To extract the roughness features present on rock grain surfaces, effects of de-spiking and filter length, used to eliminate pore size effects, are investigated. For specific applications of surface roughness corrected pore size estimation from nuclear magnetic resonance (NMR) measurements, differences in length scales of surface roughness are compared between the LSCM measurement and that derived from NMR diffusion-T_2 plus Brunauer-Emmett-Teller (BET) surface area. The surface roughness corrected NMR pore size distribution is also validated against the pore size distribution obtained from measurement of micro-computed tomography (micro-CT) scanning.

Introduction

This study is a continuation and enhancement of a previous published study[1]. The previous work focused primarily on 1D measurement and data processing for characterizing rock surface roughness, and on integrating the extracted surface roughness into the mean pore body size determined from the Brunauer-Emmett-Teller (BET) measurement, thereby reducing uncertainties in the nuclear magnetic resonance (NMR) T_2-based pore body size computation, which requires the BET measurement as an input. To validate this integrated approach, a micro-computed tomography (micro-CT) based pore size distribution measurement was used as a reference and compared with NMR diffusion T_2 (D-T_2) measurements and pore geometry restricted diffusion analysis.

In this current study, 26 rock samples were selected for laser scanning confocal microscopy (LSCM) measurements. Intuitively, a 2D surface is better characterized in 2D than in 1D. 2D areal surface roughness is therefore computed, and the effect of various data processing parameters were investigated, including filter width, de-spiking, and the impact of surface preparation. This study reports the results of the 1D absolute increment surface roughness, *Sr*, and the 2D interfacial area ratio of surface roughness, *Sdr*, which are directly related to the surface relaxivity[2], a critical parameter for NMR data interpretation. The 2D *Sdr* is a standard roughness parameter defined in ISO 25178-2:2012[3]. Therefore, using 2D *Sdr* helps standardize our approach with the surface characterization community.

The optimized de-spiking and filter length affect the measured values of the surface roughness by less than 10%, thereby the result is considered robust. There is no significant difference in the measured surface roughness when the rock surface is prepared by sawing vs. breaking. For the rock samples tested, an excellent correlation is observed ($R^2 = 0.998$) between the simplified model-based 1D approach (*Sr*), and the more representative 2D surface roughness (*Sdr*), which strongly supports the conclusion that both methods are valid and interchangeable, with a correlation.

The data indicates that the 2D *Sdr* is more sensitive than the 1D *Sr*. The reported method for measuring the surface roughness can also be used on drill cutting samples, as long as the cuttings size is larger than the roughness features and the field of view (FOV) of the measurement.

Another measurement of the surface roughness is based on the difference in length scales (a.k.a., coarse graining length scales) between the D-T_2 and BET measurements[1]. Based on the difference between D-T_2 and BET derived surface relaxivities, this surface roughness is an indirect measurement and represents a bulk value, representative of the entire sample. One caveat is that the D-T_2 and BET method only works if the pores are small, i.e., if there is sufficient restriction in D-T_2, and if the formation factor is known. On the other hand, the LSCM *Sr* and *Sdr* are direct measurements of surface roughness, and is in general found to be larger than that from the D-T_2 and BET technique.

Based on this present study, the surface roughness measurement has many fundamental applications, including the following for enhanced formation evaluation, the main objective of this study.

1. Enhance pore size distribution from NMR measurement.
2. Enhanced mean pore size (d) for Kozeny-Carman equation with measurements of porosity (ϕ) grain density (ρ_g), BET surface area (SA_{BET}), and LSCM *Sdr*:

$$d = \frac{\phi}{1-\phi}\frac{6(1+2\,Sdr)}{\rho_g SA_{BET}} \quad (1)$$

Note that Eqn. 1 is based on the model of spherical pores and its performance is validated against the pore size from the roughness independent D-T_2 and micro-CT measurements. The d is the relevant pore size for permeability and capillary pressure.

In addition, our continued studies in surface roughness characterization also paves the way toward integrating this information into other applications such as:

- Evaluating CO_2 storage and transport in underground aquafers and depleted petroleum reservoirs.
- Obtaining the representative contact angle of rough surfaces (θ_m) for proper rock wettability characterization[4] using models like the Wenzel formula:

$$cos(\theta_m) = Sdr\ cos(\theta_\gamma) \quad (2)$$

where θ_m is the measured contact angle and θ_γ is the intrinsic contact angle on smooth surfaces.

Methodology

Surface Roughness Parameters; 1D and 2D

There are many different ways of characterizing solid surface roughness. The most commonly used parameters being the absolute surface roughness; the arithmetic average of the absolute values of the profile height, *Sa*, and the root mean squared surface roughness, which is the root mean square average of the profile heights, *Sq*:

$$Sa = \frac{1}{N^2}\sum_{i,j=1}^{N}\left|z(x_i, y_j)\right| \quad (3)$$

$$Sq = \sqrt{\frac{1}{N^2}\sum_{i,j=1}^{N} z(x_i, y_j)^2} \quad (4)$$

where $z(x_i, y_j)$, $i,j = \{1, 2, 3, \ldots, N\}$, is the raw data of the surface roughness measurement, after filtering.

Both *Sa* and *Sq* have dimensional units of length, and both only require measurement of z at location (x_i, y_j). The calculated roughness for both is with respect to the mean of the measurements, Fig. 1.

The dimensionless absolute *Sr* parameter relates to the surface relaxivity[2]. It is along the x axis (at a given position y) and is calculated first by comparing two neighboring measurements from $z(x_i, y_j)$ to $z(x_{i+1}, y_j)$:

$$S_r(y_j) = \frac{1}{N\Delta}\sum_{i=1}^{N}\left|z(x_{i+1}, y_j) - z(x_i, y_j)\right| = \frac{1}{N}\sum_x\left|\frac{\partial z}{\partial x}\right| \quad (5)$$

where the step size is:

$$\Delta = |x_{i+1} - x_i| = |y_{j+1} - y_j| \quad (6)$$

then *Sr* is computed by taking the average over the y axis:

$$Sr = \frac{1}{N}\sum_{j=1}^{N} S_r(y_j) = \frac{1}{N^2}\sum_y\sum_x\left|\frac{\partial z}{\partial x}\right| \quad (7)$$

Comparing $z(x_i, y_j)$, to its neighbor $z(x_{i+1}, y_j)$ implies that *Sr* is a relative measurement.

The equivalent of *Sr* in 2D is the dimensionless *Sdr*[3,5]. It signifies the rate of an increase in surface area calculated from the measured total surface area, A_1, over the projected area, A_0, Fig. 2:

$$Sdr = \frac{1}{N^2}\sum_y\sum_x\left(\sqrt{1 + \left(\frac{\partial z}{\partial x}\right)^2 + \left(\frac{\partial z}{\partial y}\right)^2} - 1\right) \quad (8)$$

The value of the 2D *Sdr* increases as the surface texture becomes finer and rougher.

Note that *Sdr* is a standard roughness parameter[5], therefore, using *Sdr* helps standardize our approach with the surface characterization community.

Fig. 1 *An illustration of surface roughness calculations (Eqns. 3, 4, 5, and 6) with respect to the z measurement at location x_i.*

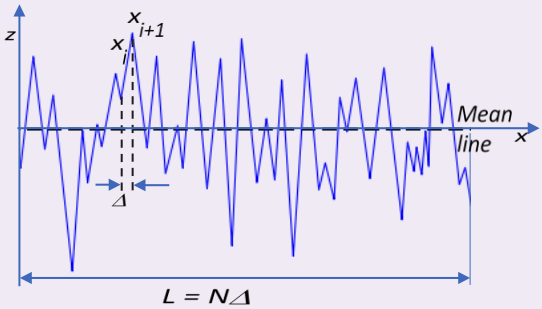

Fig. 2 *The* Sdr *is calculated from the surface area* A_1 *derived by the projected area* A_0[5].

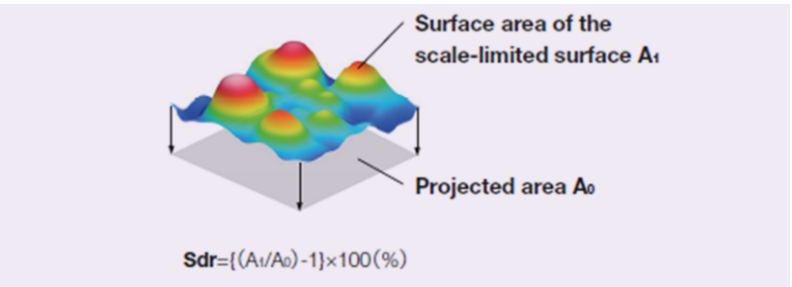

Another dimensionless surface roughness parameter is the root mean squared gradient of the surface roughness, which is the expansion of the profile 1D parameter *Sq*, indicating the mean magnitude of the local gradient (slope) of the surface. The surface is more steeply inclined as the value of the parameter *Sdq* becomes larger:

$$Sdq = \frac{1}{N^2}\sum_y \sum_x \left(\sqrt{\left(\frac{\partial z}{\partial x}\right)^2 + \left(\frac{\partial z}{\partial y}\right)^2}\right) \quad 9$$

2D Gaussian Filter and Filter Effect

Since the pore and grain surface is the only quantity of interest for surface roughness, the presence of pores on the rock surface complicates the surface roughness characterization. Because the length scale of a pore — both pore body and pore throat — is significantly larger than that of surface feature variations (with respect to the contour of the ideal smooth pore grain surface), this pore size effect needs to be filtered out from the raw surface roughness measurement. The filter should be carefully selected to remove the typical pore scale, but not to the scale of surface roughness.

In the previous study[1], a 1D filter was applied:

$$G(x) = \frac{1}{\sigma\sqrt{2\pi}} e^{-\frac{x^2}{2\sigma^2}} \quad 10$$

where σ is the size of the Gaussian filter.

In this study, the 2D Gaussian filter in Eqn. 11 is tested and implemented:

$$G(x,y) = \frac{1}{2\pi\sigma^2} e^{-\frac{x^2+y^2}{2\sigma^2}} \quad 11$$

For a given σ, the 2D filter averages signals over a larger area.

Fig. 3 *The effects of 1D (left) and 2D (right) Gaussian filter widths on five surface roughness parameters.*

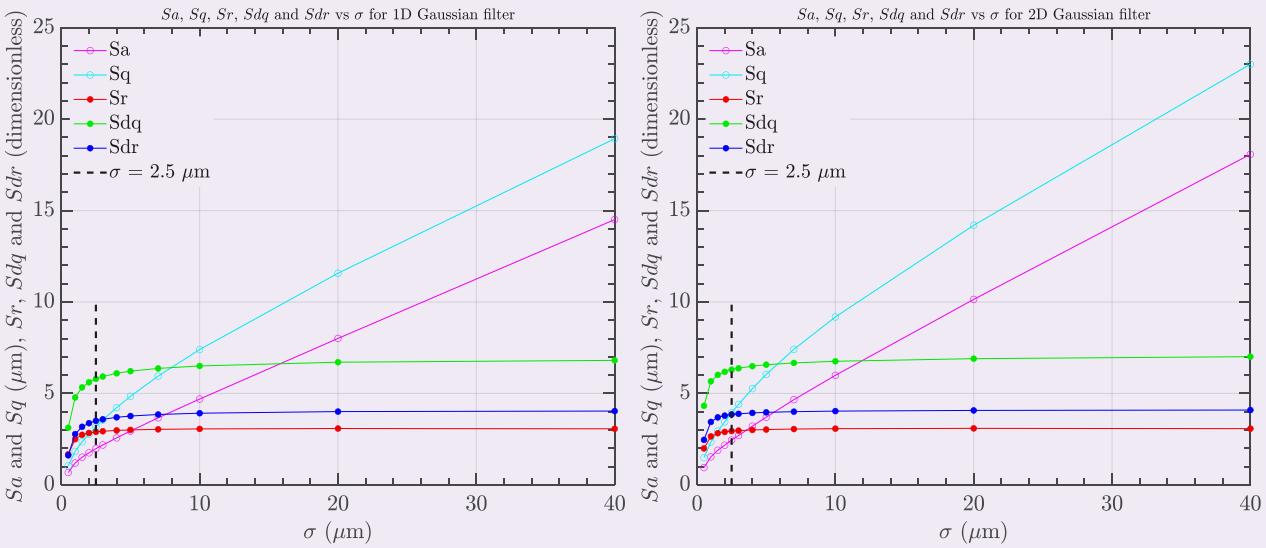

Table 1 *The effect of the filter width on* Sr *and* Sdr *normalized with that at* $\sigma = 2.5\,\mu m$.

σ (μm)	0.5	1	1.5	2	40
$Sr/Sr_{2.5\mu m}$	0.68	0.90	0.96	0.99	1.05
$Sdr/Sdr_{2.5\mu m}$	0.64	0.89	0.96	0.98	1.06

Fig. 4 *The effects of with and without filtering on three relative surface roughness parameters:* Sr, Sdr, *and* Sdq. *At* $\sigma = 2.5\ \mu m$ *the effects of filtering are 5%, 7%, and 12% lower than that without filtering.*

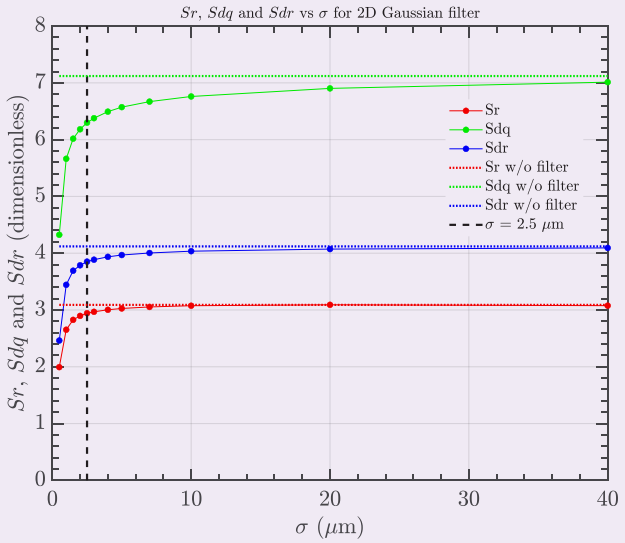

Dependence of Roughness Parameters on the Gaussian Filter Width σ

Figure 3 illustrates the effects of the 1D and 2D Gaussian filter widths, σ, on five roughness parameters. Both the 1D and 2D filters give comparable results. Parameters *Sa* and *Sq* increase monotonically with the filter width, while *Sr*, *Sdr*, and *Sdq* parameters initially increase with the filter width, then reach a plateau above σ = 2.5 µm. The filter has a significant effect on absolute roughness, *Sa* and *Sq*, but not on relative roughness *Sr*, *Sdr*, and *Sdq*, especially when $\sigma >$ 2.5 µm. Variations of *Sr* and *Sdr* normalized with that at $\sigma =$ 2.5 µm vs. σ are summarized in Table 1.

The effects of the 2D filter on *Sr*, *Sdr*, and *Sdq* are further studied in Fig. 4 by comparing the calculated values without a filter; the dash lines. From Fig. 4, it is observed that for $\sigma >$ about 2.5 µm, the filter does not have a significant effect on *Sr*, *Sdr*, and *Sdq*. At $\sigma =$ 2.5 µm, the filtered values are 5%, 7%, and 12% lower than the values obtained without filtering, i.e., the effect of the filter width on

Fig. 5 *An example of the LSCM raw and filtered data. The top panel shows the raw data in different views; 2D map on the left and 3D cube on the right. In the bottom panel, the 2D Gaussian filter of* $\sigma = 2.5\ \mu m$ *is shown on the left and the filtered data on the right.*

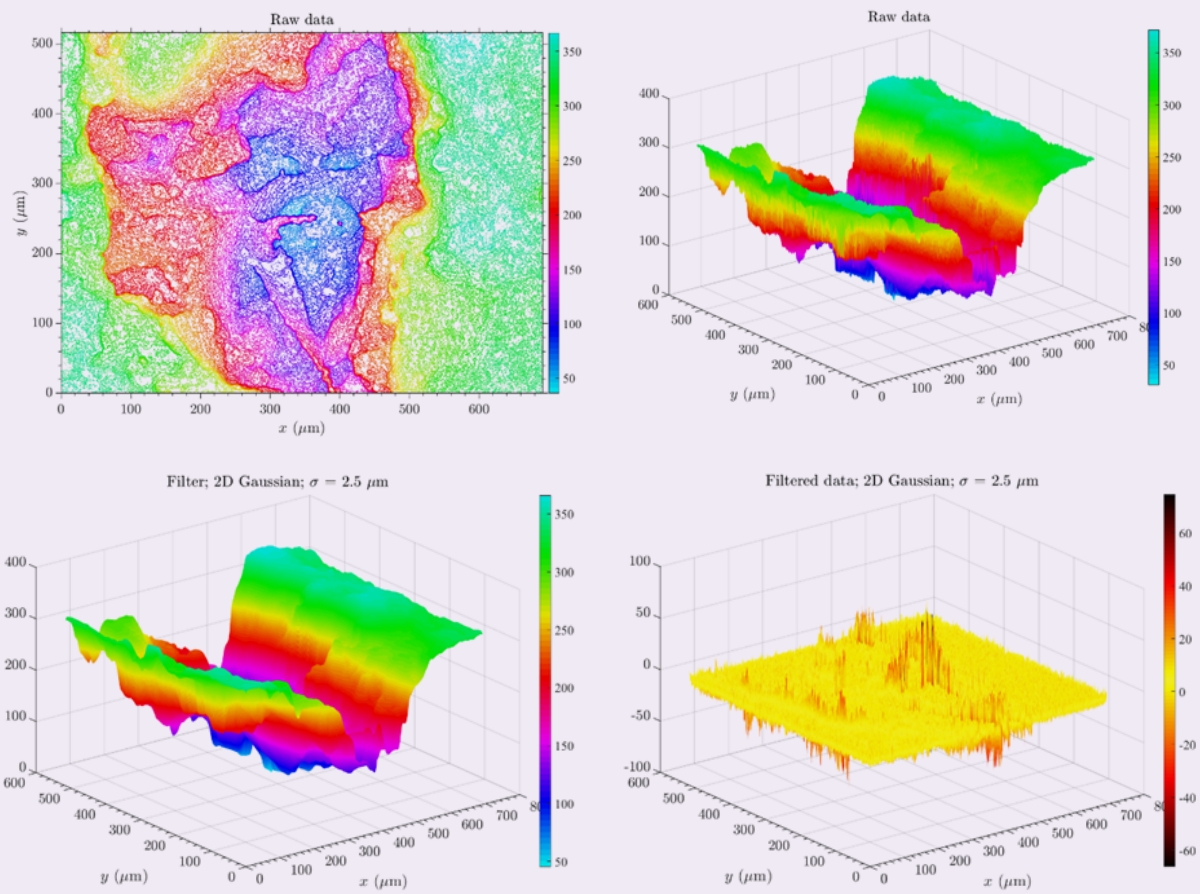

Fig. 6 *Top panel: The effects of the z cutoff (z_{cut} red bars located at 75 — without de-spiking — 30, 20, and 10 μm) on the surface roughness feature height distribution, P(z). The bottom panel shows the corresponding filtered images.*

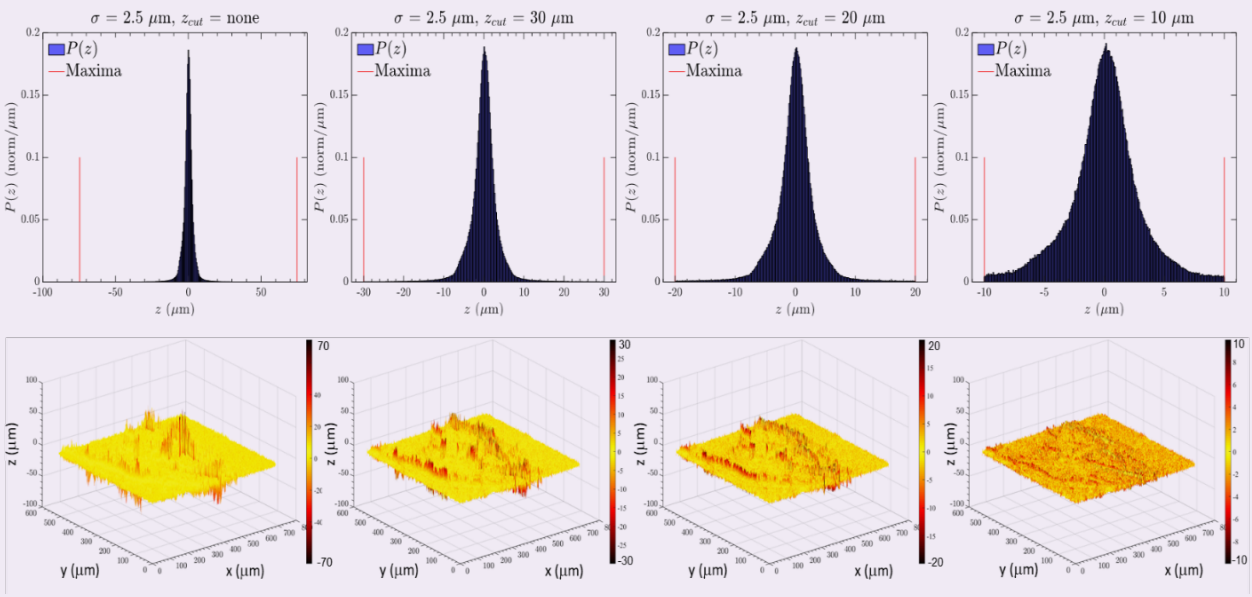

measured surface roughness *Sr* and *Sdr* is < 10%, therefore, the methods used to measure and calculate surface roughness are considered robust.

2D Gaussian Filter Example

Figure 5 shows an example of the LSCM raw and filtered data. The top panel shows the raw data in different views; 2D map on the left and 3D cube on the right. In the bottom panel, the 2D Gaussian filter of $\sigma = 2.5$ μm is shown on the left (note that it looks very much similar to the top panel 3D cube raw data) and the filtered data on the right.

The filtered data shows spikes in the regions of the LSCM image where there are significant jumps in height, which will be investigated later in terms of the effect of de-spiking on the calculated roughness value.

Effect of De-Spiking on the Filtered Data

We investigate the sensitivity of de-spiking on surface roughness calculations. Figure 6 shows the cutoffs, z_{cut}, used for de-spiking the raw data and the corresponding filtered roughness data. The calculated roughness parameters for a range of cutoffs are shown in Fig. 7. The spikes that are removed are not used in the roughness calculation.

From Fig. 6, the height distribution of the filtered image, *P(z)*, is plotted with cutoff values from $z_{cut} = 75$ μm, the maximum value, meaning that no data was removed for surface roughness calculation; $z_{cut} = 30$ μm, all the *z* values larger than 30 μm were removed from the surface roughness calculation; $z_{cut} = 20$ μm, all the *z* values larger than 20 μm were removed from the surface roughness calculation; and so on. The results in Fig. 7 show that *Sa* and *Sdq* values are the most affected by de-spiking, while *Sr* and *Sdr* are the most

Fig. 7 *The effect of de-spiking cutoff, z_{cut}, on the surface roughness parameters.*

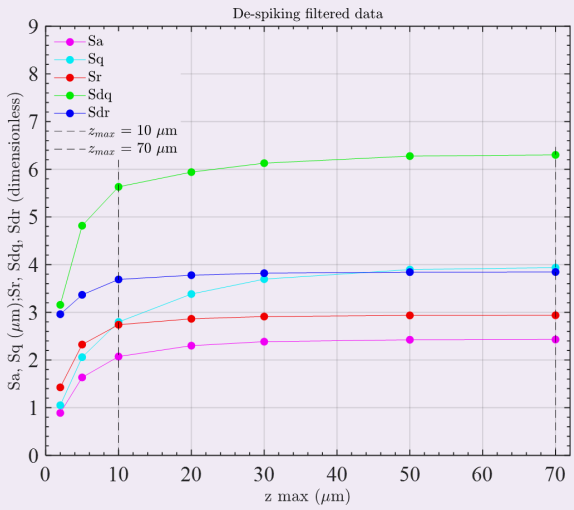

robust against de-spiking, above $z_{cut} = 10$ μm.

Table 2 lists the ratios of the surface roughness parameters for $z_{cut} = 10$ μm over $z_{cut} = 75$ μm (without de-spiking). The process of de-spiking affects the measured values of the surface roughness *Sr* and *Sdr* by less than 10%, therefore, the results are considered robust.

Directional Properties of LSCM Surface Roughness

Sr Dependency on Analysis Direction

Figure 8 is an example of the *Sr* histogram, revealing

Table 2 *The ratio of roughness parameters at z_{cut} = 10 μm over z_{cut} = 75 μm (without de-spiking).*

Roughness	Sa	Sq	Sr	Sdq	Sdr
z_{10}/z_{70}	0.85	0.71	0.93	0.89	0.96

whether the studied sample has a uniform or heterogeneous surface roughness.

From Fig. 8, the Guelph dolomite, the LSCM image shows two distinct areas. When the *Sr* is calculated along the *x*-axis (one *Sr* value corresponds to each point along the *y*-axis), Sr_0 (Eqn. 12), the *Sr* histogram shows one peak. When *Sr* is calculated along the *y*-axis (one *Sr* value corresponds to each point along the *x*-axis), Sr_{90} (Eqn. 13), the *Sr* histogram shows two peaks, corresponding to the two distinct regions in the LSCM image. The average values for Sr_0 and Sr_{90} are very close, with the slight difference likely due to data processing. During the filtering operation, a few data points at the edges of the image are removed, therefore, slightly different data points are included when the *Sr* is calculated along the *x*-axis compared to along the *y*-axis.

This directional dependency of *Sr* can be used to reveal heterogeneities in the surface roughness, and demonstrate that 2D areal surface roughness characterization is more representative of the solid surface than the 1D measurement, i.e., the *Sdr* roughness is independent on the angle, and therefore more robust to implement and straightforward to use for commercial applications.

$$Sr_0 = \frac{1}{N}\sum_{j=1}^{N} S_r(y_j) = \frac{1}{N^2}\sum_y \sum_x \left|\frac{\partial z}{\partial x}\right| \quad (12)$$

$$Sr_{90} = \frac{1}{N}\sum_{i=1}^{N} S_r(x_i) = \frac{1}{N^2}\sum_x \sum_y \left|\frac{\partial z}{\partial y}\right| \quad (13)$$

1D *Sr* vs. 2D *Sdr* Roughness Measurements

In this study, LSCM surface images were acquired on 29 samples, and the 1D *Sr* and 2D *Sdr* roughness were calculated. The results are summarized in Table 3 and cross plotted in Fig. 9. An excellent correlation with a correlation coefficient $R^2 = 0.998$ is observed between 1D *Sr* and 2D *Sdr*:

$$Sdr \approx 1.65Sr - 0.81 \quad (\text{for } Sdr > 2) \quad (14)$$

To better understand the relationship between the 1D *Sr* and 2D *Sdr*, Eqns. 15 and 16 can be derived from Eqn. 8, in the limits of very small (Eqn. 15) and large (Eqn. 16) height gradients:

$$Sdr \to \frac{1}{N^2}\sum_y \sum_x \left(\frac{1}{2}\left(\frac{\partial z}{\partial x}\right)^2 + \frac{1}{2}\left(\frac{\partial z}{\partial y}\right)^2\right) \approx \frac{1}{N^2}\sum_y \sum_x \left(\frac{\partial z}{\partial x}\right)^2 \ll Sr \ (\ll 1) \quad (15)$$

$$Sdr \to \frac{1}{N^2}\sum_y \sum_x \sqrt{\left(\frac{\partial z}{\partial x}\right)^2 + \left(\frac{\partial z}{\partial y}\right)^2} \approx \frac{1}{N^2}\sum_y \sum_x \sqrt{2\left(\frac{\partial z}{\partial x}\right)^2} \approx \sqrt{2}\,Sr \ (\gg 1) \quad (16)$$

Fig. 8 *Histograms of the 1D Sr; along the x-axis (color red Sr_0) and y-axis (color blue Sr_{90}). While the means are close (1.48 vs. 1.56), the distributions are different and directional. The x-axis direction averages over two regions with different roughness while the y-axis direction picks up roughness heterogeneity. Note that the directionless 2D Sdr = 1.70.*

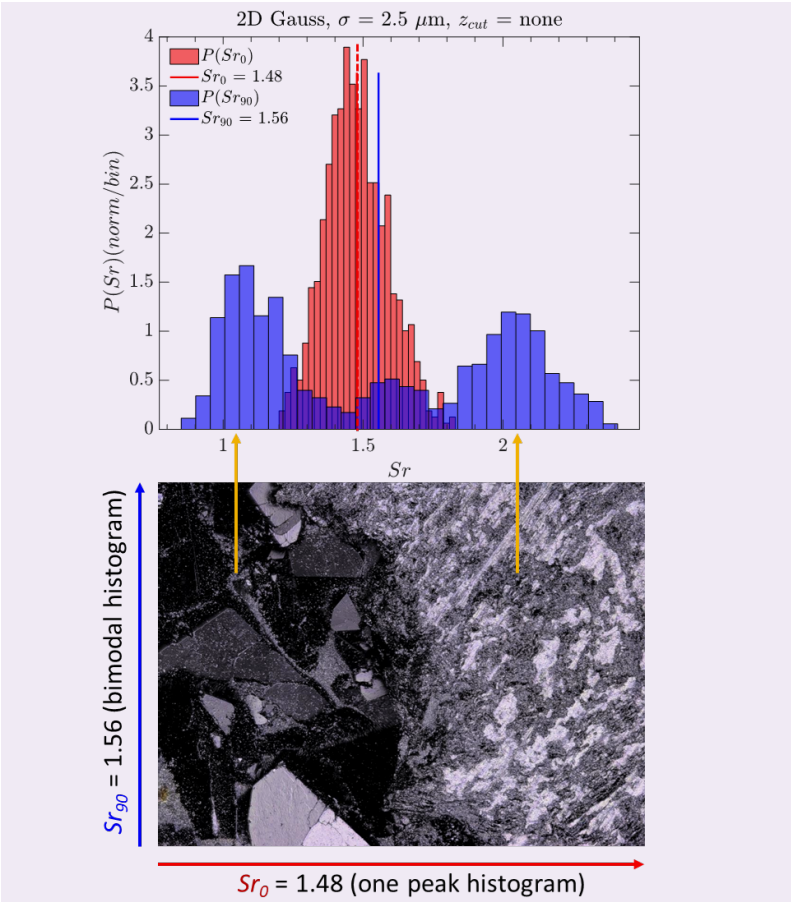

With Eqns. 14, 15, and 16, the following can be summarized:

- Both the 1D *Sr* and 2D *Sdr* methods are valid and interchangeable, with conversion factors as shown in Eqn. 14.
- The 2D *Sdr* has a wider dynamic range (from about 2 to 5) than the 1D *Sr*, (from about 2 to 3.5), therefore is more sensitive.
- The values of the 2D *Sdr* is higher than that of the 1D *Sr*, due to the way these parameters are defined and calculated.
- The two roughness expressions are linear for large values *Sdr*, *Sr* > 1 (Eqn. 16); however, they will curve toward the origin at low *Sdr*, *Sr* < 1, where Eqn. 15 predicts the parabolic curvature, e.g., $Sdr \propto Sr^2$.
- The 1D *Sr* is the mean of *Sr* histograms calculated in 1D, Eqn. 7. Note that for heterogeneous LSCM images, the *Sr* value depends on the direction along

Table 3 *The roughness parameters* Sr *and* Sdr *for various samples.*

Sample	*Sr*	*Sdr*	*Sdr/Sr*
ILS3	2.67	3.60	1.35
ILS4	2.89	3.97	1.37
ILS4A	2.93	4.03	1.38
DPink	2.63	3.51	1.33
U73	2.93	4.04	1.38
U20	3.36	4.71	1.40
U52	2.75	3.73	1.36
U86	2.78	3.78	1.36
U68	3.03	4.17	1.38
U80	2.47	3.26	1.32
U19	3.31	4.64	1.40
U159	3.07	4.25	1.38
H200	3.20	4.46	1.39
H4	2.02	2.57	1.27
H49	1.90	2.26	1.19
H12	2.36	3.01	1.28
H27A	2.45	3.22	1.31
H27B	3.57	5.04	1.41
A332166	2.95	4.01	1.36
A332275	3.15	4.32	1.37
U105137	3.14	4.33	1.38
U105146	2.92	3.98	1.36
U67054	2.52	3.35	1.33
U670113	3.22	4.51	1.40
U670181	2.91	4.00	1.37
U670224	2.88	3.96	1.38
Y21	2.44	3.21	1.32
Y28	2.57	3.4	1.32
Y29	2.45	3.21	1.31
Average	2.81	3.81	1.35

which the calculation is done first.

- Assuming large gradients (Eqn. 16) and no directional heterogeneity, the 2D *Sdr* is expected to be about 41% (factor $\sqrt{2}$) larger than *Sr*, i.e., *Sdr* ≈ 1.41 *Sr*. As the real sample contains a mixture of small and large gradients, the difference between the two will be less than 41%; such an average value of 1.35 for the samples in Table 3.

Fig. 9 *The 2D* Sdr *corelates well with the 1D* Sr.

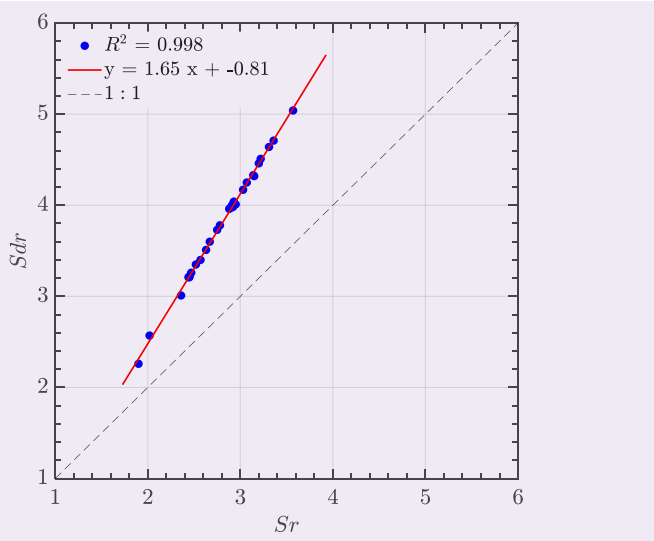

2D *Sdr* Roughness Values of Various Surfaces

An additional 17 LSCM surface roughness measurements were conducted, Fig. 10, and the 2D *Sdr* were calculated on various surfaces, Table 4 and Fig. 11. The 2D *Sdr* varies from 0.21 (smooth acrylic paint) to 6.21 (rough rose petal), with an average of 2.92. The rocks fall in between; muddy limestones having the lowest *Sdr* and grainy limestones the highest.

Figure 12 shows the raw data and roughness profiling for samples of acrylic paint, Carbon Tan, and rose petal.

Effect of Surface Preparation on 2D *Sdr*

To test the potential effect of the surface preparation on the surface roughness, artificial surfaces of four rocks (Berea, Carbon Tan, Kentucky, and Parker sandstone) were prepared by sawing and by mechanical breaking. Five symmetrical areas on the rock surface were measured, as shown in the example in Fig. 13 for Berea sandstone. An overall *Sdr* is calculated.

Although the roughness histogram shows in-depth information about the roughness heterogeneity, possibly capturing the presence of different textures or differences between small and large pore surface roughness, when the main objective is comparing the roughness between different cores, the mean values from the five different locations, Table 5, are more practical.

The overall *Sr* histogram for the five locations and the mean values are shown for the sawed and broken Berea sandstone, Fig. 14, and Carbon Tan, Fig. 15. For the same sample, the mean value is similar for the surfaces created by sawing and breaking, Table 5, while the histogram for the broken case is slightly broader, i.e., the rock surfaces prepared by sawing and breaking do not show significant variations in surface roughness.

2D Surface Roughness on Cuttings

Two cores, the Parker sandstone and Carbon Tan, were crushed to generate cuttings that were separated by

Fig. 10 *The LSCM images for the additional various samples.*

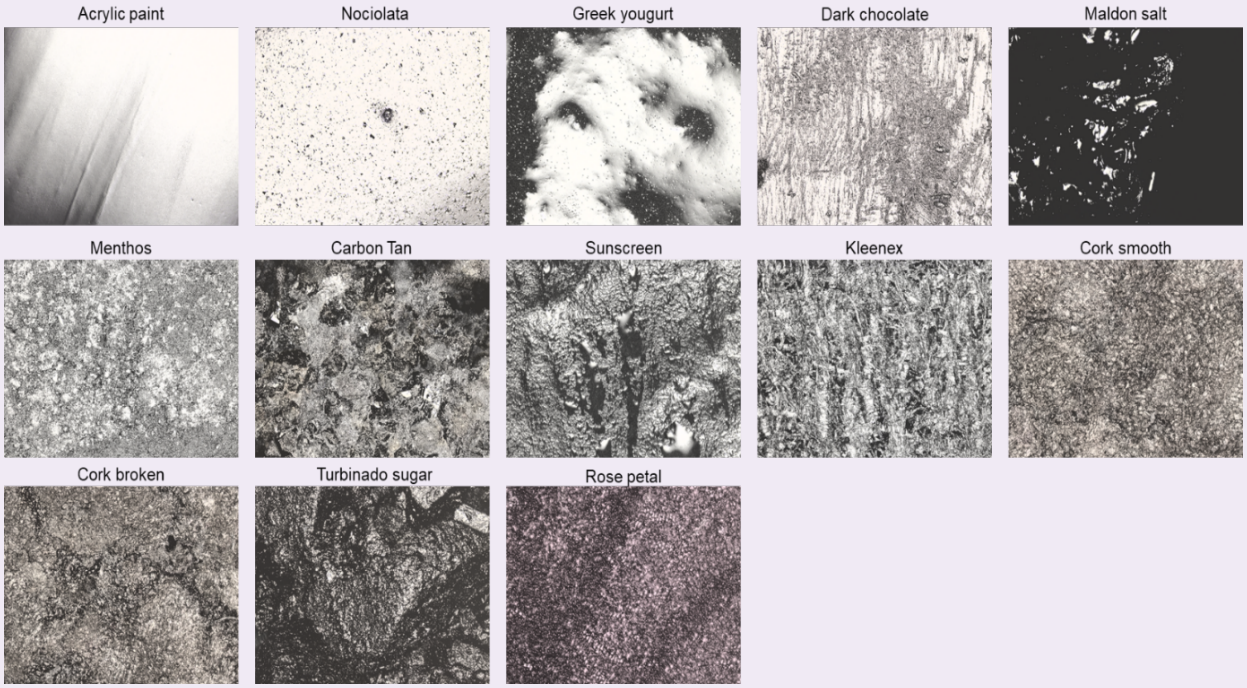

Table 4 *The roughness parameter* Sdr *for various samples. The entries in red correspond to rocks.*

	Sample	*Sdr*
1	Acrylic paint	0.21
2	Nociolata	0.38
3	Greek yogurt	1.08
4	Chocolate	1.3
5	Maldon salt	1.45
6	Menthos	1.51
7	Muddy limestone	2.77
8	Dolostone	2.81
9	Sunscreen	2.9
10	Kleenex	3.02
11	Y (mix dolomite and limestone)	3.27
12	Sandstone	3.44
13	Cork smooth	3.76
14	Grainy limestone	4.03
15	Cork broken	5.54
16	Turbinado sugar	5.91
17	Rose petal	6.21
	Average	2.92

size: < 0.8 mm, 0.8 mm to 2 mm, 2 mm to 3.35 mm, 3.35 mm to 4.75 mm, and > 4.75 mm. LSCM images were acquired on these cutting samples; five images for each cuttings size, Fig. 16. The cuttings were fixed with playdough to prevent cutting movement under the microscope and to set the measured surface as horizontal as possible.

The data shows that the surface roughness measured from the cuttings, Table 6, is comparable with that measured from the plugs, Table 5, demonstrating that cuttings can be used for measuring the LSCM surface roughness, as long as the cuttings size is larger than the roughness features and the FOV (FOV = 1 mm × 1.4 mm).

Figure 17 shows the *Sr* histograms and its mean value for the various cutting sizes.

Pore Size Distribution

Roughness-Free Pore Size Distribution

The workflows for obtaining surface roughness and roughness-free pore size distribution using LSCM, D-T_2, or micro-CT methods are shown in Fig. 18, along with their pros and cons, Table 7.

Surface Relaxivity Corrected for Surface Roughness

The surface relaxivity (ρ), which depends on surface roughness S, was introduced by Nordin and Knight (2016)[2]. Based on simple geometry, they show that ρ is defined as:

$$\rho = \rho_{intrinsic}(1 + 2S) \quad (17)$$

Fig. 11 *The measured roughness parameter* Sdr *for various samples. The entries in red correspond to rocks.*

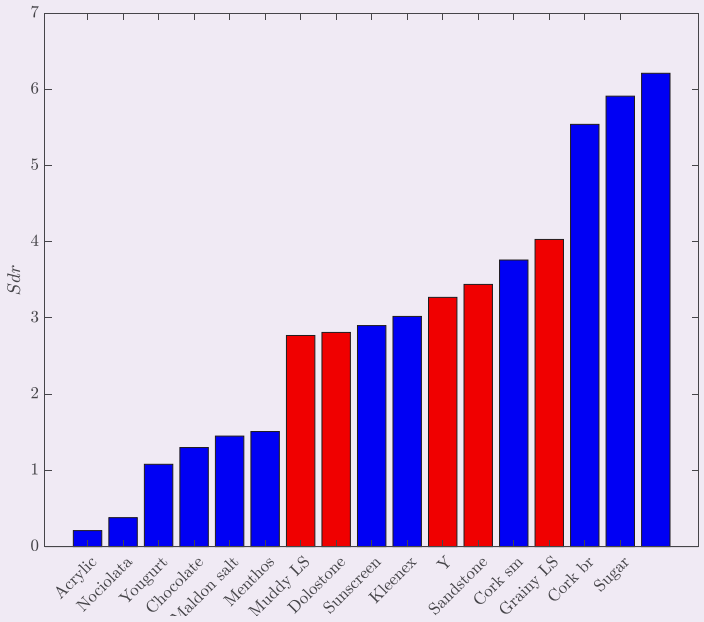

where it is assumed that the surface area of all pores is covered by roughness.

The intrinsic surface relaxivity, which parameterizes the strength of the interaction between fluid nuclear spins and the smooth pore wall, is mineralogy and surface chemistry dependent, and can be derived from the BET gas adsorption method. Then, the roughness in Eqn. 17 can be estimated from 1D *Sr*, or 2D *Sdr*, and Eqn. 17 becomes:

$$\rho_{Sr} = \rho_{BET}(1 + 2Sr) \quad 18$$

$$\rho_{Sdr} = \rho_{BET}(1 + 2Sdr) \quad 19$$

Excellent correlation with $R^2 = 0.996$ is observed when cross plotting ρ_{Sr} and ρ_{Sdr}:

$$\rho_{Sdr} \approx 1.32\rho_{Sr} - 0.16 \quad (\text{for } \rho_{Sdr} > 5\ \mu\text{m/s}) \quad 20$$

which shows that both methods are valid and can be used interchangeably, though the data indicates that ρ_{Sdr} is slightly more sensitive than ρ_{Sr}, Fig. 19.

Pore Size from D-T_2

Another method for estimating the surface relaxivity is from D-T_2 maps of the fully saturated brine cores. Mitra et al. (1992)[7] showed that at short diffusion times, t_D, the diffusion coefficient, $D(t_D)$, deviates from the bulk molecular diffusion coefficient of the fluid, D_0, by a term proportional to the surface-to-pore volume ratio, S/V_p. This is known as restricted diffusion.

At long times, when the diffusion length is large compared with the length-scale of the pore space, the spins probe the connectivity of the pore space, and the diffusion coefficient approaches the diffusion coefficient in the tortuosity limit given by:

$$\tau = \phi^{1-m} \quad 21$$

where m is the Archie cementation exponent, and the $D(t_D)$ tends to approach D_∞. The $D(t_D)$ in the tortuosity limit as defined by Eqn. 21 is:

$$D(t_D) \rightarrow D_\infty = \frac{D_0}{\tau} \quad 22$$

Latour et al. (1993)[8] introduced an expression for $D(t_D)$ that interpolates between the short-time behavior

Fig. 12 *The raw LSCM data (left), with one* z *profile from the LSCM image. The roughness data (right) after applying a Gaussian filter. Data has been shifted along the* y*-axis by 50* μm *(Carbon Tan) and 100* μm *(rose petal), for clarity. Samples are acrylic paint (smoothest), Carbon Tan, and rose petal (roughness).*

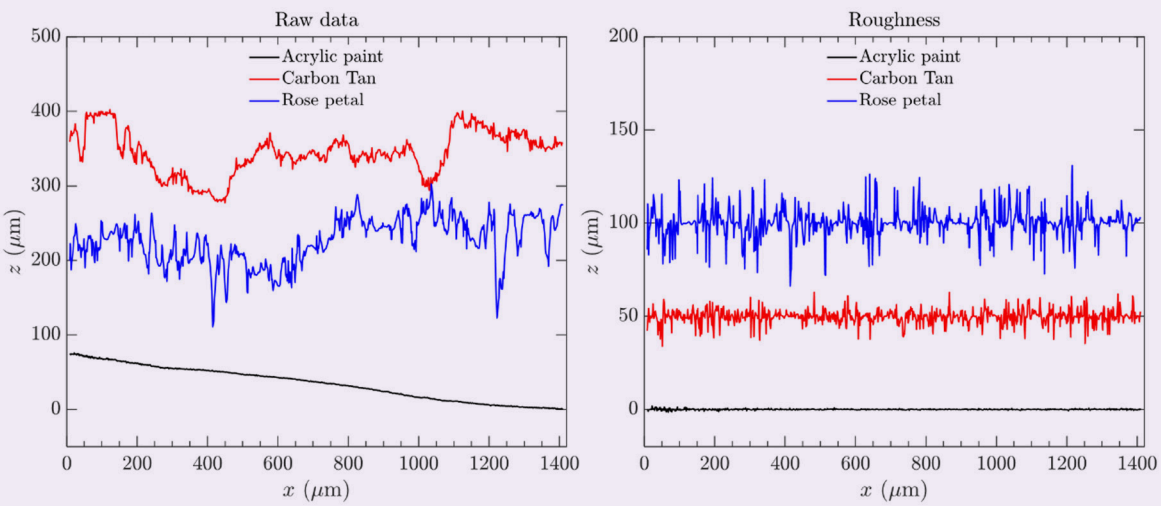

Fig. 13 *Five LSCM images acquired from five areas on two surfaces of the same rock (Berea sandstone). The top five are the sawed surface and the corresponding* Sr *distributions. The bottom five are the broken surface and their* Sr *distributions.*

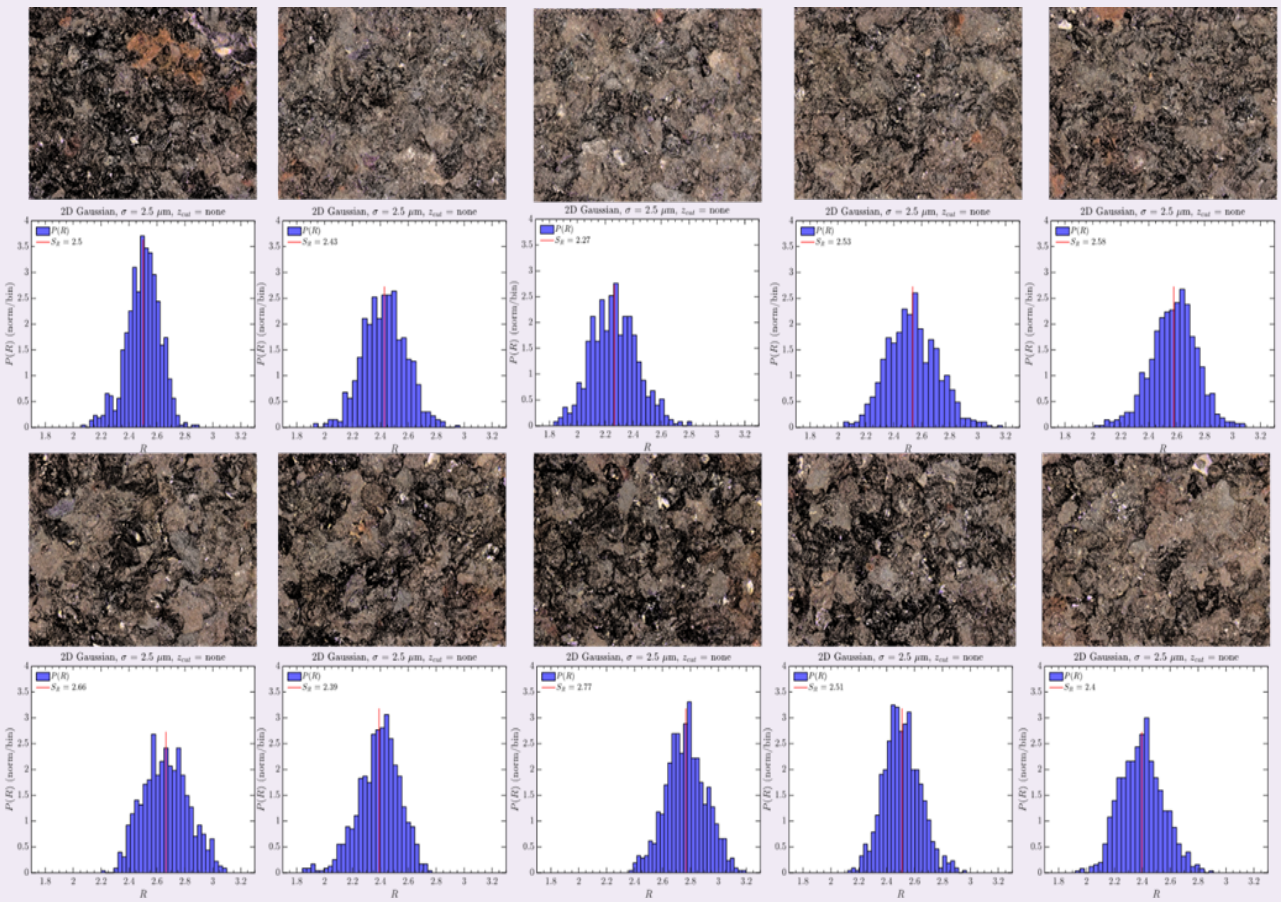

Table 5 *The effect of surface preparation on* Sdr *using five core samples of four rock types.*

Area #	Berea Sandstone		Carbon Tan			Kentucky Sandstone		Parker Sandstone	
	Sdr **sawed**	***Sdr*** **broken**	***Sdr*** **sawed (core #1)**	***Sdr*** **sawed (core #2)**	***Sdr*** **broken**	***Sdr*** **sawed**	***Sdr*** **broken**	***Sdr*** **sawed**	***Sdr*** **broken**
1	3.28	3.58	3.51	3.32	3.08	3.40	3.28	2.86	2.45
2	3.18	3.05	3.24	3.16	3.45	2.86	3.18	3.20	2.83
3	2.92	3.58	3.14	3.22	2.88	3.29	3.32	3.63	2.53
4	3.35	3.31	2.73	3.49	3.31	—	3.09	3.05	3.09
5	3.43	3.12	3.35	2.96	3.43	—	3.34	2.69	2.69
Average	**3.23**	**3.33**	**3.19**	**3.23**	**3.23**	**3.18**	**3.24**	**3.09**	**2.72**

Fig. 14 *Berea sandstone: The overall* Sr *histogram and its mean value for the sawed (left) and broken (right) surfaces. The histogram for the broken surface is slightly broader, but the mean* Sr *is similar as in the sawed surface.*

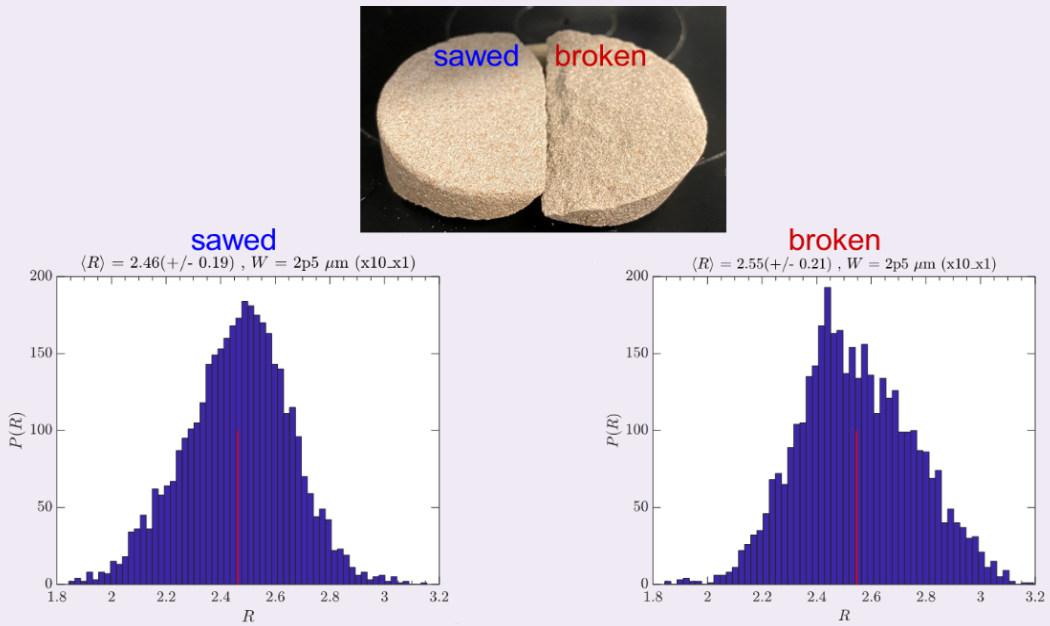

Fig. 15 *Carbon Tan: The overall* Sr *histogram and the mean value for the sawed (left) and broken (right) surfaces. The histogram for the broken surface is slightly broader, but the mean* Sr *is similar as in the sawed surface.*

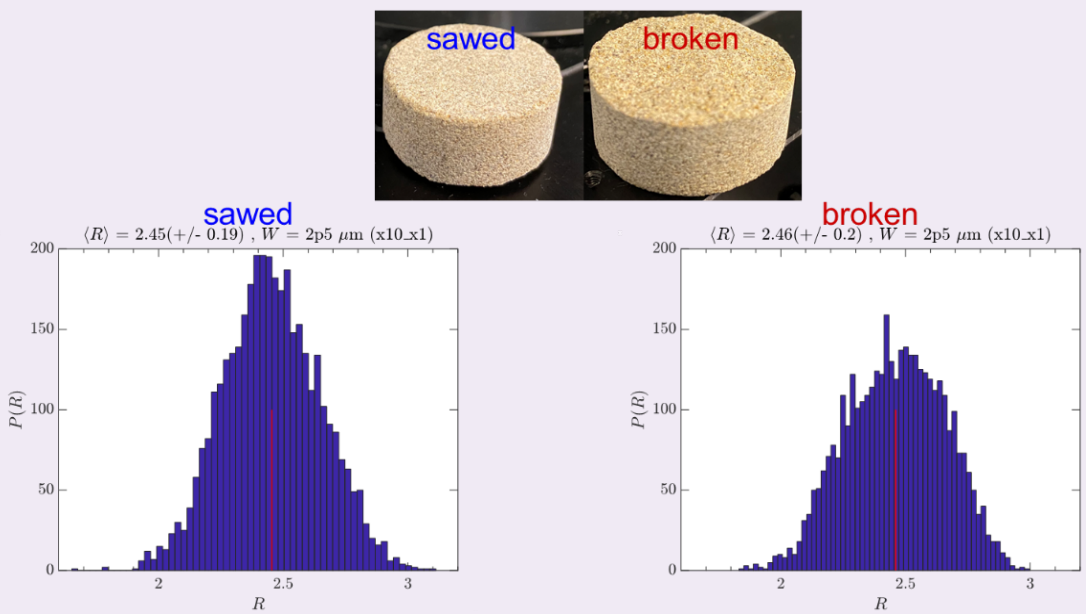

and the long-time asymptotic value of $1/\tau$. The time dependent $D(t_D)$ for short times and long times are connected using the Padé approximation[9], and the D-T_2 based surface relaxivity, ρ_{DT2}, can then be estimated[10]:

$$\frac{D(T_2)}{D_0} = 1 - \gamma \frac{\alpha L_D}{\alpha L_D + \gamma} \quad (23)$$

$$\gamma = 1 - \frac{D_\infty}{D_0} = 1 - \frac{1}{\tau} = 1 - \phi^{m-1} \quad (24)$$

$$L_D = \sqrt{D_0 t_D}, \quad (25)$$

Fig. 16 *The cuttings of different sizes are fixed in playdough to prevent movement during LSCM measurements. The crosses indicate the areas where the images were acquired.*

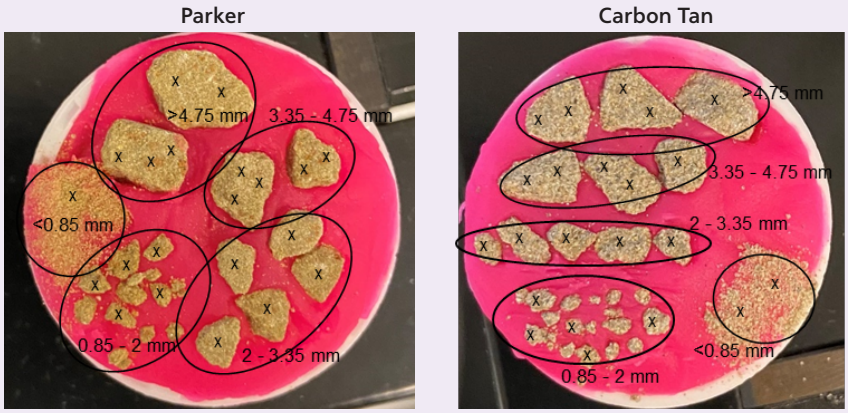

Table 6 *The* Sdr *roughness for the Parker sandstone and Carbon Tan for the five locations for each cutting size.*

Area #	Parker Sandstone Cuttings (*Sdr*)					Carbon Tan Cuttings (*Sdr*)				
	> 4.75 mm	3.35 to 4.75 mm	2 to 3.35 mm	0.85 to 2 mm	< 0.85 mm	> 4.75 mm	3.35 to 4.75 mm	2 to 3.35 mm	0.85 to 2 mm	< 0.85 mm
1	3.28	—	3.35	3.33	3.30	3.23	2.71	3.15	2.98	3.22
2	3.43	3.22	2.81	3.67	—	3.73	3.08	3.81	3.49	3.64
3	2.91	3.03	2.90	4.03	—	1.80	3.64	3.59	3.24	—
4	2.79	3.09	3.07	2.49	—	4.44	3.41	3.35	2.89	—
5	3.35	3.00	3.26	3.94	—	3.26	3.43	3.05	3.77	—
Average	**3.15**	**3.12**	**3.08**	**3.49**	**—**	**3.31**	**3.25**	**3.39**	**3.27**	**—**

Fig. 17 *The* Sr *histograms for Parker (top row) and Carbon Tan (bottom row) sandstone from five locations for each of the five cuttings sizes. The Carbon Tan histogram reveals some roughness heterogeneity.*

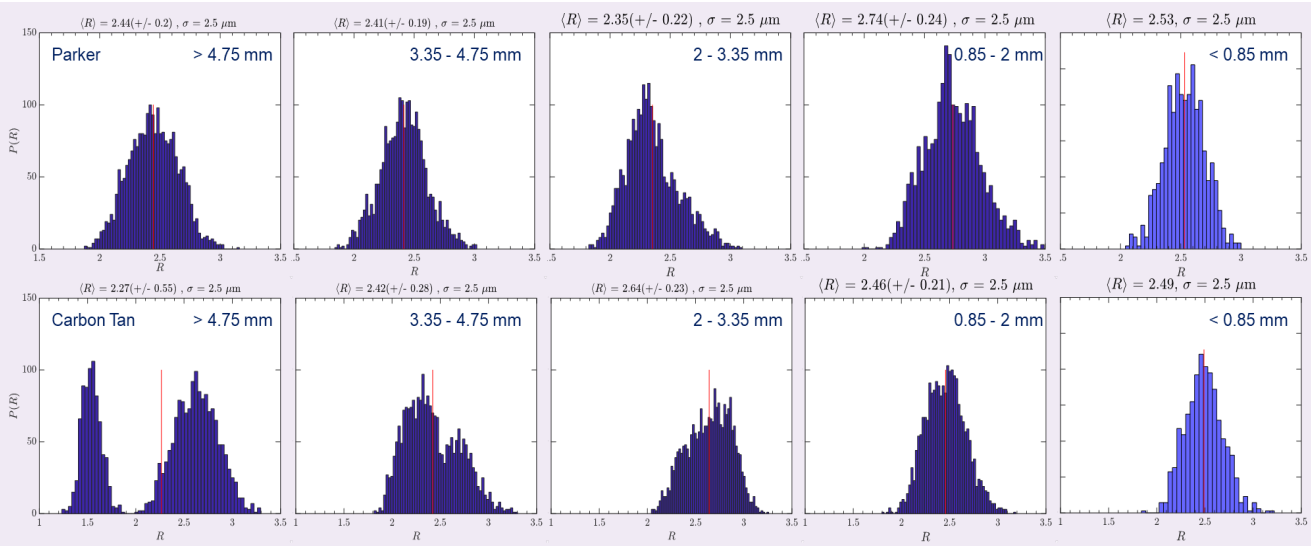

Fig. 18 *The surface roughness measurement workflow.*

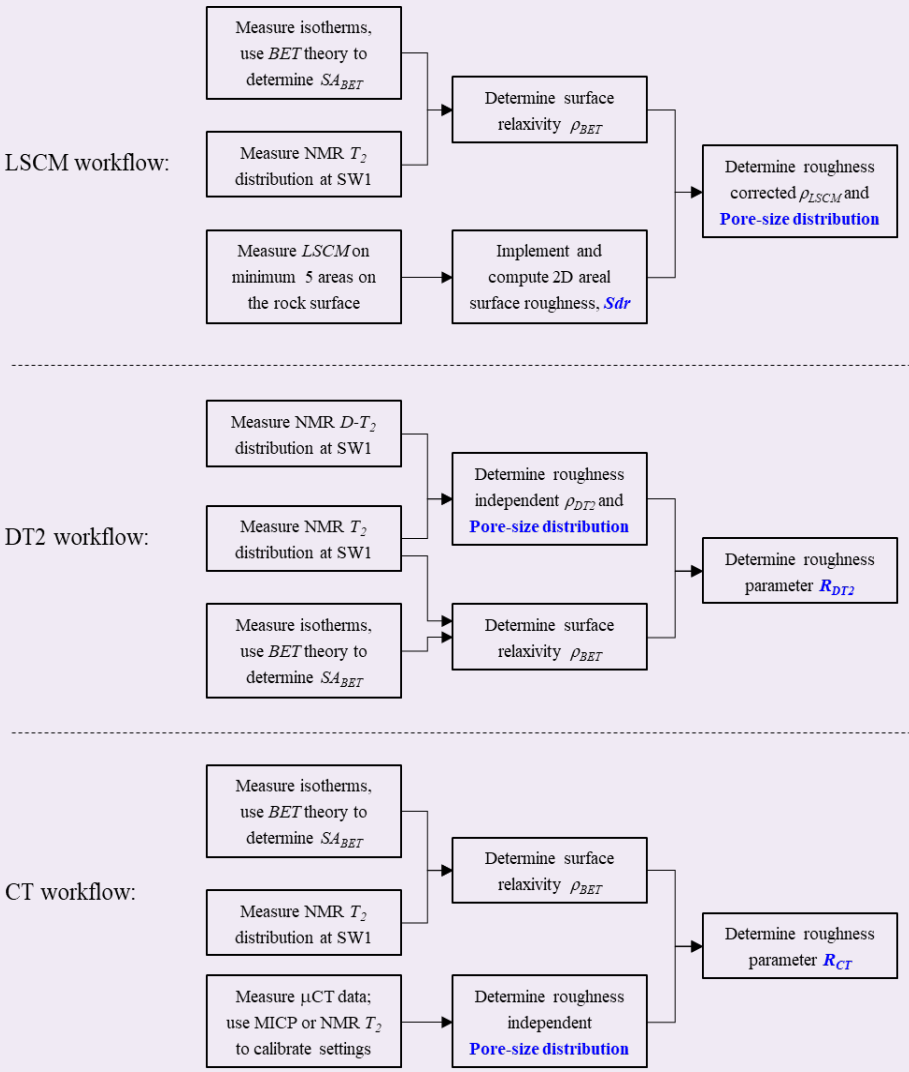

$$\alpha = \frac{4}{9\sqrt{\pi}} \frac{1}{T_{2S}\rho_{DT_2}} \quad (26)$$

$$\frac{1}{T_2} = \frac{1}{T_{2S}} + \frac{1}{T_{2B}} \quad (27)$$

D_0 is the bulk diffusion coefficient of the fluid, T_{2B} is the bulk relaxation of the fluid, D_∞ is $D(t_D)$ in the tortuosity limit as defined by Eqn. 21, and t_D the diffusion time, i.e., the time the molecules are allowed to diffuse.

The D-T_2 was measured for 11 fully saturated brine cores and the maps are shown in Fig. 20. The Padé D-T_2 correlation line (Eqn. 23) is plotted for three different values of the surface relaxivity, ρ_{DT2}, and the value that gives the best fit to the D-T_2 distribution, i.e., that goes through the peak of the 2D distribution, is shown with a blue dotted line.

Two caveats exist: (1) The tortuosity limit used in the Padé fit at short T_2 has to be measured from another technique, such as resistivity, and (2) This method for estimating the surface relaxivity only works when there is sufficient restriction. Note that the ρ_{DT2} values for the three Y samples (21, 28, and 29) have very different values, 12.76, 5.92, and 2.70 μm/s. The D-T_2 maps show that there is not much restriction, the peak of the distribution is very close to the bulk water diffusion line, and therefore, the estimation of surface relaxivity from D-T_2 is not very accurate.

In this study, it was assumed that $m = 2$ for all the cores. The surface relaxivity from D-T_2, ρ_{DT2}, along with the surface relaxivity from BET, ρ_{BET}, and LSCM, ρ_{Sr} and ρ_{Sdr}, are shown in Table 8. The ρ_{DT2}, ρ_{Sr} and ρ_{Sdr} values are higher than ρ_{BET} since they include the surface roughness effect.

As shown in Table 9, the average ratio between ρ_{Sdr} and ρ_{DT2} for the 11 tests is 1.84, due to the differences in methods used and uncertainties of data processing

Table 7 *The various methods for surface roughness measurements and their pros and cons.*

Surface Roughness	Pros	Cons
LSCM (0.2 to 2 µm)	Direct measurement. Easy to extract from LSCM image. Distinguishes between different facies, distribution of values, for 1D analysis. Insensitive to the presence of clays.	Surface measurement, therefore, might not be representative. For heterogeneous samples, cut in sections and measure multiple locations.
D-T_2 (~10 µm for water)	Bulk value, representative for entire sample.	Only works when diffusion is sufficiently restricted (small pores). Single value for the entire pore space; could distinguish between small and large pores. The tortuosity limit in the Padé fit at short T_2 must be measured from another technique, such as resistivity. Need ρ_{BET} to calculate R_{DT2}. Sensitive to the presence of clays due to ρ_{BET}.
micro-CT (~1 µm)	Can see the roughness.	Small FOV, not representative. Need T_2 to calculate ρ_{CT} and ρ_{BET} to get R_{CT}. Sensitive to the presence of clays due to ρ_{BET} (when clays are coated with bitumen, this is not an issue[6]). Expensive and time-consuming.
FIB-SEM (~1 nm)	Can see the roughness.	Extremely small FOV, not representative. Very expensive and time-consuming.

parameters, while the average ratio between ρ_{Sdr} and ρ_{BET} is significant, 8.17, mainly due to the consideration effect of the surface roughness.

Comparison of Pore Size Distributions

Assuming that the rock consists of disconnected pores and that the relaxation is in the fast diffusion limit, which means that the molecule bounces off the surface many times before relaxing, the surface relaxation then depends on the surface-to-volume ratio and surface relaxivity parameter, ρ_2, which is a function of fluid-surface interactions:

$$\frac{1}{T_2} = \frac{1}{T_{2S}} = \rho_2 \frac{A}{V_p} \quad (28)$$

where T_{2S} is the T_2 component due to surface relaxation (the bulk relaxation can be neglected here) and ρ_2 is the surface relaxivity. The geometric term A/V_p is:

$$\frac{A}{V_p} = \frac{1-\phi}{\phi}\frac{A}{V_g} \quad (29)$$

where ϕ is the porosity and V_g is the volume of the solid grains.

If the pore structure can be modeled by smooth spherical bodies of diameter d, then the pore body size can be derived from NMR data as:

$$d = 6\frac{V_p}{A} = 6\rho_2 T_{2S} \quad (30)$$

Fig. 19 *The surface relaxivity derived using 2D* Sdr, ρ_{sdr} *corelates well with the surface relaxivity derived using 1D* Sr, ρ_{Sr}.

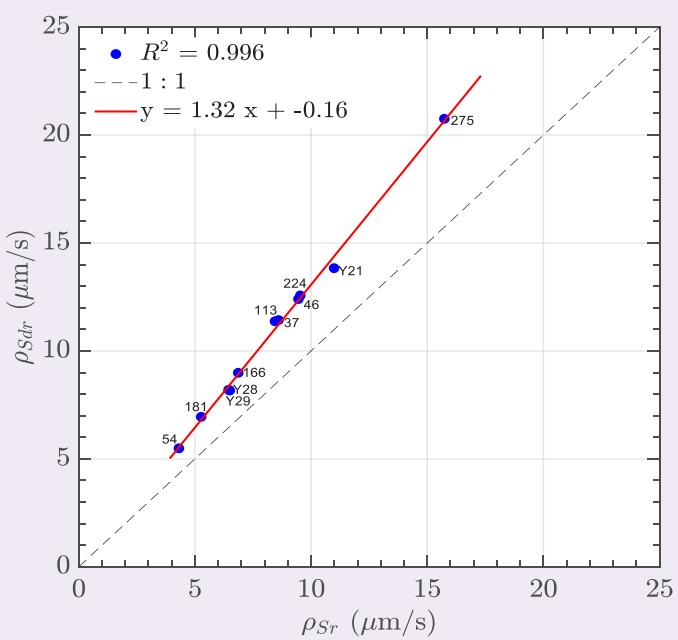

Fig. 20 *The D-T_2 maps for 11 fully saturated brine cores. Assuming m = 2, the Padé D-T_2 correlation line is plotted for three different values of the ρ_{DT2} and the best fit to the distribution is the dash blue line (blue value of ρ_{DT2}).*

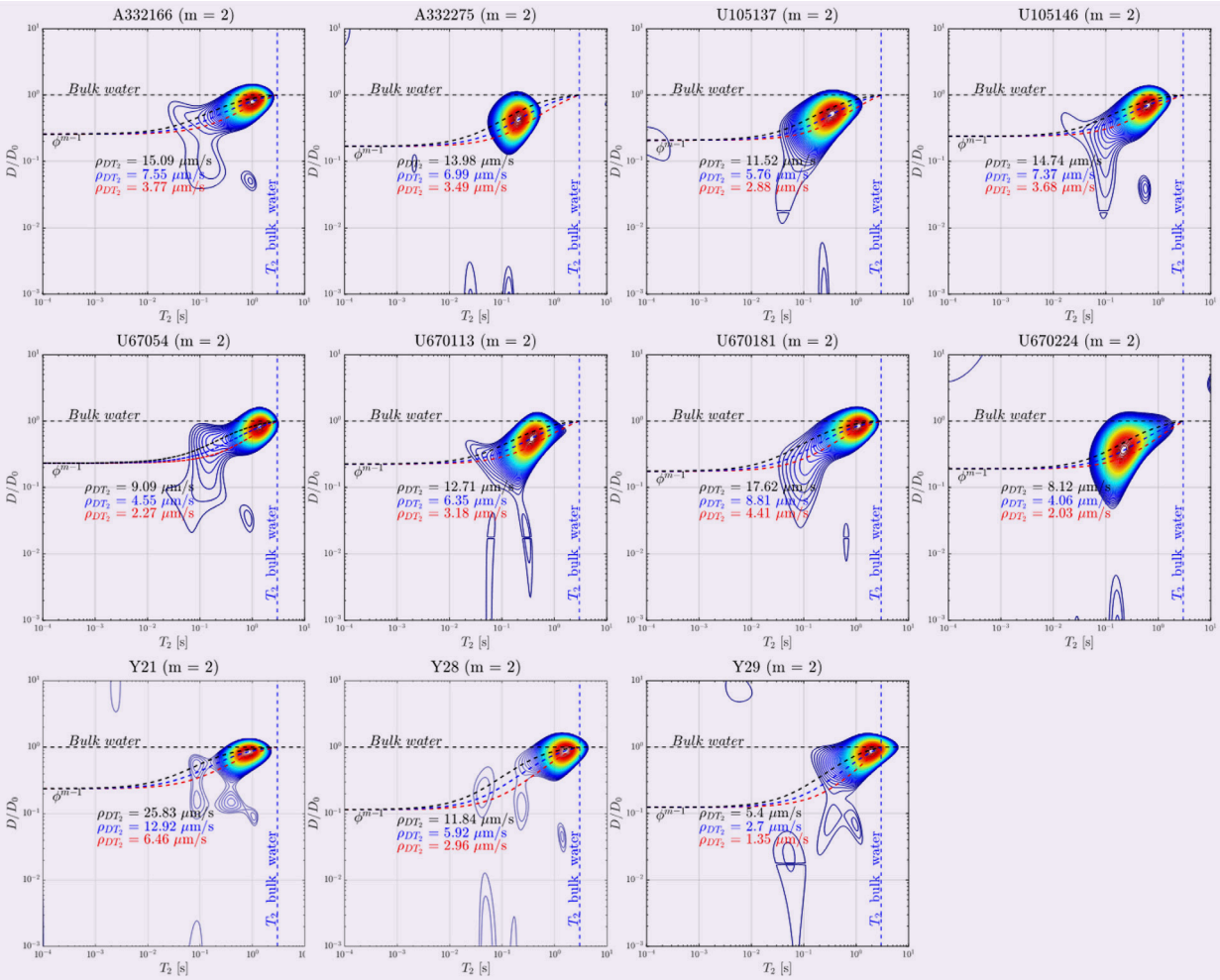

Table 8 *The surface relaxivities from the D-T_2 map, ρ_{DT2}, BET, ρ_{BET}, and LSCM, ρ_{Sr} and ρ_{Sdr}.*

Sample	ρ_{DT_2} (μm/s)	ρ_{BET} (μm/s)	ρ_{Sr} (μm/s)	ρ_{Sdr} (μm/s)
A332166	7.55	1.00	6.86	8.99
A332275	6.99	2.15	15.74	20.75
U105137	5.76	1.18	8.60	11.43
U105146	7.37	1.38	9.46	12.40
U67054	4.55	0.71	4.31	5.49
U670113	6.35	1.14	8.45	11.37
U670181	8.81	0.77	5.27	6.95
U670224	4.06	1.41	9.54	12.57
Y21	12.76	1.87	10.99	13.83
Y28	5.92	1.05	6.45	8.20
Y29	2.70	1.10	6.50	8.17

Table 9 *The ratio of surface relaxivities from the* D-T_2 *map,* ρ_{DT2}, *BET,* ρ_{BET}, *and LSCM,* ρ_{Sdr}.

Sample	ρ_{Sdr} / ρ_{DT_2}	ρ_{Sdr} / ρ_{BET}
A332166	1.19	8.99
A332275	2.97	9.65
U105137	1.98	9.69
U105146	1.68	8.99
U67054	1.21	7.73
U670113	1.79	9.97
U670181	0.79	9.03
U670224	3.1	8.91
Y21	1.08	7.40
Y28	1.39	7.81
Y29	3.03	7.43
Average	1.84	8.69

Using the surface relaxivity, ρ_2, from the standard BET, gas adsorption underestimates the NMR pore size due to surface roughness effects, Fig. 21.

Figure 22 shows the pore size distribution from NMR for 11 samples, using the surface relaxivity from BET, LSCM (*Sr* and *Sdr*) and *D*-T_2. The pore size distribution from ρ_{BET} (Eqn. 1) is much smaller, almost 10 times smaller (8.69, from Table 9), than the pore size distribution from *D*-T_2 and LSCM. The pore size distributions from *D*-T_2 and LSCM are in reasonable agreement (1.84, from Table 9) with each other, Fig. 23, except for three samples, U670224, A332275, and Y29, where the $d_{LM,Sdr} > 2\, d_{LM,DT2}$. Possible reasons for discrepancy are:

1. *D*-T_2 is a bulk measurement, while LSCM has access only to the exposed surface.
2. The LSCM surface roughness could be affected by the sample preparation.
3. In this study, it was assumed $m = 2$ for all the cores, which affects ρ_{DT2} in some cases. Ideally the tortuosity limit in the Padé fit at short T_2 should be measured by another technique, such as resistivity.

As noted before, one reason is that this method for estimating the surface roughness only works when there is sufficient restriction in *D*-T_2, and the Archie exponent, *m*, is known (for cases where ρ_{DT2} depends strongly on *m*).

Correlation with Permeability

One application of proper pore size characterization of porous media is to enhance the prediction of permeability using the modified Kozeny-Carman equation[11,12]:

$$K_{KC} = \frac{\phi\, d^2}{32\,\tau\, BTR^2} = \frac{\phi^m d^2}{32\, BTR^2} \quad (31)$$

Here we assume $m = 2$ and pore body-throat-ratio = 3, then the pore body diameter, *d*, is estimated from the surface relaxivity from *D*-T_2, d_{DT2}. The calculated Kozeny-Carman permeability is plotted against the measured gas permeability, K_{air}, for eight cores. The correlation obtained (Eqn. 32) is excellent with a correlation coefficient $R^2 = 0.982$, Fig. 24.

$$K_{KC} = 1.99 K_{air}^{0.7} \quad (32)$$

Validation Against Micro-CT Scan

One method for directly determining the pore size distribution in core samples is using micro-CT imaging. Two samples were selected, A332275 and Y21. Low resolution scans were acquired with 26.7 µm/voxel for A332275, and with 29.0 µm/voxel resolution

Fig. 21 *An illustration showing the surface roughness effect on the pore size estimation from NMR. Ignoring the surface roughness, the pore size is underestimated*[1].

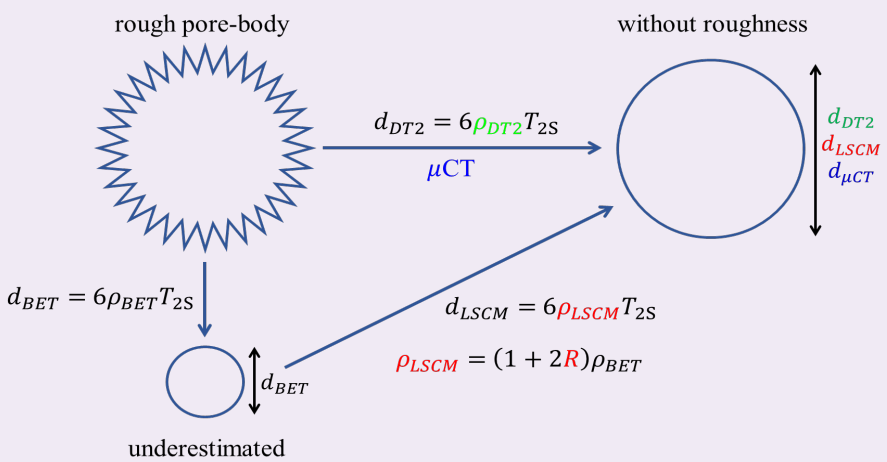

Fig. 22 *The pore size distribution from NMR with the surface relaxivity, ρ_2, from BET, $d_{BET} = 6\rho_{BET}T_{2S}$ (black dash), D-T_2, $d_{DT2} = 6\rho_{DT2}T_{2S}$ (green), LSCM Sr, $d_{Sr} = 6\rho_{Sr}T_{2S}$ (red), and Sdr, $d_{Sdr} = 6\rho_{Sdr}T_{2S}$ (red dash).*

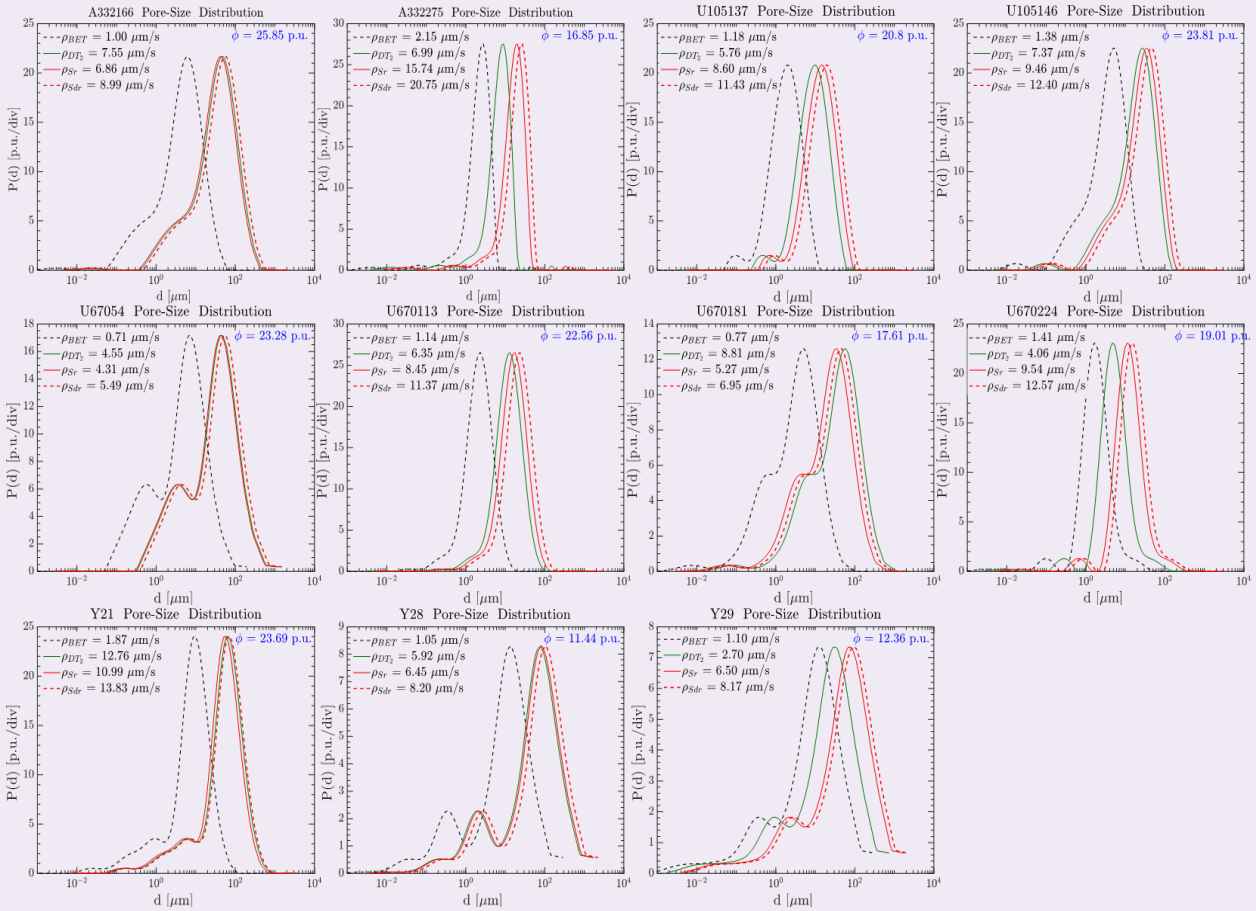

Fig. 23 *Left: Log mean of pore size distribution, dLM, from the LSCM (y-axis) vs. from D-T_2 (x-axis). Right: Log mean of pore size distribution, dLM, from the BET (y-axis) vs. from D-T_2 (x-axis).*

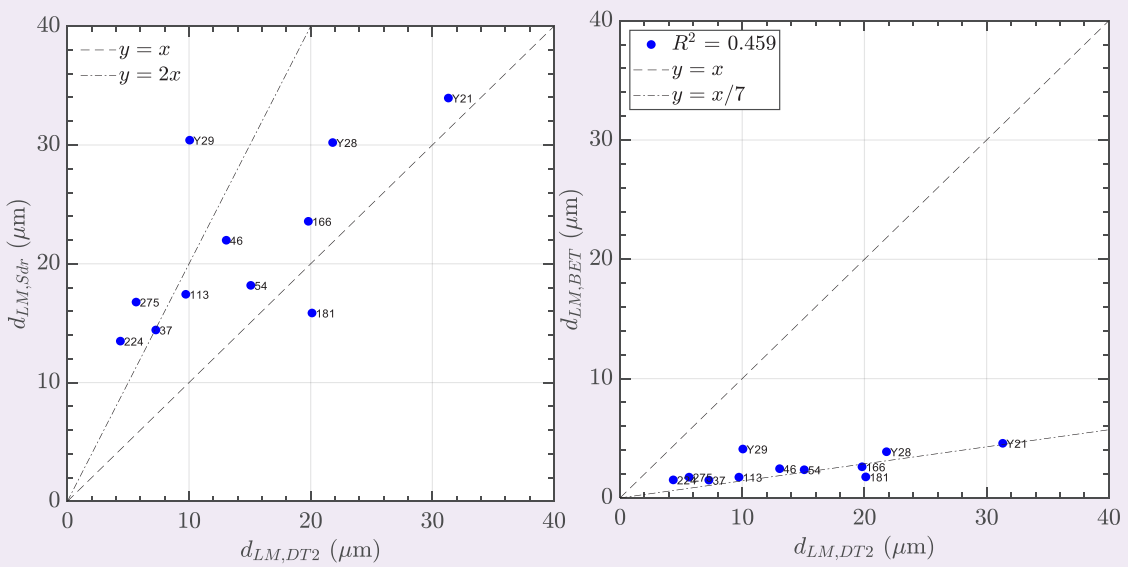

for Y21 sample. Note that at this low resolution direct measurement of small pores is not possible, while at the higher resolution, FOV becomes too small that large pores are lost. Consequently, a balanced approach was adopted and the focus of this study was to capture the big pores. Microporosity estimation requires higher resolution images such as using the nano-CT and/or 3D focused ion beam scanning electron microscopy (FIB SEM), which are not only more time-consuming, but also requires scaling.

The pore size distribution was extracted from micro-CT images using the hydraulic pore size distribution model[15]. In this model, the pore diameter is equal to the diameter of the largest sphere that can fill the pore space. Note that when using this model, small corners could be missed, therefore, the total pore space could be underestimated. As a quality check, the total porosity (resolved large pores and unresolved microporosity) calculated from micro-CT scans should be compared to the NMR porosity.

The typical workflow for determining pore size distribution from micro-CT images is to first measure the mercury injection capillary pressure (MICP) and use the results for selecting the optimal settings for the micro-CT measurement. The MICP is used as a quality check for the micro-CT pore size distribution.

The pore size distribution from the low resolution micro-CT is shown for A332275 in Fig. 25, and for Y21 in Fig. 26. In both examples, the upper end of the pore size distribution from NMR, using the LSCM roughness corrected surface relaxivity, is in good agreement with the pore size from the micro-CT.

The pore size distribution from NMR, using the D-T_2 surface relaxivity, is in good agreement with the pore size from the micro-CT for Y21, however, for A332275 it is about three times smaller. One possible reason is that for A332275, the surface relaxivity from D-T_2 depends strongly on m (assumed to be $m = 2$ throughout), while for Y21 it is almost independent on m.

Fig. 24 *The Kozeny-Carman permeability (y-axis) vs. the gas permeability (x-axis).*

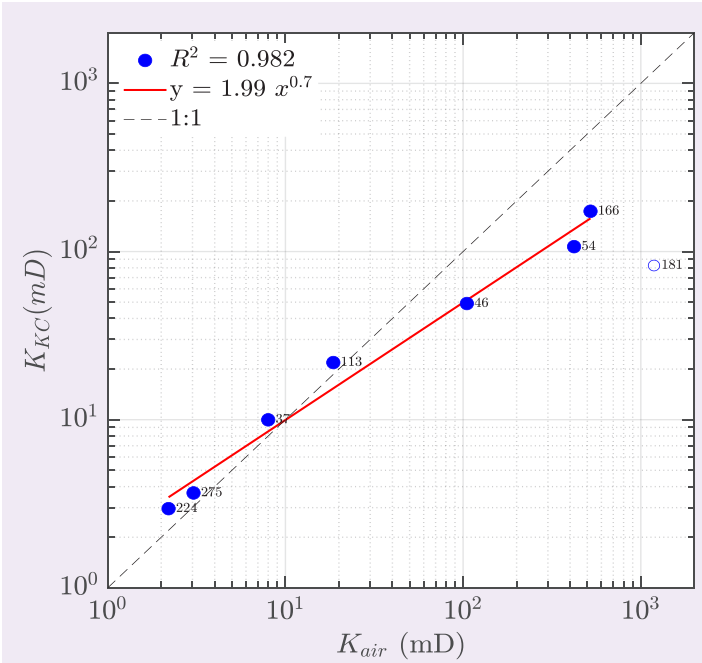

Fig. 25 *The effect of surface roughness on the surface relaxivity and pore size distribution for A332275.*

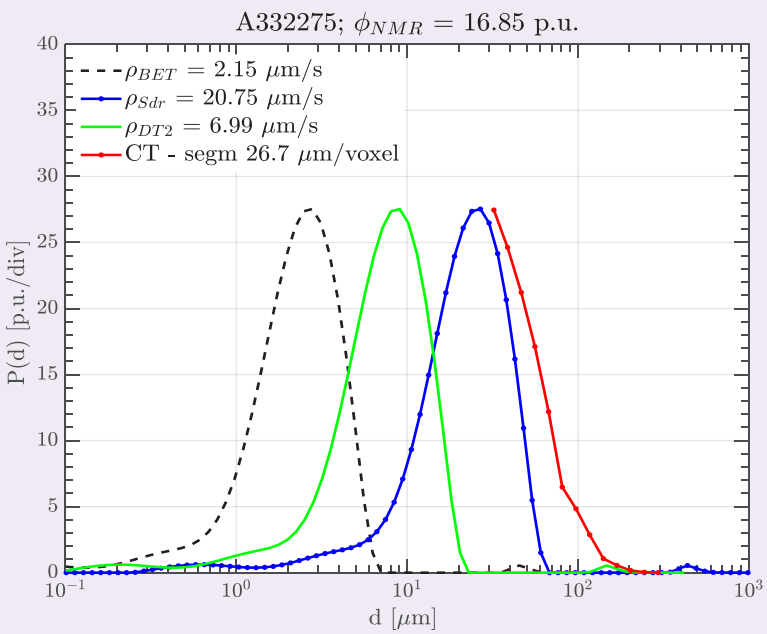

Fig. 26 *The effect of surface roughness on the surface relaxivity and pore size distribution for Y21.*

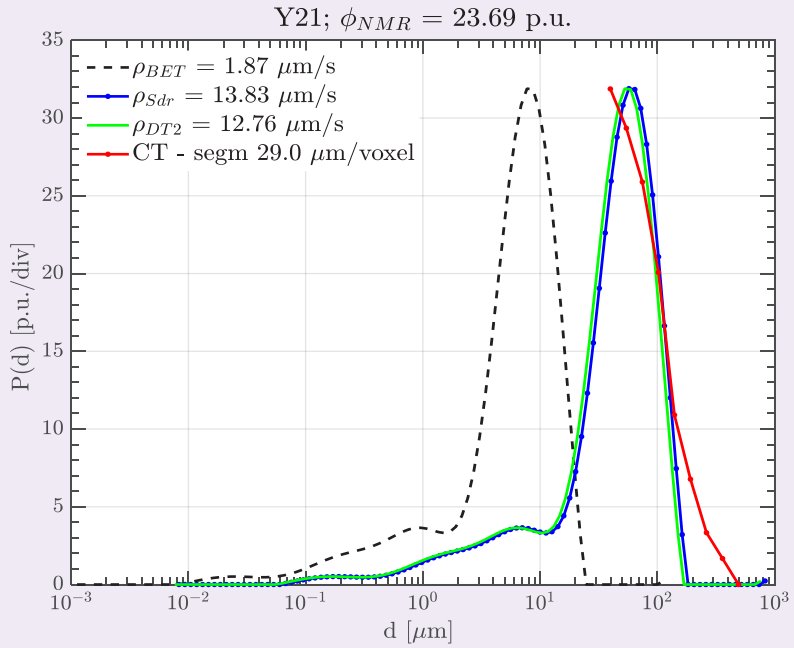

Conclusions

In this study, 2D *Sdr* derived from LSCM measurements and associated data processing algorithms were developed and validated with 29 carbonate core samples. In addition, various surface roughness parameters were calculated and the ones that are directly related to surface relaxivity, the NMR data interpretation, and the 1D absolute *Sr* and 2D *Sdr* were studied in detail. The general findings and conclusions are summarized as:

- The 1D *Sr* is based on a simple approximation model, while the 2D *Sdr* is a standard surface roughness parameter defined in ISO 25178-2:2012[5], and thereby is a more direct and sensitive roughness parameter that standardizes our approach with the surface characterization community.
- Another alternative method to measure surface roughness is based on the difference in length scales between the NMR *D*-T_2 and BET measurements. Although NMR *D*-T_2 is a bulk measurement, results derived from the NMR *D*-T_2 and BET measurements agree reasonably well with surface measurements of LSCM-based 1D *Sr* and 2D *Sdr*, provided that the *D*-T_2 method works within its validity range, i.e., the pore sizes are not too large, as such, there is sufficient restriction.
- Integrating surface roughness with the mean pore body size derived from the BET measurement reduces uncertainties in pore body size interpretation from NMR measurements.
- To validate, good agreement is found between the large pores from micro-CT imaging and that from NMR, with BET-based surface relaxivity after correcting for the effect of surface roughness.

Specific observations for the 1D *Sr* and 2D *Sdr* are:

1. **Surface preparation.** There are no significant effects of surface preparation on the 1D *Sr* and 2D *Sdr*; sawing and breaking surfaces gave very similar results.
2. **Data processing.** Both *Sr* and *Sdr* are robust against de-spiking and the Gaussian filter width σ, when σ > about 2.5 μm.
3. **Dynamic range.** The 2D *Sdr* has a wider dynamic range, indicating that it is more sensitive than the 1D *Sr*.
4. **Advantages.** Each one has its own specific advantages:
   - The 1D *Sr* histogram can reveal any roughness heterogeneity along the measurement direction.
   - The 2D *Sdr* is a standard roughness parameter, which is more robust against processing parameters, and is therefore easier to implement for practical applications.
5. **Robustness.** An excellent correlation was observed with a R^2 = 0.998 between the 1D *Sr* and 2D *Sdr*, which validates the use of 1D *Sr* in our previous study[1], and shows that both can be used for surface roughness characterization.
6. **Advancing drill cutting analysis.** Both 1D *Sr* and 2D *Sdr* can be measured on cutting samples, and the results are comparable to that of core plugs, as long as the sizes of cuttings are large enough; larger than the roughness features and the FOV of

the microscope setting. This is significant since it indicates the potential advancement of mud logging by extracting surface roughness features from drill cuttings and integrating them into log interpretation for enhanced formation evaluation.

Acknowledgments

We thank Philip Mendoza for the CT-scan data acquisition and processing, and Nathan Davis for allowing us to use the confocal microscope in the Halliburton MultiChem Lab and for helping with the instrument setup.

References

1. Ma, S.M., Singer, G., Chen, S. and Eid, M.: "Objective-Driven Solid Surface Roughness Characterization for Enhanced Nuclear Magnetic Resonance Petrophysics," *SPE Journal*, Vol. 26, Issue 4, October 2021, pp. 2860-2879.

2. Nordin, M. and Knight, R.: "The Effect of Surface Roughness on Nuclear Magnetic Resonance Relaxation," *Diffusion Fundamentals.org*, Vol. 26, Issue 3, 2016, pp. 1-11.

3. ISO 25178-2:2012: *Geometrical Product Specifications (GPS) — Surface Texture: Areal — Part 2: Terms, Definitions and Surface Texture Parameters*, April 2012, 47 p.

4. Sauerer, B., Al Hamad, M., Ma, S.M. and Abdallah, W.: "Effect of Oil-Based Mud Filtrate on the Wettability of Rock Surfaces with Different Mineralogy and Topology," *Energy Fuels*, Vol. 34, Issue 7, June 2020, pp. 8250-8259.

5. Olympus Manual: *Surface Roughness Measurement — Parameters*, *https://www.olympus-ims.com/en/metrology/surface-roughness-measurement-portal/parameters/.*

6. Wang, X., Singer, P.M., Liu, Y., Chen, Z., Hirasaki, G.J., et al.: "Permeability from NMR in Unconventional Point-Pleasant Formation," URTeC paper 2021-5015, presented at the SPE/AAPG/SEG Unconventional Resources Technology Conference, Houston, Texas, July 26-28, 2021.

7. Mitra, P.P., Sen, P.N., Schwartz, L.M. and Le Doussal, P.: "Diffusion Propagator as a Probe of the Structure of Porous Media," *Physical Review Letters*, Vol. 68, Issue 24, June 1992, pp. 3555-3558.

8. Latour, L.L., Mitra, P.P., Kleinberg, R.L. and Sotak, C.H.: "Time-Dependent Diffusion Coefficient of Fluids in Porous Media as a Probe of Surface-to-Volume Ratio," *Journal of Magnetic Resonance, Series A*, Vol. 101, Issue 3, February 1993, pp. 342-346.

9. Hürlimann, M.D., Helmer, K.G., Latour, L.L. and Sotak, C.H.: "Restricted Diffusion in Sedimentary Rocks. Determination of Surface-to-Volume Ratio and Surface Relaxivity," *Journal of Magnetic Resonance, Series A*, Vol. 111, Issue 2, December 1994, pp. 169-178.

10. Zielinski, L., Ramamoorthy, R., Minh, C.C., Al Daghar, K.A., et al.: "Restricted Diffusion Effects in Saturation Estimates from 2D Diffusion-Relaxation NMR Maps," SPE paper 134841, presented at the SPE Annual Technical Conference and Exhibition, Florence, Italy, September 19-22, 2010.

11. Dullien, F.A.L.: *Porous Media Fluid Transport and Pore Structure*, 1st edition, Academic Press: New York, 1979, 598 p.

12. Wang, X., Singer, P.M., Liu, Y., Chen, Z., et al.: "Pore Size, Tortuosity, and Permeability from NMR Restricted Diffusion in Organic-Rich Chalks," *Petrophysics*, Vol. 62, Issue 3, June 2021, pp. 244-264.

13. Suhrer, M., Toelke, J., Diaz, E., Grader, A., et al.: "Computed Two-Phase Relative Permeability Using Digital Rock Physics in a Shale Formation," paper presented at the International Symposium of the Society of Core Analysts, Napa Valley, California, September 16-19, 2013.

About the Authors

Dr. Gabriela Singer

Ph.D. in Nuclear Science and Engineering, Massachusetts Institute of Technology

Dr. Gabriela Singer (Leu) is a Principal Scientist contractor at Halliburton working in the Sensor Physics Department. Previously, she worked at Schlumberger for 12 years, as a Tool Physicist at the Schlumberger Houston Formation Evaluation Center in Houston, TX, and as a Senior Research Scientist in the Geology and Rock Physics Department at the Schlumberger-Doll Research in Cambridge, MA.

Gabriela received her B.S. degree in Physics from Alexandru Ioan Cuza University, Iasi, Romania, and her Ph.D. degree in Nuclear Science and Engineering from the Massachusetts Institute of Technology, Cambridge, MA.

Dr. Shouxiang M. Ma

Ph.D. in Petroleum Engineering, New Mexico Institute of Mining and Technology

Dr. Shouxiang M. "Mark" Ma is a Senior Petroleum Engineer Consultant overseeing research and development, subject matter technical support, and professional development in the Advanced Petrophysical Modeling Group of Saudi Aramco's Reservoir Description and Simulation Department. Prior to this, he was Supervisor of the Petrophysical Support & Study Unit, advisor at the Upstream Professional Development Center, and Lead Petrophysicist for logging operations.

Before joining Saudi Aramco in 2000, Mark worked at the Exxon Production Research Company, Wyoming Western Research Institute, New Mexico Petroleum Recovery Research Center, and China Yangtze University.

He served as a chairperson of the 2013 Society of Petroleum Engineers (SPE) Formation Evaluation Award Committee, the 2018 SPE Annual Technical Conference and Exhibition Formation Evaluation Committee, and on the 2019 International Petroleum Technology Conference Education Week Conference.

Mark was awarded the 2019 SPE MENA Formation Evaluation Award.

From 2015 to 2020, he served on the *JPT* Editorial Board where he was responsible for formation evaluation content. Mark is a Society of Petrophysicists and Well Log Analysts (SPWLA) Saudi Arabia Chapter vice president for technical events, and from 2018 to 2020, he was a SPWLA Director representing the Middle East and Africa region. Mark is also an Associate Editor for the *Journal of Petrophysics*, and Vice President of the SPWLA Saudi Arabia Chapter.

He received his B.S. degree from the China University of Petroleum, Shandong, China, and his M.S. and Ph.D. degrees from the New Mexico Institute of Mining and Technology, Socorro, NM, all in Petroleum Engineering.

Dr. Songhua Chen

Ph.D. in Physics, University of Utah

Dr. Songhua Chen is Senior Manager of the Nuclear Magnetic Resonance (NMR) Sensor Physics at the Halliburton Houston Technology Center. Since joining Halliburton 11 years ago, he has been leading a team of scientists and mathematicians to research and design new wireline Xaminer Magnetic Resonance (XMR) and logging while drilling (LWD) NMR sensors, as well as to optimize NMR data acquisition, processing, and interpretation methodologies. Most recently, Songhua's interest focuses on carbonate pore typing, unconventional reservoir fluid identification, and applying data analytic approaches in petrophysical interpretation.

In the last several years, he has also been closely collaborating with colleagues in Aramco's RDD on a number of applied research projects to advance carbonate formation evaluation technologies, core analysis methods, and machine learning and deep learning applications.

Prior to joining Halliburton, Songhua was with Baker Hughes for 15 years as a Staff Scientist and NMR Interpretation Project Leader, and later became Senior Manager of the Integrated Interpretation group to develop technologies involving NMR, geochemistry, fluid sampling/testing interpretations, and pore scale modeling.

Prior to working in the energy service industry, he was a Senior Scientist at Texas A&M University in College Station, Texas.

Songhua is an inventor or co-inventor of more than 90 U.S. patents in NMR downhole sensors, data processing and analytics, inversion, core analysis, and integrated petrophysics. He has authored or coauthored more than 100 publications, including book chapters, peer-reviewed journal papers, and conference proceedings.

Songhua is an active member of the Society of Petroleum Engineers (SPE) and the Society of Petrophysicists and Well Log Analysts (SPWLA). He was previously a vice president of Publications of SPWLA and the editor of the *Petrophysics* journal. Songhua was selected twice as the SPWLA Distinguished Speaker in 2006 and 2013, respectively, and is the recipient of the 2019 SPWLA Distinguished Technical Achievement Award.

He received his B.S. degree from the Nanjing Institute of Technology, Nanjing, China, and his Ph.D. degree from the University of Utah, Salt Lake City, UT, both in Physics.

Mahmoud Eid

M.S. in Reservoirs Characterization and Source Rock Evaluation, Cairo University

Mahmoud Eid works for Halliburton Wireline and Perforating as the Middle East and North Africa (MENA) Technical Sales and Marketing Regional Manager. He has more than 20 years of experience gained in drilling and wireline logging services, including open and cased hole operations, data post-processing, and interpretation,

Mahmoud spent the last 18 years in the Formation and Reservoir Solutions group at various locations within the MENA area, assisting logging operations, developing log quality processes, working on special formation evaluation projects and supporting customer Geosciences' Asset teams. His experience also includes developing expertise in a variety of formation evaluation techniques and in pulsed neutron log interpretation for major mature oil fields.

Currently, Mahmoud is leading the Technical Sales team within the MENA region to develop and promote customized reservoir solutions that meet customer challenges in the exploration of conventional and unconventional as well as in the development and mature fields utilizing open hole, cased hole, and coring technologies and technical offerings.

He is an active member of the Society of Petroleum Engineers (SPE) and the Society of Petrophysicists and Well Log Analysts (SPWLA).

In 2001, Mahmoud received his B.S. degree with a double major in Geology and Chemistry, and then received his M.S. degree in Reservoirs Characterization and Source Rock Evaluation, both from the Faculty of Science, Cairo University, Giza, Egypt.

Successful Intervention through Multilateral Completion Window for Logging and Wellbore Treatment

Hemant K. Sharma and Abdulrakeeb Almasri

Abstract /

An effective well completion design is crucial to maximize reservoir recovery rates, with many exploration and production (E&P) companies utilizing multilateral technology to achieve this important objective. Subsequently, as fields mature and more wells are drilled, cost-effective reservoir management becomes more challenging.

The E&P companies drill dedicated wells to collect important data for reservoir planning, with well logging conducted periodically to monitor the changes in the reservoir. Observation wells have been drilled in different locations to monitor the reservoir and assist with planning and intervention decisions; however, these wells can be costly and occupy valuable space that could be utilized for production. An alternate technique enables E&P companies to drill a pilot hole, perform all the necessary logging, and obtain the required reservoir information. The pilot hole is then plugged and abandoned. Even though this technique saves the space occupied by a dedicated observation well, the collected data only remains valid for a limited period due to potential changes to the reservoir.

The production and completion engineers have further leveraged this solution and developed a new multilateral well technology that addresses these challenges. These enhanced technologies allow wells to be completed with a pilot hole (vertical) drilled for reservoir evaluation throughout the life of the well, with a permanent downhole monitoring system with permanent downhole monitoring gauges (PDHGs) installed for pressure and temperature monitoring, while the horizontal lateral functions as an oil/gas producer. Combining the observation and producer wells into one well results in cost savings and maximum reservoir recovery and management. In addition, the capability to access the lateral allows for the intervention in both the motherbore and lateral at any time.

A well completed with this multilateral technology recently required intervention for well logging and treatment to revive the well. Slick line runs were performed to gain access to the horizontal lateral, which included retrieval of an isolation sleeve and installation of a tubing exit whipstock (TEW) for lateral reentry. Later, coiled tubing was run through the window into the lateral to perform intervention operations and revive the well. Upon completion of the intervention, the TEW was retrieved from the window, the isolation sleeve was reinstalled, and the revived well returned to production. Well intervention through this multilateral completion demonstrates the ease and efficiency of accessing both the vertical and horizontal lateral, without requiring a rig or completion retrieval.

This article will highlight the multilateral completion technology for accessing both the laterals, including real-time monitoring capabilities that provide more reliable data to maximize the recovery and management of the reservoir, as well as perform an effective intervention.

Introduction

Proper well completion design is key to successful production throughout the life of the well. Many technologies are under development worldwide to enhance well completions and simplify future well intervention. In particular, multilateral technology, which enables the drilling of multiple laterals from a single location and allows access to each lateral, provides a proven strategy to increase production from the wells, and reduce capital expenditure. Subsequently, because each field is different, multilateral completion strategies should be tailored to address the particular requirement of that field.

The ability to maintain well integrity during construction and provide full access to the well throughout its life cycle can be difficult. Lateral access is necessary for production optimization, reservoir management, and well treatment to enhance production and even to revive dead wells with enzyme treatment/acid stimulation. In addition, logging and well treatment is required occasionally to maintain well health and provide maximum sweep of the reservoir.

Type of Completions

Most wells drilled are vertical or horizontal with open hole or cased hole completions. In general, the wells that are completed as horizontal producers/injectors are either a single lateral with single packer completion or multilateral. Multilateral drilling can greatly impact production and overall well costs.

Therefore, an optimum well construction and completion strategy is crucial to achieve maximum benefits and address challenges that includes the following:

- A well construction method to help ensure well integrity during the life of the well.
- A completion method that will provide lateral access, pressure, and temperature monitoring, and simple installation and retrieval.

Well Construction Method

The Technology Advancement of Multilaterals (TAML) system categorizes multilateral wells according to junction functionality and complexity, designated TAML Levels 1 through 6. This ranking system is used to determine the appropriate lateral design.

The TAML levels are defined as follows:

1. TAML Level 1: An open hole lateral is drilled from an open hole main bore, Fig. 1. Level 1 multilaterals are drilled in fields with stable formations; however, flow control and lateral reentry cannot be achieved.

Fig. 1 *TAML Level 1.*

2. TAML Level 2: The main bore is cased and cemented and the lateral is an open hole or drop liner without connection at the junction, Fig. 2. Flow control for each lateral can be achieved when an isolation packer is installed below each window; however, lateral access is not possible unless the entire completion is retrieved.

Fig. 2 *TAML Level 2.*

3. TAML Level 3: The main bore is cased and cemented and the lateral is cased but uncemented. The lateral wellbore is mechanically joined to the main bore, but the junction is not hydraulically sealed, Fig. 3. Level 3 construction is not common in the oil industry.

Fig. 3 *TAML Level 3.*

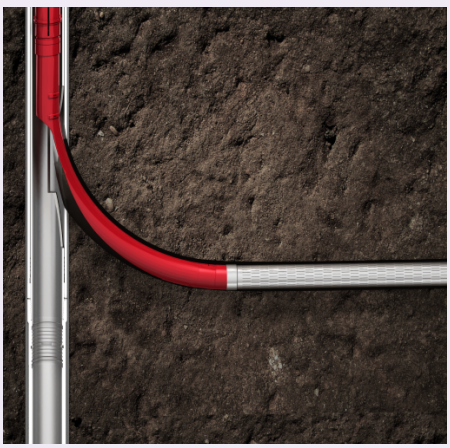

4. TAML Level 4: Both the main bore and lateral are cased and cemented and hydraulic integrity depends on the cement quality, Fig. 4.

Fig. 4 *TAML Level 4.*

5. TAML Level 5: The junction integrity is accomplished by the completion, and the junction can be cemented or uncemented, Fig. 5. The Level 5 system is common in fields where gas migration at the junction is detected.

Fig. 5 *TAML Level 5.*

6. TAML Level 6: Two branches are drilled from the original wellbore, and both mechanical and pressure integrity are achieved using the casing to seal the junction, Fig. 6.

The completion engineers extensively evaluated the available options to determine the best system for use to enhance production with the ability to access both the laterals. Based on the formation properties and well plans, it was agreed that Well-A would be constructed as a Level 4 multilateral to help ensure junction integrity. This integrity is achieved using a liner in the lateral that extends to the main bore, and cement pumped between the lateral and the formation provides the necessary support and prevents migration of unwanted fluid into the main bore.

Fig. 6 *TAML Level 6.*

Once the lateral liner is cemented, a washover assembly removes the cement remnants inside and leaves the well with a casing drift size lateral window. The Level 4 multilateral construction is common in the oil industry when the window is cut in the build section and a cemented section is required. This system is effective in providing well integrity.

Multilateral Completion Method

Selection of Multilateral Completion Equipment: The well required a multilateral completion system installed in a cost-effective manner that enabled accessing the well during the production phase, without rig intervention and without retrieving the completion equipment[1].

For Well-A, the system selected utilized a completion window that is designed as an integral part of the production string and equipped with landing profiles and sealbores to enable the setting of deflectors for lateral access or isolation sleeves for lateral flow control and isolation. These profiles are designed such that a special tool can be set inside the window for a specific objective.

Completion Window: The completion window is connected to the tubing and equipped with internal profiles for the service tool to achieve reentry access either to the main bore or the lateral, Fig. 7. The inner diameter of the window should be sufficient to allow the entire bottom-hole assembly (BHA) to run into the well and pass through to the main bore or the lateral.

Fig. 7 *The reentry window.*

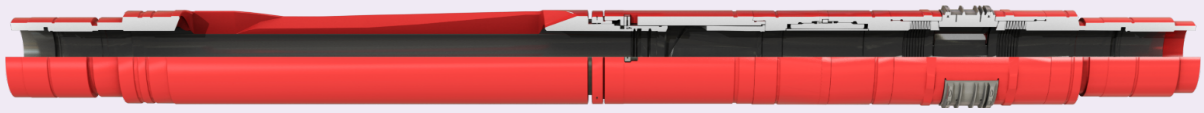

Fig. 8 *The reentry window oriented to the lateral.*

Fig. 9 *The reentry window with a pressure isolation sleeve installed.*

Fig. 10 *The reentry window with a TEW installed.*

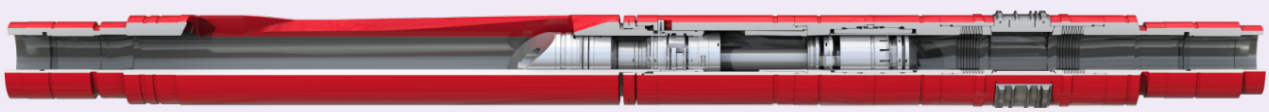

A latch coupling is run as part of the casing to help ensure the window is installed at the optimum depth, with the opening oriented to the lateral, Fig. 8.

Pressure Isolation Sleeve: The completion window has a profile to set the pressure isolation sleeve, Fig. 9, which isolates the lateral and helps ensure the BHA is directed to the main bore and logging can be performed. This sleeve is run and retrieved by a special running and retrieving tool.

Tubing Exit Whipstock (TEW): The reentry window has another profile to set the TEW when lateral intervention is necessary, Fig. 10. With the TEW tool set inside the window, any BHA run in the hole will be redirected to the lateral. The TEW is run and retrieved by a special running and retrieving tool.

Completion Packers and Accessories

Well-A was designed to include the following completion accessories, Fig. 11:

1. A lower production packer to isolate the main bore below the window.
2. Two permanent downhole gauges (PDHGs) above the completion reentry window for pressure and

Fig. 11 *A schematic of Well-A.*

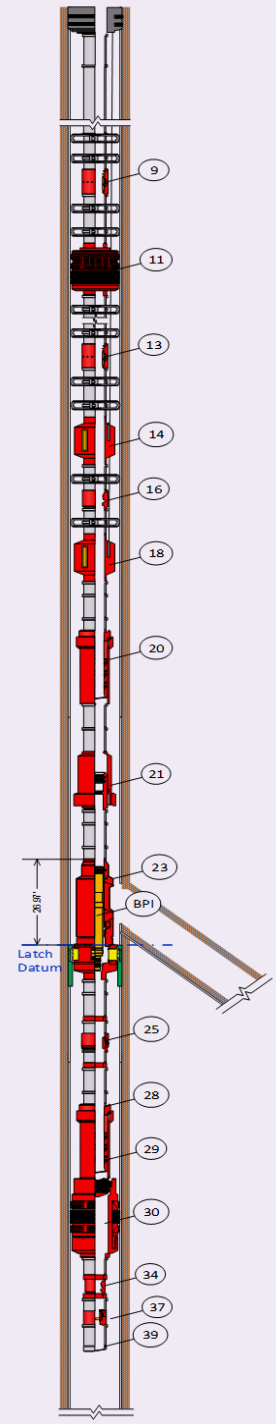

#	Assy	Description	Qty	OD	ID	Top (MD)	Length (ft)
1		Original Elevation (Estimated), (RKB to THF)		N/A	N/A	0.00	30.00
2		Tubing hanger, 4-1/2" 12.6# L-80 New Vam Box down.	1	11.000"	3.958"	30.00	1.00
3		Double Pin Sub: 4-1/2" 12.6# L-80 New Vam.	1	4.500"	3.958"	31.00	1.00
4		Tubing Joint, 4 1/2 12.6 # L-80 NewVam	2	4.500"	3.958"	32.00	80.00
5		Space out Pup Joints, 4 1/2" 12.6# New Vam L-80 (as req'd)	AR	4.500"	3.958"	112.00	37.06
8		Tubing Joint, 4 1/2 12.6 # L-80 NewVam	99	4.500"	3.958"	149.06	3,960.00
9	Upper SSD Assy	Pup Joint, 4 1/2 12.6 # L-80 NewVam	1	4.500"	3.958"	4,109.06	10.00
		4-1/2" 12.6# New Vam 3.813" "XU" SSD Durasleeve	1	5.600"	3.813"	4,119.06	2.00
		Pup Joint, 4 1/2 12.6 # L-80 NewVam	1	4.500"	3.958"	4,121.06	10.00
10		Tubing Joint, 4 1/2 12.6 # L-80 NewVam	1	4.500"	3.958"	4,131.06	80.00
		Pup Joint, 4 1/2 12.6 # L-80 NewVam	1	4.500"	3.958"	4,211.06	6.00
		Pup Joint, 4 1/2 12.6 # L-80 NewVam	1	4.500"	3.958"	4,223.16	6.00
12		Tubing Joint, 4 1/2 12.6 # L-80 NewVam	1	4.500"	3.958"	4,229.16	41.00
13	Lower SSD Assy	Pup Joint, 4 1/2 12.6 # L-80 NewVam	1	4.500"	3.958"	4,270.16	6.00
		4-1/2" 12.6# New Vam 3.813" "XU" SSD Durasleeve	1	5.600"	3.813"	4,276.16	2.00
		Pup Joint, 4 1/2 12.6 # L-80 NewVam	1	4.500"	3.958"	4,278.16	6.00
14	Upper PDHMS	Pup Joint, 4 1/2 12.6 # L-80 NewVam	1	4.500"	3.958"	4,284.16	6.00
		Gauge Mandrel Assembly 4 1/2 12.60 lb/ft NEWVAM PIN-PIN Connection Type . ANNULUS PORTED	1	5.990"	3.938"	4,290.16	6.20
		Pup Joint, 4 1/2 12.6 # L-80 NewVam	1	4.500"	3.958"	4,296.36	6.00
15		Tubing Joint, 4 1/2 12.6 # L-80 NewVam	1	4.500"	3.958"	4,302.36	41.00
16	X Nipple assy	Pup Joint, 4 1/2 12.6 # L-80 NewVam	1	4.500"	3.958"	4,343.36	6.00
		4 1/2" 12.6# N. VAM X-NIPPLE 3.813".	1	5.050"	3.813"	4,349.36	2.00
		Pup Joint, 4 1/2 12.6 # L-80 NewVam	1	4.500"	3.958"	4,351.36	6.00
17		Tubing Joint, 4 1/2 12.6 # L-80 NewVam	1	4.500"	3.958"	4,357.36	40.00
18	Lower PDHMS	Pup Joint, 4 1/2 12.6 # L-80 NewVam	1	4.500"	3.958"	4,397.36	6.00
		Gauge Mandrel Assembly 4 1/2 12.60 lb/ft NEWVAM PIN-PIN Connection . TUBING PORTED	1	5.990"	3.938"	4,403.36	6.00
		Pup Joint, 4 1/2 12.6 # L-80 NewVam	1	4.500"	3.958"	4,409.36	6.00
19		Tubing Joint, 4 1/2 12.6 # L-80 NewVam	1	4.500"	3.958"	4,415.36	41.00
20	PBA Assy	Pup Joint, 4 1/2 12.6 # L-80 NewVam	1	4.500"	3.958"	4,456.36	6.00
		PBA Polished Bore Receptacle Assembly 7	1	8.120"	3.850"	4,462.36	23.04
		LOCATOR, 4.880 BORE, 4 1/2-12.60 NEWVAM X 4 1/2-12.60 VAMTOP-SC80, BOX-BOX,	1	5.124"	3.850"	4,462.36	0.99
		Spacer Bar/ Pup Joint 175.0 in. Length 4 1/2-12.60 VAMTOP Pin-pin	1	4.545"	3.894"	4,463.35	14.90
		VTP Premium Seal Unit 4.880 in.4 1/2-12.60 VAMTOP-SC80 Box x 4 3/8-10 UNS-2A Pin	1	4.850"	3.860"	4,478.25	3.85
		Halliburton Self-Aligning Muleshoe Guide 4.880 Seal Bore ID-Min 4 3/8-10 UNS-2B Box	1	4.850"	3.860"	4,482.10	3.30
		End of production seal assy.				4,485.40	
		PBR Polished Bore Receptacle Assembly	1	8.120"	4.880"	4,463.35	22.80
		Pup Joint, 4 1/2 12.6 # L-80 NewVam	1	4.500"	3.958"	4,486.15	10.00
21	On-Off Tool	Pup Joint, 4 1/2 12.6 # L-80 NewVam	1	4.500"	3.958"	4,496.15	10.00
		Pup Joint, 4 1/2 12.6 # L-80 NewVam	1	4.500"	3.958"	4,514.75	10.00
22		Tubing Joint, 4 1/2 12.6 # L-80 NewVam	4	4.500"	3.958"	4,524.75	160.00
23	IsoRite Assy	Pup Joint, 4 1/2 12.6 # L-80 NewVam	1	4.500"	3.958"	4,684.75	10.00
		Window, 4 1/2" 12.6 New Vam BxP with Bottom No-Go Pressure Isolation Sleeve (BPI) installed Top of the IsoRite Assembly to the Latch Key Datum (Min ID 3.55" on window & 3.56" lateral access)	1	8.200"	2.967"	4,694.75	26.97
		Latch Key Datum to the bottom of the window Assembly (Max OD on Latch Keys, expanded. But, 8.180" OD on latch assembly body)		9.030"	3.850"	4,722	6.49
		Pup Joint, 4 1/2 12.6 # L-80 NewVam	1	4.500"	3.958"	4,728.20	4.00
24		**X-over 4 1/2" New Vam Box to 3 1/2" EUE Pin, L-80**	1	4.500"	2.992"	4,732.20	2.00
		SWV JT ASSY 3 1/2 9.3# EUE BxP	1	4.430"	2.953"	4,734.20	1.94
26		**X-over 4 1/2" New Vam Pin to 3 1/2" EUE Box, L-80**	1	4.500"	2.992"	4,736.14	2.00
27		Tubing Joint, 4 1/2 12.6 # L-80 NewVam	20	4.500"	3.958"	4,738.14	800.00
28	Locator seal assy.	Pup Joint, 4 1/2 12.6 # L-80 NewVam	1	4.500"	3.958"	5,538.14	4.00
		PSA Polished Bore Receptacle Seal Unit Assembly	1	5.124"	3.850"	5,542.14	23.04
		LOCATOR, 4.880 BORE, 4 1/2-12.60 NEWVAM X 4 1/2-12.60 VAMTOP-SC80, BOX-BOX,	1	5.124"	3.850"	5,542.14	0.99
		Spacer Bar/ Pup Joint 175.0 in. Length 4 1/2-12.60 VAMTOP Pin-pin	1	4.545"	3.894"	5,543.13	14.90
		VTP Premium Seal Unit 4.880 in.4 1/2-12.60 VAMTOP-SC80 Box x 4 3/8-10 UNS-2A Pin	1	4.850"	3.860"	5,558.03	3.85
		Halliburton Self-Aligning Muleshoe Guide 4.880 Seal Bore ID-Min 4 3/8-10 UNS-2B Box	1	4.850"	3.860"	5,561.88	3.30
		End of production seal assy.				5,565.18	
29	PBR	PBR Polished Bore Receptacle Assembly	1	8.120"	4.880"	5,550.14	22.80
30	Packer Assembly	RLV Ratch-Latch™ Seal Assembly with VTR Seal 5.250-6 RTH LTH LH Latch Type	1	5.290"	3.938"	5,586.94	1.89
		9 5/8" 40:47# Hydraulic Set, Retrievable Production Packer	1	8.460"	3.880"	5,588.83	6.47
		Pup Joint, 4 1/2 12.6 # L-80 NewVam	1	4.500"	3.958"	5,595.30	6.00
31		Tubing Joint, 4 1/2 12.6 # L-80 NewVam	1	4.500"	4.000"	5,601.30	40.00
32		**X-over 4 1/2" New Vam Box X 3 1/2" EUE Pin, L-80**	**1**	**4.500"**	**2.992"**	**5,641.30**	**2.00**
33		Tubing Joints, 3 1/2 9.3# L-80 EUE	1	3.500"	2.992"	5,643.30	30.00
34	X-nipple	PUP JOINT 3 1/2" 9.30# L-80 EUE	1	3.500"	2.992"	5,673.30	10.00
		PUP JOINT 3 1/2" 9.30# L-80 EUE	1	3.500"	2.992"	5,685.30	6.00
35		Tubing Joints, 3 1/2 9.3# L-80 EUE	1	3.500"	2.992"	5,691.30	31.00
36		**X-over 4 1/2" New Vam Pin X 3 1/2" EUE Box, L-80**	**1**	**3.500"**	**2.992"**	**5,722.30**	**2.00**
		Pup Joint, 4 1/2 12.6 # L-80 NewVam	1	4.500"	4.000"	5,726.30	4.00
38		Tubing Joint, 4 1/2 12.6 # L-80 NewVam	18	4.500"	4.000"	5,730.30	729.00
39	Mule Shoe	Pup Joint, 4 1/2 12.6 # L-80 NewVam	1	4.500"	4.000"	6,459.30	10.00
		4-1/2" 12.6# L-80 NEW VAM Mule Shoe Guide (6" inside the TOL)	1	4.960"	3.850"	6,469.30	0.70
		End Of Tubing				**6,470.00**	

temperature monitoring. The lower gauge sensor measures tubing pressure from the main bore; the upper gauge sensor measures annulus pressure from the lateral. The real-time readings allow the production team to detect changes as they occur.

3. Two sliding side door devices that open and close using a slick line. One sliding side door located below the upper packer flows the well through. A second sliding side door located above the upper packer displaces the well for lifting before moving the rig.
4. An upper feed through production packer to isolate the flow of the lateral and direct it into the sliding side door below the packer.
5. One landing nipple positioned between the PDHGs. The landing nipple includes a plug to isolate the two PDHGs, which helps prevent interference between the main bore and the lateral.
6. One landing nipple positioned below the lower packer to isolate the main bore, if necessary, during lateral operations.

Advantages of TAML Completion

It is well-known and field proven that longer laterals help increase production, and many exploration and production (E&P) companies drill horizontal wells despite the increase in cost and additional challenges; however, as well depths increases, more challenges arise. Therefore, multilateral drilling has become a necessity to achieve higher production because multiple laterals can be drilled without going too deep into the reservoir.

Equalizer completion technology, consisting of an inflow control device (ICD) and open hole packers, have proven effective in horizontal and multilateral wells, to help ensure effective water shutoff. Some E&P companies utilize ICDs with built-in sliding side doors, which provides the option to shut-in any lateral zone should water breakthrough occur. The reentry window system provides the lateral access necessary to perform these intervention operations efficiently.

Wellbore Cleanup

Candidate Well Description: The candidate well, Well-A, was drilled open hole and completed with the multilateral reentry window system and active ICDs separated by open hole packers in the lower completion. Consequently, when put on production, Well-A was dead. Several attempts to revive the well, which included lowering the pressure in the test trap, were unsuccessful. A detailed investigation of the drilling process determined that the pay zone was drilled using water-based polymer inhibited mud.

In general, after drilling the well and before completion, if no circulation loss occurs, an enzyme-based treatment fluid can be placed and soaked to break the polymer in the filter cake. Due to high permeable streaks with loss circulation zones in Well-A, an enzyme-based treatment could not be performed because the treatment fluid will follow the easiest path to the high permeable zones and leave other zones untreated.

Fig. 12 *A microscopic view of the damage caused by different types of polymers.*

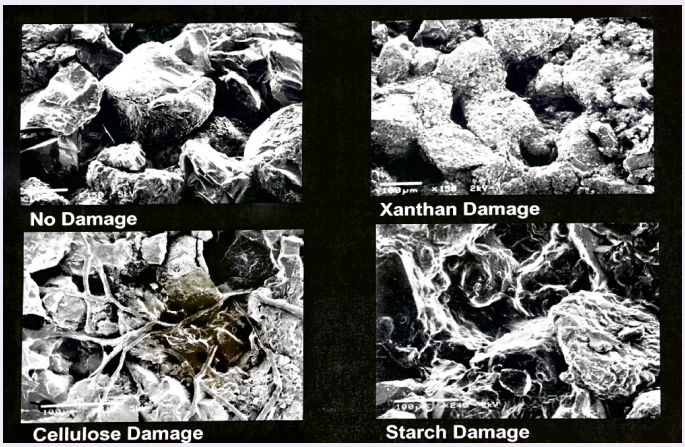

Well performance was evaluated using nodal analysis, which confirmed that under the existing reservoir conditions, the well could produce the reservoir fluid to the surface. In addition, sensitizing the well parameters for extremes, such as high water cut and slight reduction in the reservoir, also confirmed well flow.

Drill-In Fluid

The drill-in fluids (DIFs) are typically composed of starch, xanthan, or cellulose sized calcium carbonate ($CaCO_3$) chips (fine or medium) with salt particulates to increase the mud weight. The starch or cellulose provides the viscosity for friction reduction and lubrication while the xanthan polymer provides enhanced cutting transport capabilities. The $CaCO_3$ chips and salt particulates provide the required fluid loss control.

Although the DIFs are less damaging than the conventional mud used in the oil industry, impermeable filter cakes are still formed. Insufficient degradation of the filter cakes resulting from even these clean DIFs can significantly impede flow capacity at the wellbore wall. This results in high skin buildup at the borehole, which reduces production or injection.

During horizontal drilling, the reservoir fluid and drilling fluid contact at the heel of the lateral is increased by five to 10 times vs. vertical wells, and results in higher wellbore damage. Formation damage from drilling fluid leakoff and filter cake impairment should be eliminated to realize the full potential in horizontal and multilateral completions[5]. Figure 12 shows a microscopic view of the damage caused by the polymers.

To minimize the damage caused by drilling fluid, particularly while drilling horizontal wells, clean brine-based DIF with acid or water-soluble weighting agents are used, followed by an acid or oxidative breaker system to dissolve filter cake solids and polymers. If oil-water contact is not an issue, 15% hydrochloric (HCl) acid, with pre-flush and post-flush, is the generally accepted industry method. Although, if oil-water contact is near the pay zone, using acid might connect

the wellbore fluid to the water zone, and water will dominate fluid flow in the wellbore, which can lead to loss of oil production and ultimately the well.

This is more an issue in horizontal wells, because the acid will follow the least-resistant path in the wellbore and easily connect to fissure/fractures that leads to increased water production. The issue is aggravated in wells with an extended horizontal section, where acid treatment is ineffective. Lack of wellbore cleanup performed before completing these wells can cause costly completion delays, particularly during multilateral drilling, due to rig nonproductive time. In addition, flow line connection delays to the production header, caused by pore throat plugging by the DIF polymer, can lead to nonproductive wells after opening.

Basics of Using Polymers for Drilling Pay Zone

A polymer is a large molecule, or macromolecule, composed of many repeated subunits. These substances often form into a chain-like structure. Due to their broad range of properties, both synthetic and natural polymers play essential and ubiquitous roles in everyday life. Polymers range from familiar synthetic plastics, such as polystyrene, to natural biopolymers, such as deoxyribonucleic acid and proteins that are fundamental to biological structure and function.

Polymers, both natural and synthetic, are created via the polymerization of many small molecules, known as monomers. Their consequently large molecular mass relative to small molecule compounds produces unique physical properties, such as toughness, viscoelasticity, and a tendency to form glasses and semi-crystalline structures, rather than crystal[2].

Polymers are used in the DIF to build sufficient viscosity to transport cuttings and deposit a filter cake around the wellbore to reduce fluid loss. Polymers are primarily used for filtration control, usually as supplemental additives to bentonite or other chemicals. They are also used for viscosity modification, flocculation, and shale stabilization. Most DIFs are composed of starch, cellulose, or xanthan polymers added with bridging agents, such as $CaCO_3$ and salt particles[3].

DIF polymers can be classified as synthetic or natural polymers, Fig. 13. In addition, a combination of natural and synthetic polymers can be made by adding side chains onto natural polymers[4].

Natural polymers include starch, guar gum, and xanthan gum. The natural gums are complex materials that are more stable under adverse conditions of heat and acid. This structural complexity provides more complex rheological characteristics.

- Starch is used in the oil industry as a filtrate control and shale stabilization material. Starches used in the oil field are either made from corn or potatoes, which are processed to make them water-soluble. Moreover, starches are susceptible to bacterial degradation and will require preservatives when used.
- Guar gum is a nonionic, high molecular weight polysaccharide derived from the seed of the guar plant and is commonly used during proppant transport while fracturing. Guar gum is also susceptible to bacterial degradation and will require preservatives when used.
- Xanthan gum is a high molecular weight bio-polysaccharide produced by bacterial growth. Each individual bacterium produces a coating composed of this polymer. It is used by bacterium as a protective mechanism to prevent dehydration. The polymer is produced by a fermentation process, precipitation in alcohol, and then drying and milling the product to a powder form. Xanthan gum is used as a viscosifier and suspending agent.

Synthetic polymers include cellulosics, acrylates, acrylamides, and maleic anhydride derivatives.

- Cellulosics are organic compounds with the formula $(C_6H_{10}O_5)n$. The polysaccharides consist of a linear chain of several hundreds to several thousands of $\beta(1\rightarrow4)$ linked D-glucose units. Cellulose is an important structural component of the primary cell wall of green plants, many forms of algae, and oomycetes.
- Polyacrylamides are a synthetic material manufactured by attaching monomers together under appropriate temperature and pressure conditions. The acrylamides can be prepared according to specific application requirements; the polymer weight and degree of hydrolysis determine the viscosity exhibited by the polymer in water solutions. Polyacrylamides are mainly used for viscosity control during enhanced oil recovery and as a shale-stabilizing mechanism in drilling fluids.
- Polyacrylates/maleic anhydride derivatives are synthetic materials and can be made in a wide range of molecular weights with various charges on the molecules. Many types of polyacrylates are manufactured by combining various acrylic acid monomers. The type and number of monomers determine the end product properties. Polyacrylates

Fig. 13 *DIF polymers can be classified as synthetic or natural polymers.*

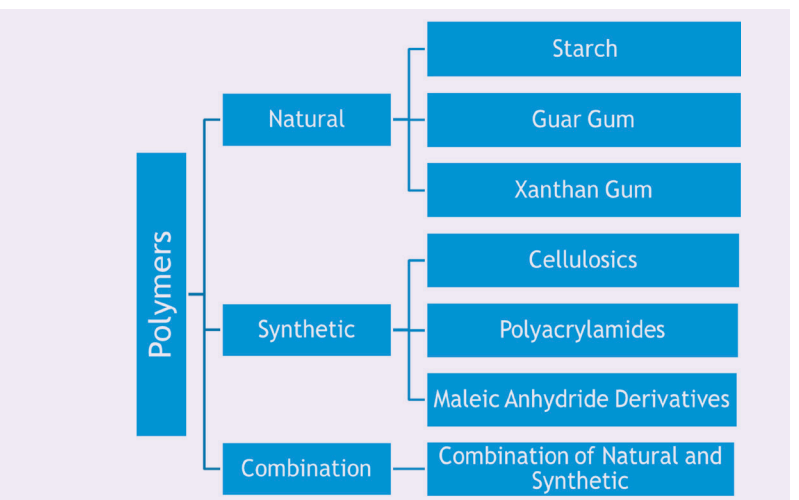

are used for flocculants, bentonite extenders, and shale stabilizing additives. The maleic anhydride copolymers are similar to acrylates and are used mainly as bentonite extenders in freshwater systems.

The polymer mud in the DIF invades the near wellbore area and creates skin damage, which is more pronounced in horizontal and multilateral wells due to a longer contact time and larger area.

Enzyme Treatment

Enzymes are protein catalysts, Fig. 14, that can promote various reactions under a mild range of acceptable conditions of pH and temperature[5]. Enzymes act as organic catalysts; they increase the rate of reaction while their chemical structure remains unchanged. As a catalyst, enzymes can increase the rate of reaction as much as 1 billion times. Hundreds of different enzymes with different catalytic activities exist. These activities are often specific; a certain enzyme can only catalyze the breakdown or synthesis of certain compounds. Because the enzymes are catalysts, only a small quantity of enzyme is required and is regenerated during the reaction.

For wells drilled with polymer mud, the enzymes are used to break the polymers into their natural elements (carbon, hydrogen, oxygen, and nitrogen), after converting the insoluble polymers into water-soluble sugars. The substances at the start of the reaction are substrates, and the substances at the end of the reaction are products. Enzymes work on the substrates and turn them into products.

During filter cake removal, specific enzymes are used for the specific type of filter cake in the formation. Enzymes used to dissolve polymers in wells drilled using xanthan gum will not dissolve starch until both types are mixed and placed in the wellbore.

The gentle action of an enzyme-based wellbore cleanup fluid on filter cake (starch and xanthan) enables placement across the horizontal section before the reaction progresses to help ensure even treatment distribution throughout the horizontal section. This leads to uniform dissolution and removal of the filter cake from the entire wellbore. Weak and dilute organic acid is also used in the treatment, which is either mixed with the enzyme or treated before the enzyme treatment. The weak acid treatment breaks the mechanical integrity of the mud cake and results in effective wellbore cleanup. This combination of enzyme and organic acid work in synergy; enzymes dissolve the polymer coating on the $CaCO_3$ particles, exposing them to acid reaction. The resulting acid reaction (and production of carbon dioxide) reduces the mechanical strength of the mud cake and enables further penetration of the enzyme. Figure 15 shows the enzyme action on the filter cake.

Enzymes also have significant potential to generate desirable chemicals in situ after fluid placement. Acid can be delivered deep into the rock matrix, fractures, or even long horizontal intervals. This allows successful acidizing where conventional highly reactive acids, such as HCl acid, are ineffective due to lack of penetration as a result of spent acid near the point of injection. This process uses esterase enzymes to generate organic acid (acetic acid).

Fig. 14 *An illustration of a microscopic enzyme protein.*

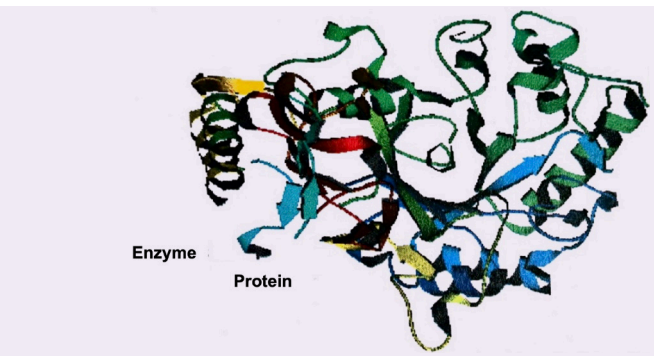

Operational Summary

Well-A

The well was drilled in a location where the reservoir support is sufficient to lift the wellbore fluid, even with higher water cut. Well-A, as described, could not flow after drilling and completing the well with the reentry window system. Multiple investigations were performed to confirm well readiness, which includes opening the lower sliding sleeve such that the tubing could be connected with the reservoir. Further

Fig. 15 *The enzyme action on filter cake.*

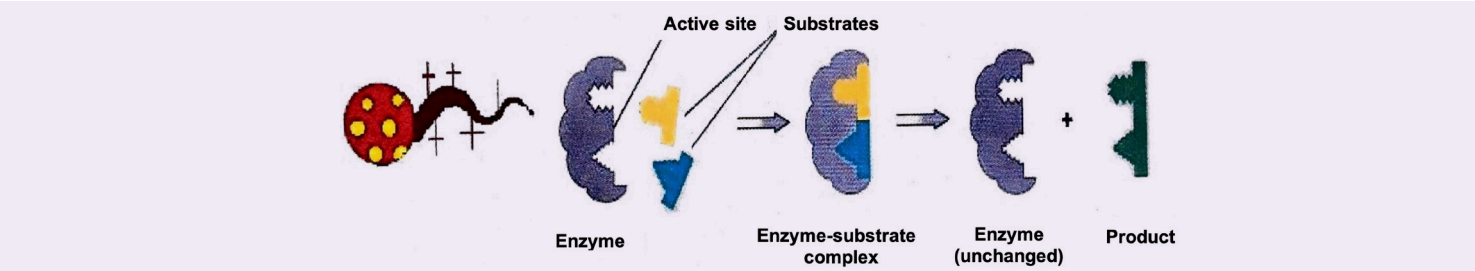

investigation confirmed that the well was drilled with 72-pcf polymer mud and no enzyme treatment was performed to break the polymers.

The well was sidetracked and completed as a horizontal producer with equalizer completion consisting of nine active/active ICDs (with sliding sleeve), separated by three open hole packers.

To address reservoir challenges and revive the well, lateral access was necessary for treatment.

Using a slick line, the following operations were performed:

- A brush run was performed before running the retrieving or running tool because debris could have accumulated inside the tubing, particularly in the profile area, which could jeopardize the next operation.
- A PX plug was retrieved from the nipple profile. This step was performed in three slick line trips: (1) retrieving the junk basket, (2) retrieving the prong, and (3) retrieving the plug.
- A pressure isolation sleeve was retrieved from the reentry window using the retrieving tool, Figs. 16 and 17. Jarring was required to remove the seal from the profile.
- A slick line brush was used to clean the profile area inside the reentry window.
- A TEW with a running tool was attached to the slick line and installed in the reentry window, Fig. 18 and Fig. 19, respectively. After the TEW was installed, the slick line with the running tool was pulled out of the hole.
- A treatment BHA was run in hole past the window and into the lateral, Fig. 20.
- Enzyme treatment was performed to clean the wellbore.
- After the treatment was complete, the slick line was pulled out of the hole.
- The retrieving tool was run on a slick line and the TEW was retrieved.
- The pressure isolation sleeve was run with a slick line and installed inside the reentry window.
- The PX plug was installed in the landing nipple below the upper production packer.
- The well was delivered and later put on production.

Fig. 16 *A pressure isolation sleeve retrieved by a slick line.*

Fig. 17 *A pressure isolation sleeve outside the window.*

Fig. 18 *A TEW run on a slick line and installed in the window.*

Fig. 19 *A TEW installed inside the reentry window.*

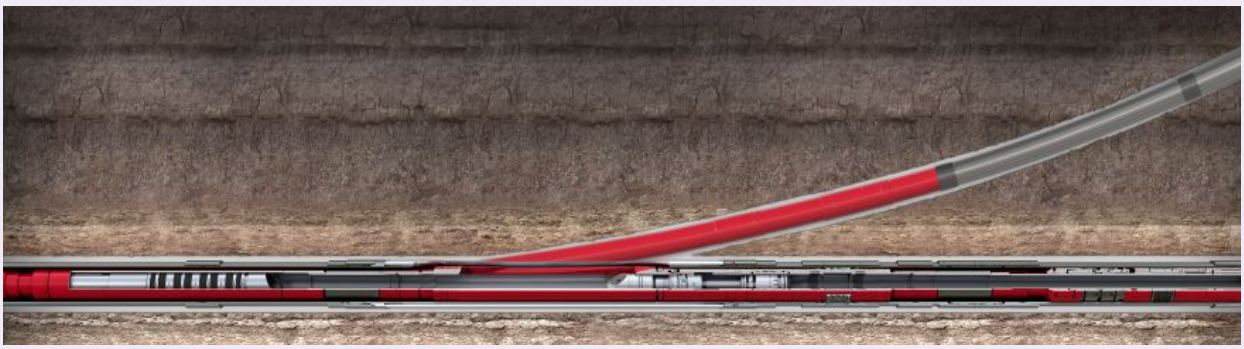

Fig. 20 *The wellbore treatment BHA was run inside the lateral.*

Table 1 *The production summary of Well-A after initial treatment and 6 months after the initial treatment.*

Well	Action	Water Cut (%)	Decrease in Water Production (%)	Increase in Oil Production (%)
Well-A	After drilling and putting well on production	63	34	2,664
	After treatment	29		

Production Performance

The successful enzyme treatment in the wellbore using coil tubing helped dissolve the polymers and the well was revived with very encouraging results. In fact, the well began to flow naturally after reentry window operations, including wellbore treatment and the planned nitrogen kickoff job was cancelled. Table 1 shows the production rate for Well-A immediately after the initial treatment and also 6 months after the initial treatment.

Conclusions

The following conclusions are based on the operation performed on an iso-rite completed well, which was dead after completion and treatment fluid were pumped to liven the well:

- The new multilateral completion technology enabled improvement in the production optimization strategy and the functionality of the ICD.
- Multilateral completions address multiple issues encountered during the life of the well.
- The technology has unlocked several additional methods to improve the water shutoff strategies, which could have become more complicated with the passage of time.
- The polymer forms a long chain and helps minimize the leakoff of the drilling mud into the formation.
- The polymer mixed in the DIF is designed to naturally disintegrate with a shelf life of 1 to 3 months. Although, in many of the wells, the polymer did not naturally disintegrate, even after 6 to 24 months.
- Polymers (starch and xanthan) mixed in the DIF are responsible for plugging the wellbore.
- In general, the life of the polymer is controlled by the crosslinker, which can be manipulated according to completion requirements.
- Enzymes attack specific polymers; therefore, treatment should be designed based on the type of polymer used.
- The enzyme treatment for wells drilled with polymer mud showed encouraging results. Well productivity substantially increased, with some wells revived by the treatment alone and without nitrogen kickoff.
- If the polymer is unable to disintegrate naturally, wellbore plugging can cause a well control situation because the kill fluid might not be able to kill the well (due to low injectivity).
- The latest practice of displacing the open hole with oil-based mud (OBM) before completing the lower section with ICDs helps reduce the filter cake thickness, and ultimately the well is able to flow when open to production.

Recommendations

The technology presented has proven useful and should be considered to maximize well performance. The following is recommended:

1. Select strategic locations for the application of reentry window technology.
2. Improve the technology such that a reduced number of runs are necessary during the intervention process.
3. After drilling the pay zone with polymer-based mud, perform enzyme treatment to regain wellbore productivity.
4. Selectively treat wells, partially drilled using polymer-based mud, with enzymes if complete losses (fractures were opened) occur while drilling the pay zone.
5. Perform proper wellbore circulation and cleanout before completing the wells to help ensure effective enzyme treatment.
6. Displace the open hole with OBM, even if the pay zone is drilled with water-based mud.

Acknowledgments

This article was presented at the SPE Annual Technical Conference and Exhibition, Houston, Texas, October 3-5, 2022.

References

1. Al Ansari, N. and Racine, B.: "A Successful Deployment of Level 4 Multilateral Isolation Completion System," SPE paper 197581, presented at the Abu Dhabi International Petroleum Exhibition and Conference, Abu Dhabi, UAE, November 11-14, 2019.
2. Sharma, H.K., AlKhalifah, Q., Al-Mulhim, A.K. and Al-Shammari, M.J.: "Successful Wellbore Cleanup Using Environmentally Friendly Chemicals to Enhance Well Productivity," SPE paper 199271, presented at the SPE International Conference and Exhibition on Formation Damage Control, Lafayette, Louisiana, February 19-21, 2020.
3. Mehtar, M.A., Kasam, Y., Al-Aleeli, A., Ghosh, B., et al.: "Derivation of Kinetic Rate Constant of Enzyme Buffer Mud Cake Clean Up Systems — Laboratory Investigation and Verification in High Temperature Fractured Carbonate Reservoir," SPE paper 161643, presented at the Abu Dhabi International Petroleum Conference and Exhibition, Abu Dhabi, UAE, November 11-14, 2012.
4. Carico, R.D. and Bagshaw, F.R.: "Description and Use of Polymers Used in Drilling, Workovers, and Completions," SPE paper 7747, presented at the SPE Production Technology Symposium, Hobbs, New Mexico, October 30-31, 1978.
5. Suhy, T.E. and Harris, R.P.: "Application of Polymer Specific Enzymes to Clean Up Drill-in Fluids," SPE paper 51094, presented at the SPE Eastern Regional Meeting, Pittsburg, Pennsylvania, November 9-11, 1998.

About the Authors

Hemant K. Sharma

MBA,
Indira Gandhi National Open University

Hemant K. Sharma is a Supervisor of the Hawiyah Production Engineering Unit in Saudi Aramco's Southern Area Production Engineering Department. He has more than 30 years of experience in the oil and gas industry, which includes onshore and offshore technical support.

Hemant's experience and knowledge includes production enhancement and sustainability, formation damage diagnosis and remediation, well stimulation, water shutoff, well surveillance and monitoring, well completion and wireline, and long-term planning/forecasting and construction/commissioning of large oil and gas complexes.

In 1990, he received his M.Eng. degree from Bhagalpur College of Engineering, Bihar, India, and in 2005, Hemant received an MBA from Indira Gandhi National Open University, Delhi, India.

Abdulrakeeb Almasri

B.S. in Civil Engineering,
Sana'a University

Abdulrakeeb Almasri is a Senior Business Development Account Representative in Halliburton's Completion Tool Department at Halliburton Saudi Arabia. He is a subject matter expert for completion and multilateral completions with more than 16 years of experience. As a completion design expert, Abdulrakeeb has working experience in well completion design and evaluation for standard well completions, multilateral well completions, and smart well completions.

He received his B.S. degree in Civil Engineering from Sana'a University, Sana'a, Yemen.

Notes

Notes

Have an article you would like to publish? Here are our guidelines.

These guidelines are designed to simplify and help standardize submissions. They need not be followed rigorously. If you have any questions, please call us.

Length

Average of 2,500-4,000 words, plus illustrations/photos and captions. Maximum length should be 5,000 words. Articles in excess will be shortened.

What to send

Send text in Microsoft Word format via email. Illustrations/photos should be clear and sharp. Editable files are requested for graphs, i.e., editable in Excel.

Procedure

Notification of acceptance is usually within three weeks after the submission deadline. The article will be edited for style and clarity and returned to the author for review. All articles are subject to the company's normal review. No paper can be published without a signature at the manager level or above.

Format

No single article need include all of the following parts. The type of article and subject covered will determine which parts to include.

Working Title
Lorem Ipsum here.

Abstract
Usually 150-300 words to summarize the main points.

Introduction
Different from the abstract in that it sets the stage for the content of the article, rather than telling the reader what it is about.

Main body
May incorporate subtitles, artwork, photos, etc.

Conclusion/Summary
Assessment of results or restatement of points in introduction.

Endnotes/References/Bibliography
Use only when essential. Use author/date citation method in the main body. Numbered footnotes or endnotes will be converted. Include complete publication information. Standard is *The Associated Press Stylebook*, 52nd ed. and *Wesbter's New World College Dictionary*, 5th ed.

Acknowledgments
Use to thank those who helped make the article possible.

Illustration/Tables/Photos and explanatory text

If the files are large, these can be submitted separately, due to email size limits. Initial submission may include copies of originals; however, publication will require the originals. When possible, submit original images. Color is preferable.

File Format

Illustration files with .EPS extensions work best. Other acceptable extensions are .TIFF/.JPEG/.PICT.

Permission(s) to reprint, if appropriate

Previously published articles are acceptable but can be published only with written permission from the copyright holder.

Author(s)/Contibutor(s)

Please include a brief biographical statement.

Submission/Acceptance Procedures

Papers are submitted on a competitive basis and are evaluated by an editorial review board comprised of various department managers and subject matter experts. Following initial selection, authors whose papers have been accepted for publication will be notified by email.

Papers submitted for a particular issue but not accepted for that issue may be carried forward as submissions for subsequent issues, unless the author specifically requests in writing that there be no further consideration.

Submit articles to:

Editor
The Saudi Aramco Journal of Technology
C-10B, Room AN-1080
North Admin Building #175
Dhahran 31311, Saudi Arabia
Tel: +966-013-876-0498
Email: *william.bradshaw.1@aramco.com.sa*

Submission deadlines

Issue	Paper submission deadline	Release date
Spring 2023	November 7, 2022	March 31, 2023
Summer 2023	February 1, 2023	June 30, 2023
Fall 2023	May 9, 2023	September 30, 2023
Winter 2023	August 7, 2023	December 31, 2023

There is more.

Testing Gas-Liquid Homogenization for High GVF Flow Applications in ESPs

Dr. Chidirim E. Ejim, Dr. Jinjiang Xiao, Dr. Hassan M. Badr, Dr. Abdelsalam M. Alsarkhi and Dr. Rached Ben-Mansour

Abstract / High gas volume fractions (GVFs) decrease the pressure boosting capacity of electric submersible pumps (ESPs). To prevent this, advanced gas handlers, helico-axial pumps, etc., may be installed upstream of the pump, but this equipment can be expensive. This study presents the results of testing different impeller combinations up to 90% intake GVF. The findings present a potential economical option for managing high GVF flows in ESP operation, beneficial to boosting and maximizing production from a field asset.

The pump used was a two-stage, radial-type centrifugal pump with a 3.78" impeller diameter operating at 3,400 revolutions per minute (rpm). Three impeller pairs were used: P0 (no hole in any impeller blades), P1 (holes only in the second stage impeller blades), and P2 (holes in the first and second stage impeller blades). Water flow rates were fixed from 75 barrels per day (bpd) to 550 bpd, and air flow rates varied to give intake GVFs between 10% and 92% for average fluid temperatures of approximately 25 °C. The corresponding differential pressures across the pump were measured and compared to one another.

Deep Learning Model for CO_2 Leakage Detection Using Pressure Measurements

Dr. Xupeng He, Marwah M. AlSinan, Dr. Yiteng Li, Dr. Hyung T. Kwak and Dr. Hussein Hoteit

Abstract / Geologic carbon dioxide (CO_2) sequestration (GCS) has been considered as an efficient engineering measure to decrease the global CO_2 emissions. The real-time monitoring of CO_2 leakage is an important part of big-scale GCS deployment. In this work, we introduce a deep learning-based algorithm using a hybrid neural network for detecting CO_2 leakage based on bottom-hole pressure (BHP) measurements.

The proposed workflow includes the generation of train validation samples, the coupling process of training and validating, and the model evaluation. This work solves the diffusivity equation for pressure within the Computational Modeling Group framework used to generate data sets under no leakage conditions. A Bayesian optimization process is performed to optimize the model hyperparameters. We test the performance of the hybrid neural network called the convolutional neural network (CNN) and bi-directional long short-term memory (CNN-BiLSTM) on the BHP data collected from CO_2 leakage simulations.

Use of Symbolic Regression for Developing Petrophysical Interpretation Models

Dr. Songhua Chen, Dr. Wei Shao, Dr. Huiwen Sheng and Dr. Hyung T. Kwak

Abstract / A new physics guided artificial intelligence (AI) machine learning method for petrophysical interpretation model development is described. The workflow consists of the following five constituents: (1) Statistical tools, such as correlation heat maps, are employed to select the best candidate input variables for the target petrophysical equations; (2) A genetic programming-based symbolic regression (SR) approach is used to fuse multiphysics measurements data for training the petrophysical prediction equations; (3) An optional ensemble modeling procedure is applied for maximally utilizing all available training data by integrating multiple instances of prediction equations objectively, which is especially useful for a small training data set; (4) A means of obtaining conditional branching in prediction equations is enabled in SR to handle certain formation heterogeneity; and (5) A model discrimination framework is introduced to finalize the model selection based on mathematical complexity, physics complexity, and model performance.

أرامكو السعودية
saudi aramco

Aramco
Journal
of Technology

Liked this issue? Sign up. It's free.

To begin receiving the *Aramco Journal of Technology* please complete this form, scan and send by email to ***william.bradshaw.1@aramco.com.***

Got questions?

Just give us a call at +966-013-876-0498 and we'll be happy to help!

Scan the QR code to go straight to your email and attach the form!

Subscription Form

Name

Title

Organization

Address

City

State/Province

Postal code

Country

Email address

Phone number

Number of copies